VITAL SIGNS MONITORING USING DOPPLER SIGNAL DECOMPOSITION

YUQING LI

VITAL SIGNS MONITORING USING DOPPLER SIGNAL DECOMPOSITION

DISSERTATION

to obtain the degree of Master of Science
in Electrical Engineering
at Delft University of Technology,
to be defended publicly on Friday August 21, 2020 at 09:00 AM

by

YUQING LI

born in Liaoning, China.

This thesis has been approved by the

supervisor:	Prof. DSc. Olexadner Yarovyi
daily supervisor:	Dr. Nikita Petrov

Thesis committee:

Prof. DSc. Olexadner Yarovyi,	MS3 TU Delft
Prof. dr. ir. Richard Heusdens,	CAS TU Delft / NLDA
Dr. Nikita Petrov,	MS3 TU Delft

Contents

1

INTRODUCTION

1.1. MOTIVATION

Cardiopulmonary signals, respiration and heartbeat, are crucial indicators of vital signs: they can be used to judge the state of the human body and detect abnormal cardiopulmonary activities, essential to particular medical emergencies. A growing interest in people's health monitoring is strengthened by the rapid development of medical electronic technologies, and ever-growing demand for monitoring cardiopulmonary signals during a variety of occasions, including clinical application, and daily activities: sleeping, driving and sports.

Radar-based vital signs monitoring has been an object of research since the 1970s, which detects human chest displacement using Doppler radar. Non-contact, accurate and real-time monitoring of human respiration and heartbeat signals can be achieved through the processing of radar echo.

1.2. OVERVIEW OF VITAL SIGNS MONITORING TECHNOLOGIES

Modern vital signs detection approaches, such as electrocardiography (ECG) for heart monitoring [1] and inductive or optoelectronic plethysmography for respiratory monitoring are designed for disease diagnosis with high reliability. However, the application of such devices during daily activities is infeasible by their bulkiness, high cost and complicated operation [2].

To overcome these shortcomings, miniaturized and portable devices of vital signs detection have recently attracted considerable interest. In the last decade, there has been a growing emergence towards portable or wearable devices, which can be used to detect various vital signs (heartbeat rate, body temperature, blood oxygen, etc.) of humans [3] [4]. Although most of the current vital signs detection devices are small-sized and non-invasive, they still bound a user by electrodes or cables. Also its application range is restricted: contact electrodes can interfere with the measurement of some physiological parameters, and thus affect the accuracy of parameter estimation.

1

Non-contact vital sign detection can overcome these shortcomings by measuring respiration, heartbeat and other parameters without contacting the human body. The sensor is not directly in touch with the body and detects physiological signals from a distance. It provides a convenient, non-invasive and remote detection way for vital signs monitoring, crucial for physiological signal detection in difficult occasions, such as patients with large-scale burn trauma, infectious and mental patients; long-term monitoring of infants and sleep disorders in adults; life detection during disaster rescue such as earthquake collapse [5].

Schematic comparison of existing mainstream contact/non-contact vital sign detection approaches is listed in Tab. 1.1 [2].

Approach	Contact or not	Measured vital sign	Main advantage	Main disadvantage
Strain measurement[3]	Contact	Respiration heartbeat	Unobtrusiveness	Motion artifacts
Impedance measurement[4]	Contact	Respiration heartbeat	Unobtrusiveness	Motion artifacts
Movement measurement[6]	Contact	Respiration heartbeat	Unobtrusiveness	Motion artifacts
Air component[7]	Contact	Respiration	Accuracy	Intrusiveness
Biopotential measurement[1] (i.e., ECG)	Contact	Respiration heartbeat	Accuracy	Motion artifacts
Light intensity measurement (i.e., PPG)[1]	Contact	Respiration heartbeat	Unobtrusiveness	Motion artifacts
Infrared[8]	Non-contact	Body temperature	Accuracy	Environment dependent
Camera (i.e., rPPG)[9][10]	Non-contact	Respiration heartbeat	Unobtrusiveness	Lighting condition dependent
Visible light[11]	Non-contact	Respiration heartbeat	Low-cost	Lighting condition dependent
Radar [12]	Non-contact	Respiration heartbeat	Environment independent	Sensitivity to interference
Microphone[13]	Non-contact	Respiration heartbeat	Low-cost	Sensitivity to noise
Sonar[14]	Non-contact	Respiration	Environment independent	Insensitivity to small motion

Table 1.1: Vital signs detection approaches

From the table, it can be seen that contact-based approaches measure parameter changes (strain, displacement or current, etc.) during cardiopulmonary activities to ob-

tain vital signs, while non-contact approaches use electromagnetic wave or sound wave to detect vital signs remotely. Camera and visible light-based vital signs monitoring technology puts high demands on the lighting condition, and microphone-based monitoring requires a quiet environment. Radar and sonar-based vital signal monitoring techniques are both independent of the environment, while the former has lower cost and complexity, leading to wider usage in vital signs monitoring.

1.3. RADAR-BASED VITAL SIGN MONITORING TECHNIQUES

The real-time detection of cardiopulmonary parameters extraction with radar needs to address the following challenges: limited time duration of the signal for the extraction of cardiopulmonary signals, accuracy of vital signs parameters estimation and signal processing algorithm complexity. In this section, we recall the methods for remote vital signs detection and parameter estimation (respiration and heartbeat frequencies).

Modern time-frequency analysis methods include short-time Fourier transform [15], Gabor transform [16], etc., which can be seen as evolved forms of Fourier transform. However, spectrum resolution of STFT may not be sufficient to track frequency changes of a rapidly varying non-stationary signal. Gabor transform is a STFT with a Gaussian window, but it is difficult to find the optimal fitting model.

More advanced time-frequency representation method, such as wavelet transform (WT) [17], can overcome the resolution limitation of STFT. WT is a time-scale analysis method which estimates the wavelet coefficients from the signal, and exploits the recombination algorithm to analyze their frequency content. Wavelet Transform (WT) and its modifications such as Wavelet Filter [18], Wavelet Packet Decomposition (WPD) [19], Discrete Wavelet Transform (DWT), Complex Wavelet Transform (CWT) [20], CWT with Morlet mother wavelet [21] have been recently applied to separate and estimate respiration and heartbeat signals. The traditional spectral analysis methods such as Fourier transform and wavelet have certain limitations for time-frequency analysis: the former can only obtain the overall distribution of the spectrum, which does not include the frequency changes over time; the latter suffers from the optimal choice of the wavelet base.

STFT and wavelet transform are both linear time-frequency representations. To describe the instantaneous power spectral density of a signal, quadratic time-frequency representation is applied. It describes the energy density distribution of the signal, the most popular methods are Winger-Vile distribution (WVD) [22] [23] and Cohen time-frequency distribution [23]. When the signal has multiple frequency components, quadratic time-frequency distribution suffers from the cross terms, which generate false harmonics and can result in the frequency estimation error, crucial for considered application [24]. A proper design of kernel function can suppress this effect [25].

Another brunch of research focuses on the application of the modern spectrum analysis methods to overcome the limitations of FT. Among these methods, RELAX is a parametric and cyclic optimization approach for the estimation of sinusoidal parameters proposed in [26]. It has demonstrated in [27] that RELAX can mitigate the effects of smearing and leakage in conventional Periodogram, succeeding in the estimation of vital signs parameters, but it has a shortage of computational complexity. Another approach reported is a multiple signal classification algorithm referred to as MUSIC. The eigenvalue decomposition of the covariance matrix composed of received signals is used to

obtain the spectrum by using the minimum eigenvector of the covariance matrix. The MUSIC algorithm is used to estimate the frequency of time-domain waveform after high-frequency filtering, and extract the required vital sign parameters [28]. The shortcomings of the MUSIC algorithm are its computation complexity in spectral peak search. Therefore, Barabell proposed a Root-MUSIC algorithm [29], which uses the polynomial root search method instead of spectral peak search to achieve computational efficiency.

Iterative adaptive approach (IAA) is a robust, high resolution, and low sidelobe frequency estimation method, which can be employed to obtain the IAA spectrum of the radar echo. Thus, frequencies of respiration and heartbeat can be reliably determined from the IAA spectral estimation [30]. In addition, Lomb-Scargle Periodogram was also applied for respiratory rate estimation. Experimental verification has proved that motion artifacts can be eliminated in Lomb-Scargle Periodogram, providing a reliable result when estimating the respiration frequency [31].

A few digital signal processing algorithms to extract chest wall displacement due to respiration with two microwave Doppler radars are presented in [32]: Mean of signals (MEAN), Least Squares (LS), Hough Transformation (HOUGH), Particle Filter (PF) and Direct Phase Estimation based on Vector Difference (DIFF). Experimental results show that the best phase estimation method for measuring respiration is the LS method with appropriate window size. However, accurate estimation of respiration frequency is difficult to achieve in LS method if the human chest is not facing the radar sensor. Application of Extended Kalman filter for vital signs monitoring was proposed in [33]. It used I and Q channel signal as input signal separately, and after the estimation, principal component combining (PCC) and digital elliptic filtering are applied to get the respiration and heartbeat rate. However, there is still a lack of dynamic modeling of vital signs and their extraction techniques [34].

Empirical mode decomposition (EMD) is an analysis method for nonlinear and non-stationary time series signals. EMD decomposes the input signal into a series of so-called intrinsic mode functions (IMF) [35]. Hilbert-Huang transform (HHT) is applied after EMD to obtain instantaneous frequencies of IMFs, which is called Hilbert-Huang time-frequency distribution. HHT overcomes shortcomings of Fourier and Wavelet transform and can provide the time-frequency spectrum of the signal with high resolution. Ensemble empirical mode decomposition (EEMD) is a modification of EMD proposed to settle the mode mixing problem, performed in non-contact vital signs sensing systems [20][36]. However, the reconstructed signal this method still contains the residual noise component. And EEMD requires complex recursion and takes longer calculation time compared to STFT. CEEMDAN was developed as a modification over EEMD, which has less number of sifting iterations [37]. However, the rigorous physical and mathematical significance of CEEMDAN needs to be explored and explained further.

Empirical signal decomposition methods are sensitive to noise, a more advanced technique called Variational Mode Decomposition (VMD) is further introduced to tackle the problem. It is an adaptive decomposition algorithm, the purpose of the variational mode decomposition algorithm is to obtain the optimal solution through iteration, so as to determine the central frequency and bandwidth of each IMF and extract the signal components. Different from the definition of the IMF in EMD algorithm, the IMF of VMD algorithm is an amplitude-frequency modulation signal [38]. Based on VMD, the

respiration signals of different humans can be decomposed into different sub-signals, and then the time-varying respiration signals can be accurately tracked [39].

An alternative numerical analysis method is third-order cyclic cumulant (TOCC) [40]. For a non-stationary statistical signal, if it undergoes periodicity after some non-linear change, it can be seen to have the property as cyclostationarity. The received Doppler radar signal exhibits cyclostationarity in non-contact vital signs sensing system, so TOCC can be performed. In literature, the TOCC detection method shows its insensitivity to Gaussian interference and non-cyclic signals, the respiration and heart frequencies can be accurately detected [41].

According to the description of signal processing methods in this chapter, the variety of popular signal processing approaches in vital signs monitoring are summarized in Tab. 1.2.

Approach	Main advantage	Main disadvantage
STFT	Simple and conventional	Unfit into the frequency changes of a rapidly varying non-stationary signal
GT	High resolution of spectrogram	Determination of best fitting model
WT	Multi-scale analysis	Choice of wavelet base
RELAX	Solve smearing and leakage problems of the conventional Periodogram	Computational complexity
MUSIC	Multi-signal detection	Computational complexity
IAA	High resolution, low sidelobe	Computational complexity
EKF	High computational efficiency	Lack of dynamic modelling of non-Gaussian noise
PF	Unlimited model noise, simple algorithm	Large amount of calculation
EMD	Suitable for nonlinear and non-stationary time series signals	Mode mixing
EEMD	Solve mode mixing problem	Reconstructed signal contains artificially added noise components
CEEMDAN	Solve mode mixing problem low computational cost	Lack rigorous physical and mathematical significance
VMD	Robust to noise	Computational complexity

Table 1.2: Popular signal processing approaches in vital signs monitoring

1.4. OUTLINE OF THE THESIS

The thesis is structured as follows. Chapter 2 introduces the physiology of cardiopulmonary activity and models of vital signs. Besides, the principles of three radar systems and their requirements for vital signs monitoring are explored. In Chapter 3, four signal decomposition methods for vital signs detection and parameter estimation are demon-

strated: EMD, EEMD,CEEMDAN and VMD. These methods are evaluated by Monte-Carlo simulation and their performances under different circumstances are assessed. Chapter 4 describes two online signal decomposition methods, providing a dynamic estimation of respiration and heartbeat signal parameters. The performances of the proposed techniques for vital signs monitoring are also assessed by Monte-Carlo simulation. Experimental verification is then presented in Chapter 5, proving the feasibility of the above methods in vital signs monitoring. Finally, the conclusion and recommended future work are summarized in Chapter 6.

2

Models and Radar Systems for Vital Signs Monitoring

Existing non-contact vital signs monitoring relies on electromagnetic waves emitted by radar to penetrate obstacles and reach the human body to detect vital sign parameters. The radar will measure the slight displacement of the surface of human prothorax due to the physiological activities such as heartbeat and respiration. Therefore, the collected radar echo signals after human body reflection will carry the physiological activity information, and the vital signs parameters extracted from the data with modern signal processing methods.

In this chapter, the physiology of cardiopulmonary activity is introduced. Then the models of vital signs are described including the noise and possible vibration of auto in the application for driver state monitoring. In addition, various radar systems were applied for human being monitoring. In the final part of this chapter, the principles of these technologies, in particular, continuous wave (CW), linearly frequency-modulated continuous-wave (LFMCW) and impulse-radio (IR) ultra wide-band (UWB) radars are explored.

2.1. Signal Models for Vital Signs Monitoring

2.1.1. Physiology of Cardiopulmonary Activity

In some studies, it has been observed that the movement of the lungs and respiratory muscles can deform the heart. However, there is still no convincing conclusion on the interaction between the respiration and heartbeat [42]. Hence, respiration and heartbeat are regarded as independent activities in this thesis. In this section, the physiology and data models of the two kinds of cardiopulmonary activity, respiration and heartbeat, will be presented and discussed.

Lungs ventilation refers to the gas exchange process between lungs and the external environment. The human structure responsible for lungs ventilation includes the respiratory tract, thoracic cage, and respiratory muscles. The respiratory tract is the passage

of gas getting into and getting out of the lungs. Lungs are located inside the rib cage, with a closed pleural cavity between them. The respiratory muscles are attached to the thoracic cage, changing the volume of the thoracic cage through contraction and relaxation activities, causing the expansion and contraction of the lungs to provide power for lungs ventilation [43].

Under a natural breathing state, the internal volume of the lungs changes due to its expansion and contraction leading to changes in the lungs' pressure. Lungs do not have the ability to contract and relax independently due to their physiological characteristics. The contraction and relaxation of lungs changes with the corresponding activity of the thoracic cage, and the change of the thoracic cage is regulated by the control of the respiratory muscles. The contraction of the respiratory muscles corresponds to the reduction of the thoracic cage. Conversely, the relaxation of the respiratory muscles enlarges the thoracic cage, and the entire process becomes respiratory motion. The change in lungs volume during a respiratory cycle is shown in Fig. 2.1. Changes in lungs volume reflect the contraction and expansion of the rib cage and also the displacement of the chest wall.

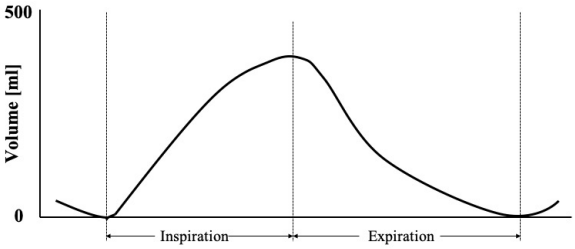

Figure 2.1: Changes in lungs volume during respiration process

The main function of the heart is to pump blood. The continuous and coordinated contraction and relaxation of the heart is a necessary condition for the realization of the blood pumping function. Each time the heart contracts and relaxes, it constitutes a cycle of mechanical activity, called the cardiac cycle. Since the ventricle plays a major role in the pumping activity of the heart, the cardiac cycle usually refers to the ventricular activity cycle. The cardiac cycle is the reciprocal of the heart rate, in one cardiac cycle duration, a mechanical vibration caused by factors such as myocardial contraction, open and closure of the valve, and the impact of blood flow can be transmitted to the chest wall through the surrounding tissue, giving rise to the corresponding movement of the chest wall [43]. The change of the ventricular volume in a cardiac cycle is depicted in Fig. 2.2.

The diastole process is filling with ventricular, by this time, the pressure of left ventricular drops, when it becomes lower than atrial pressure, the mitral valve will open (1). Then the systole begins when the ventricles contract and all valves in the heart close, which is called isovolumetric ventricular contraction (2). As the pressure in the ventricle increases, when it is larger than the aorta pressure, the aortic valve opens and ventricular begins to eject blood (3). Finally, the pressure in the ventricles decreases with the outflow of blood, and the valve closes and comes to relaxation when its pressure falls below the pressure of the aortic valve. This process (4) is called isovolemic ventricular diastolic

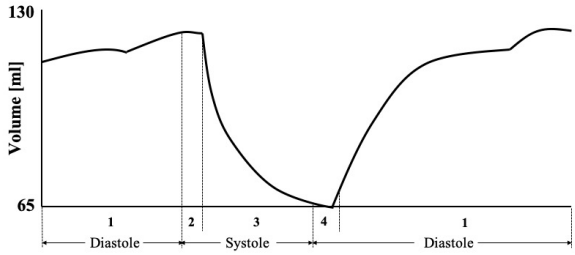

Figure 2.2: Changes in ventricular volume of cardiac cycle

period since all the valves in the heart are closed and the ventricles are in a diastolic state [43]. The actual chest displacements caused by respiration and heartbeat are depicted in Fig. 2.3 [44].

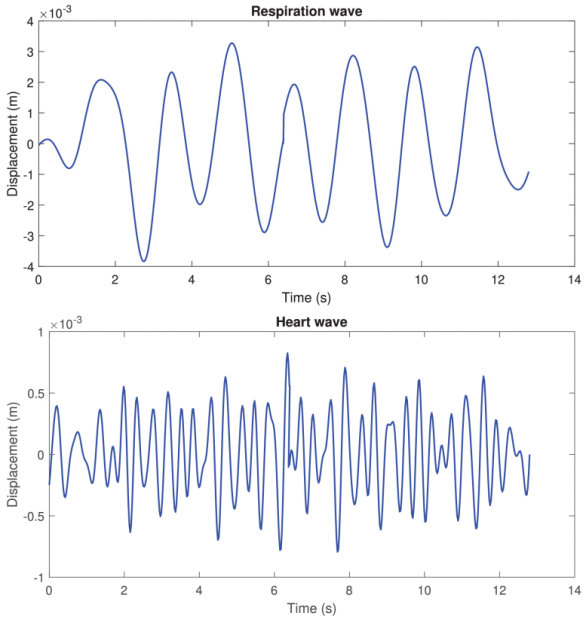

Figure 2.3: A sample of respiration (top) and heartbeat (bottom) waveforms vs time

2.1.2. CARDIOPULMONARY ACTIVITY MODEL

In general, healthy adults have a heartbeat rate of 50-100 beats per minute and take 6-24 breaths per minute. When the human body stays still and the mood remains stable, the respiration and heartbeat signals basically change periodically. In many experiments and research, a single tone movement is employed to simulate the periodic movement of the human chest induced by respiration and heartbeat, so respiration and heartbeat movements are approximated by sinusoidal movements with different amplitudes and

frequencies [45]. Then chest wall displacement $x(t)$ can be expressed by the summation of two sinusoidal signals:

$$x(t) = A_r \sin(2\pi f_r t) + A_h \sin(2\pi f_h t), \tag{2.1}$$

where A_r, A_h are the amplitudes of respiration and heartbeat, respectively, and f_r, f_h are the frequencies of respiration and heartbeat, respectively.

The typical values of respiration and heartbeat frequency and amplitude [43] are displayed in Tab. 2.1.

	Frequency[Hz]	Amplitude[mm]
Respiration	0.1-0.4	4-12
Heartbeat	0.83-1.67	0.3-0.6

Table 2.1: Typical frequencies and amplitudes of vital signs

However, the real movement of the two vital signs is not simply sinusoidal. Compared with the traditional sinusoidal vital signs model, the improved model is more in line with actual chest wall displacement, thus improving the authenticity of the simulation results. After analyzing a large amount of experimental data, it was found that the actual waveform of the respiration is more like a higher-order curve of a sinusoidal signal[46]. Prototype respiration pulse is:

$$p_r(t) = \sin^p(\pi f_r t), \quad p = 3 \tag{2.2}$$

leading to a discrete-time respiration signal component:

$$x_r(n) = A_r p_r\left(\frac{n}{f_s} - \left[\frac{n}{f_s} f_r\right]\frac{1}{f_r}\right), \tag{2.3}$$

where A_r and f_r are the amplitude and frequency of respiration signal, respectively. The improved and sinusoidal models of respiration are shown in Fig. 2.4, where $A_r = 8$mm, $f_r = 0.25$Hz, sampling frequency $f_s = 50$Hz.

The fluctuation caused by the heartbeat can only be transmitted to the chest wall through the bones and skin. So the heartbeat signal finally becomes the displacement of the chest, which is actually a "filter" procedure through the bones and skin [46]. The pulse signal $p_h(t)$ serves as a heartbeat signal model, in which the frequency of the heartbeat signal is f_h. The model of the pulse signal is set to the exponential $e^{-t/\tau}$, where τ is the heartbeat pulse time. The pulse signal is filtered by a second-order Butterworth filter, which is analogous to the actual attenuation of the heartbeat signal through the bones and skin. The improved heartbeat signal model is:

$$p_h(t) = e^{\frac{-t}{\tau}} + \left[\left(\frac{\sqrt{2}}{\omega_0 t} - 1\right)\sin\frac{\omega_0 t}{\sqrt{2}} - \cos\frac{\omega_0 t}{\sqrt{2}}\right] e^{\frac{-\omega_0 t}{\sqrt{2}}}, \tag{2.4}$$

where $\omega_0 = 2\pi f_0$ is the cutoff radian frequency, $\tau = 0.05$ and $f_0 = 1$ in this case.

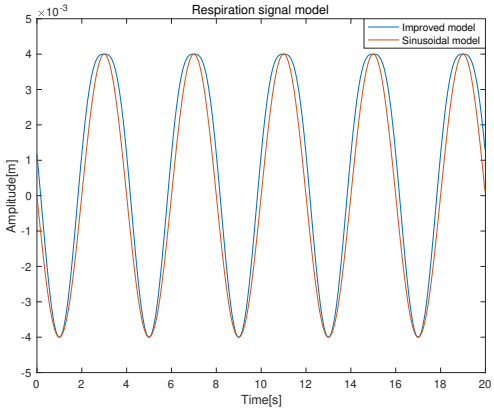

Figure 2.4: Improved respiration model vs sinusoidal respiration model

The discrete time model of the heartbeat signal is:

$$x_h(n) = A_h p_h\left(\frac{n}{f_s} - [\frac{n}{f_s} f_h]\frac{1}{f_h}\right), \tag{2.5}$$

where A_h is the peak-to-peak value of heartbeat signal, f_h is the frequency of heartbeat signal. Samples are sequentially taken until it reaches the heart-rate period, where the period ends and a new period will begin, $p_h(t)$ is the pulse response function that describes the period. The improved and sinusoidal models of heartbeat are shown in Fig. 2.5, where $A_h = 8$mm, $f_h = 1.3$Hz.

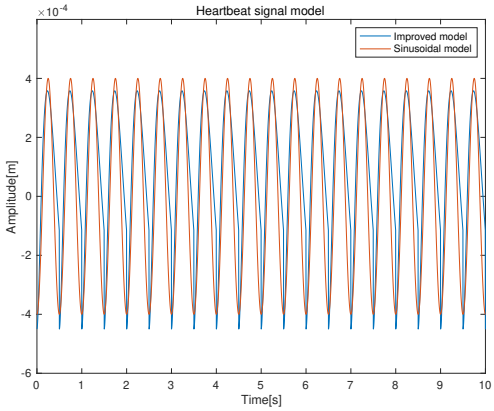

Figure 2.5: Improved heartbeat model vs sinusoidal heartbeat model

2.1.3. DYNAMIC CARDIOPULMONARY SIGNAL MODELS

In reality, the frequencies and amplitudes of respiration and heartbeat signals are not constant but slowly changes in time. The dynamic models of respiration and heartbeat signals are generated by first-order auto-regression models, which can be written as

$$f_{dynamic} = f + \Delta_{f,t} \tag{2.6}$$

$$\Delta_{f,t} = q\Delta_{f,t-1} + \sigma_f \sqrt{1-q^2}, \tag{2.7}$$

and

$$\alpha_{dynamic} = \alpha + \Delta_{\alpha,t} \tag{2.8}$$

$$\Delta_{\alpha,t} = q\Delta_{\alpha,t-1} + \sigma_\alpha \sqrt{1-q^2}, \tag{2.9}$$

where q is the model parameter, σ is the standard deviation of the driving noise, for respiration and heartbeat model, we usually assign different values to each of them. One example of dynamic cardiopulmonary signal models with $q_{f,r} = 0.99$, $q_{\alpha,r} = 0.98$ and $q_{f,h} = 1 - 10^{-3}$, $q_{\alpha,h} = 0.99$; $\sigma_{f,r} = 0.2$Hz, $\sigma_{\alpha,r} = 1$mm, $\sigma_{f,h} = 0.5$Hz and $\sigma_{\alpha,h} = 0.1$mm is in Fig. 2.6. From the figure, it can be seen that the frequencies and amplitudes of respiration and heartbeat vary with time, leading to the time-varying combined vital signs signal.

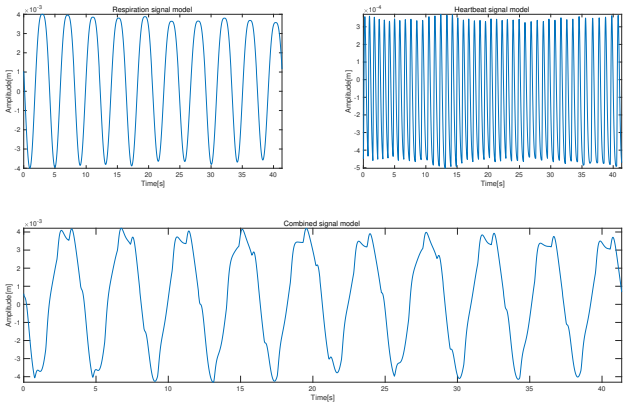

Figure 2.6: Dynamic cardiopulmonary models. Upper left: respiration signal model; upper right:heartbeat signal model; bottom: combined signal model

2.2. RADAR SYSTEMS FOR VITAL SIGNS MONITORING

2.2.1. SINGLE-TONE CONTINUOUS-WAVE RADAR

Continuous-wave radar has a long history of development, and it has advantages of low power consumption, compactness, and high Doppler sensitivity. Doppler effect consists in the change of received signal frequency when there is a relative radial movement

between the receiver and the target. Similarly, if the radar and the scatterer are not stationary with each other, the received echo impinges back to the radar at frequency f_r, different from the transmitted frequency f_t due to the Doppler effect. Assume a target in the radar's observation range is moving towards the radar, and the transmitted frequency of radar is f_t, the received frequency becomes:

$$f_r = \left(\frac{1+v/c}{1-v/c}\right) f_t, \tag{2.10}$$

where v is the radial velocity of target relative to the radar.

Since $v \ll c$, (2.10) can be simplified as:

$$f_r = \left(1+\frac{2v}{c}\right) f_t. \tag{2.11}$$

The instantaneous Doppler shift in frequency $f_d(t)$ can be expressed as a function of instantaneous velocity $v(t)$ of the moving target:

$$f_d(t) = \frac{2f}{c} v(t) = \frac{2v(t)}{\lambda}, \tag{2.12}$$

where λ is the wavelength of radar emitted signal. Denote the target displacement of the human chest as $x(t)$, then Doppler frequency shift of the reflected signal can be expressed using the integral relation of frequency and phase:

$$\theta(t) = \int_0^t 2\pi f_d(t)\,dt = \int_0^t 2\pi \frac{2f}{c} v(t)\,dt = \frac{2f}{c}(2\pi x(t)) = \frac{4\pi x(t)}{\lambda}. \tag{2.13}$$

Therefore, the displacement of the human chest can be measured via the variation of the phase, observed by the radar. Under an ideal circumstance, the time-varying phase information, proportional to the time-varying displacement of the human chest, can be obtained through phase demodulation and used to extract relevant information of respiration and heartbeat.

The sketch diagram of CW radar-based vital signs detection is depicted in Fig. 2.7. The transmitted signal $T(t)$ can be represented as:

$$T(t) = A_T \cos(2\pi f_c t + \phi(t)), \tag{2.14}$$

where A_T is the amplitude of transmitted signal, f_c is the carrier frequency, $\phi(t)$ is the fluctuation in signal phase.

Suppose the target has a time-varying displacement $x(t)$ on the distance d_0, then the distance between the transceiver and the target is

$$d(t) = d_0 + x(t). \tag{2.15}$$

The distance between the transceiver and the target will cause a propagation time delay, the delay of a round trip of the radar signal can be expressed as:

$$t_d = \frac{2d(t)}{c} = \frac{2(d_0 + x(t))}{c}. \tag{2.16}$$

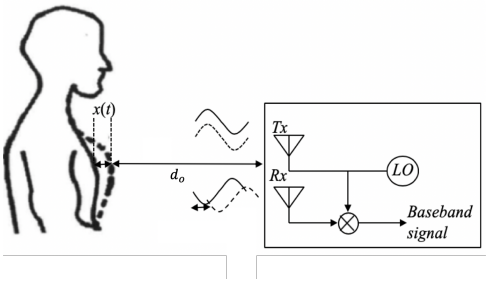

Figure 2.7: Sketch diagram of continuous wave radar based vital signs monitoring

The received signal $R(t)$ obtained by the receiver is a delayed copy of the transmitted signal, with amplitude A_R:

$$R(t) = A_R \cos\left[2\pi f(t-t_d) + \phi(t-t_d) + \theta_0\right], \tag{2.17}$$

where θ_0 is a constant phase shift affected by several factors, for example, the phase shift formed by the target's reflective surface (close to 180^o), and the time delay from transmitter to antenna. Combining (2.16) and (2.17), the received signal becomes:

$$R(t) = A_R \cos\left[2\pi f t - \frac{4\pi d_0}{\lambda} - \frac{4\pi x(t)}{\lambda} + \phi\left(t - \frac{2d_0}{c} - \frac{2x(t)}{c}\right) + \theta_0\right]. \tag{2.18}$$

Since the period of chest displacement is much longer than the time delay caused by the distance of radar and target, $T \gg d_0/c$, and the chest displacement is much smaller than the distance of radar and target, $x(t) \ll d_0$, the received signal can be approximately written as:

$$R(t) = A_R \cos\left[2\pi f t - \frac{4\pi d_0}{\lambda} - \frac{4\pi x(t)}{\lambda} + \phi\left(t - \frac{2d_0}{c}\right) + \theta_0\right]. \tag{2.19}$$

The received signal has a similar structure with the transmitted signal, with a time delay determined by the initial distance between the radar and target d_0 and the periodic movement of target chest $x(t)$. The phase of the received signal contains information of human chest motion.

Once the echo signal is received, it is demodulated by mixing the received echo signal with the same local oscillator, and a low pass filter is applied to extract the baseband signal:

$$B(t) = A_B \cos\left[\frac{4\pi x(t)}{\lambda} + \theta + \Delta\phi(t)\right], \tag{2.20}$$

where A_B is the amplitude of baseband signal, and $\Delta\phi(t)$ is the residual phase noise:

$$\Delta\phi(t) = \phi(t) - \phi\left(t - \frac{2d_0}{c}\right), \tag{2.21}$$

and θ is the constant phase shift proportional to d_0:

$$\theta = \frac{4\pi d_0}{\lambda} - \theta_0. \tag{2.22}$$

In order to avoid the problem of null detection point, restoring the target motion information with high accuracy, I/Q quadrature receiver and arctangent (AT) demodulation are often used [47]. The outputs of quadrature receiver contain in-phase (I) and quadrature (Q) baseband components are:

$$I(t) = A_I \cos\left[\frac{4\pi x(t)}{\lambda} + \theta + \Delta\phi(t)\right], \tag{2.23}$$

$$Q(t) = A_Q \sin\left[\frac{4\pi x(t)}{\lambda} + \theta + \Delta\phi(t)\right]. \tag{2.24}$$

Arctangent demodulation calculates:

$$\phi_{his}(t) = \arctan\left(\frac{Q(t)}{I(t)}\right). \tag{2.25}$$

It can make good use of information on I/Q quadrature channels and there are no harmonic and intermodulation effects between demodulated vital sign signals. Theoretically, AT demodulation can recover the complete chest wall displacement, the phase information of the baseband signal is:

$$\phi_{his}(t) = \frac{4\pi x(t)}{\lambda} + \theta + \Delta\phi(t). \tag{2.26}$$

And the range history of vital signs can be estimated from:

$$R_{his}(t) = \frac{c\phi_{his}(t)}{4\pi f_c}. \tag{2.27}$$

By doing this, information of human chest displacement is recovered.

2.2.2. FREQUENCY-MODULATED CONTINUOUS WAVE RADAR

A simple continuous-wave radar can only determine the velocity of a target, but not the distance between radar and target. Therefore, frequency-modulated continuous-wave (FMCW) radar is contrived to resolve the blemish. Linear frequency modulation (LFM) is the most commonly used in radar including vital signs monitoring, its principle will be described in this section.

The principle of range and relative velocity detection in LFMCW radar is exemplified in Fig. 2.8, showing the transmitted and received echo signals for detecting a target at a range of R, approaching with relative radial velocity v_r. The frequency of transmitted signal varies within the range $[f_0, f_0 + B]$ in period T_m, where f_0 is the minimum frequency and B is the bandwidth. A signal is emitted with frequency f_1 at time t_1, and it is received with frequency f_2 at time t_2, after a round-trip delay $\tau = 2R/c$ along with a Doppler frequency shift f_d. Then a procedure called de-ramping is applied where a mixer produces a baseband signal at the instantaneous difference frequency between the transmitter and the received signals, referred to as the beat signal $f_b = |f_{Tx} - f_{Rx}|$.

The sinusoidal transmitted signal from a LFMCW as in Fig. 2.8 can be expressed as:

$$T(t) = A_{Tx} \cos(\phi_{Tx}(t)), \tag{2.28}$$

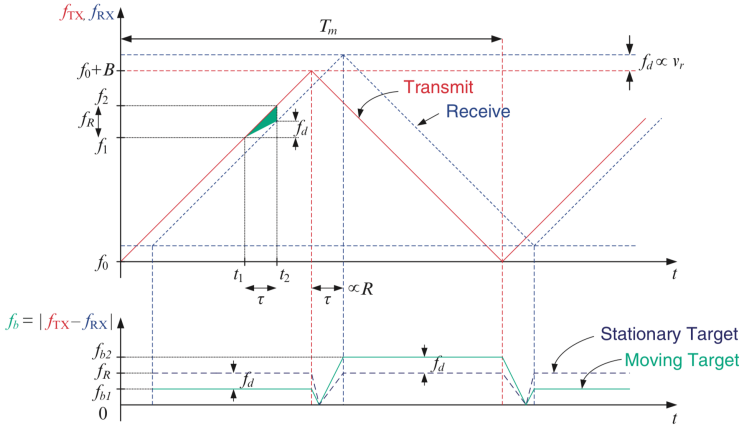

Figure 2.8: Principle of range and velocity measurement of LFMCW radar

where A_{Tx} is the amplitude of emitted signal and ϕ_{Tx} is instantaneous phase related to the instantaneous transmitter frequency f_{Tx}, which is shown as follows:

$$\phi_{Tx} = 2\pi \int_0^t f_{Tx}(t)dt. \tag{2.29}$$

For a chirp in the time interval $[0, T_m/2]$, the variation of transmitted signal frequency can be expressed as:

$$f_{Tx}(t) = f_0 + \frac{B}{T_m/2}t = f_0 + \frac{2B}{T_m}t. \tag{2.30}$$

Substituting (2.29) into (2.30), the instantaneous transmitter phase is obtained by:

$$\begin{aligned}\phi_{Tx} &= 2\pi\left(f_0 t + \frac{1}{2}\cdot\frac{2B}{T_m}t^2\right)\Big|_0^t \\ &= 2\pi\left(f_0 t + \frac{B}{T_m}t^2\right).\end{aligned} \tag{2.31}$$

For a target at range R, approaching radar with velocity v_r, the received signal from the moving target with a round-trip time delay is:

$$R(t) = A_{Rx}\cos(\phi_{Rx}(t)) = A_{Rx}\cos(\phi_{Tx}(t-\tau)), \tag{2.32}$$

where the delay $\tau = 2(R - v_r t)/c$.

As mentioned previously, a mixer produces a signal at the instantaneous difference frequency, referred to as beat signal, which is:

$$s_B(t) = A_B\cos(\phi_B(t)) = A_B\cos(\phi_{Tx}(t) - \phi_{Rx}(t)). \tag{2.33}$$

Then, combining the last two equation, the phase of beat signal is gained as:

$$\begin{aligned}\phi_B(t) &= \phi_{Tx}(t) - \phi_{Rx}(t) \\ &= 2\pi\left(f_0\tau + \frac{2B}{T_m}t\cdot\tau - \frac{B}{T_m}\tau^2\right).\end{aligned} \tag{2.34}$$

Since in most cases, $\tau / T_m \ll 1$ holds, the last term in (2.34) can be neglected. τ is a function of range R and velocity v_r, substitute τ, (2.34) can be expressed as:

$$\phi_B(t) = 2\pi \left[\frac{2R}{c} f_0 + \left(\frac{4B}{T_m} \cdot \frac{R}{c} - \frac{2v_r}{c} f_0 \right) t + \frac{4B}{T_m} \cdot \frac{v_r}{c} t^2 \right]. \tag{2.35}$$

The last term in (2.35) is known as range-Doppler coupling and it is negligible when $v_r << c$. Thus, frequency of beat signal can be obtained by differentiating simplified $\phi_B(t)$:

$$f_B = \frac{1}{2\pi} \cdot \frac{\partial \phi_B(t)}{\partial t} = \frac{4B}{T_m} \cdot \frac{R}{c} - \frac{2v_r}{c} f_0. \tag{2.36}$$

Since the beat signal is a rectangular-shaped frequency changing signal with period $T_m/2$, and Doppler frequency is estimated from a sequence of n chirps, the frequency resolution Δf is the reciprocal of the period:

$$\Delta f = \frac{2}{nT_m}. \tag{2.37}$$

Substituting (2.37) into $f_d = 2v_r f_0 / c$, the velocity resolution of target is given as:

$$\Delta v_r = \frac{c}{2f_0} \cdot \Delta f = \frac{c}{nf_0 T_m}. \tag{2.38}$$

Thus, higher velocity resolution can be achieved by increasing the transmitted frequency or the signal duration.

The range resolution of a FMCW radar is:

$$\Delta R = \frac{c}{2B}, \tag{2.39}$$

which is only related to the bandwidth.

The data collected by FMCW radar is organized as follows. The beat signals sampled in each sweep are stacked in rows of the data matrix in fast-time and slow-time dimensions. Collected data is in matrix $\mathbf{R}[n,k]$ ($n = 1,2,\ldots,N$; $k = 1,2,\ldots,K$), N being the number of samples per ramp (fast time samples) and K is the number of transmitted ramps. Apply fast Fourier transform (FFT) to each row of $\mathbf{R}[n,k]$, resulting in a range-profile matrix $\mathbf{RP}[n,k]$. Then select the range cell r in which the target is found, the desired signal is captured as a one-dimensional data set:

$$\mathbf{s}[n] = \mathbf{RP}[n,r]. \tag{2.40}$$

Extract the phase of signal $\mathbf{s}[n]$, we get the phase history ϕ_i. After obtaining the phase information ϕ_i of the desired signal, the 2π discontinuity of the extracted phase appears when an extreme value, $\pi / -\pi$, is reached; the phase then jumps to the other end of the interval, $-\pi / \pi$, which suffers from the deficiency known as phase wrapping. To tackle this problem, the unwrapping process [48] is necessary to avoid the jump of the extracted phase, the process steps are:

1. Calculate the difference between the current sample in wrapped phase signal $\phi_w(n)$ and its previous adjacent phase sample $\phi_w(n-1)$:

$$\Delta\phi = \phi_w(n) - \phi_w(n-1), \qquad n = 2,\ldots,N \tag{2.41}$$

2. If $\Delta\phi > +\pi$, subtract 2π from current phase sample and also from all the samples to the right of it.

3. If $\Delta\phi < -\pi$, add 2π to the current sample and also to all the samples to the right of it.

The process can be mathematically expressed as:

$$\phi_u(t) = \mathscr{U}[\phi_w(t)] = \phi_w(t) + 2\pi k, \qquad k \in \{-1, 1\} \tag{2.42}$$

where $\mathscr{U}[\cdot]$ indicates the phase unwrapping operation, then phase history $\phi_{his}(t)$ can be obtained as:

$$\phi_{his}(t) = \mathscr{U}[\phi_i(t)]. \tag{2.43}$$

Now we get the information of phase history, recovery equation of range history in FMCW radar system is the same as in CW radar system written in (2.27).

2.2.3. IMPULSE-RADIO ULTRA WIDE BAND RADAR

Compared with CW radar, UWB radar system has the capability of localization and can be used in multi-target vital signs monitoring. An IR-UWB Doppler radar detects the changes in the propagation time of transmitted impulses and reflected ones, monitoring human vital signs by analyzing the echos from the human chest back to the radar.

UWB radars have a very large relative bandwidth $\eta > 0.25$, and relative bandwidth is calculated as:

$$\eta = \frac{\Delta f}{f_c}, \tag{2.44}$$

with Δf and f_c indicting absolute bandwidth and carrier frequency of radar, respectively, and they are expressed as:

$$\Delta f = f_h - f_l, \tag{2.45}$$

$$f_c = \frac{f_h + f_l}{2}, \tag{2.46}$$

where f_h and f_l respectively denote the highest and lowest frequency in the band.

From basic pulse radar principle, the range resolution of UWB radar depends on the pulse repetition interval PRI, for a rectangular pulse of duration τ, -3dB bandwidth B can be approximated as $B = 1/\tau$, so the range resolution of pulsed UWB radar is defined similarly to as FMCW radar in (2.39).

The velocity resolution in UWB radar is given as:

$$\Delta v_r = \frac{c}{2nf_c \cdot PRI}, \tag{2.47}$$

where PRI denotes the pulse repetition interval of radar, n is the number of pulses in the observation time.

The impulse response of vital signs for an IR-UWB radar is:

$$h(\tau, t) = A \cdot \delta(\tau - \tau_d(t)), \tag{2.48}$$

where A denotes amplitude of the pulse reflected on surface of human chest, and τ_d is the time delay associated with the displacement of chest induced by vital signs:

$$\tau_d(t) = \frac{2d(t)}{c}, \tag{2.49}$$

and the expression of $d(t)$ is the same as the one in (2.15), c is the velocity of light.

Assume that $s(\tau)$ represents the transmitted pulse, the signal received at radar is then written as:

$$\begin{aligned} r(\tau, t) &= s(\tau) * h(\tau, t) \\ &= A \cdot s(\tau - \tau_d(t)). \end{aligned} \tag{2.50}$$

The received signals are measured in slow-time as discrete moments $t = kT_s, (k = 1, 2, \ldots, K)$, T_s is the sampling period in slow-time and K is the number of discrete time sequences in slow-time domain. The received signals are sampled and stored in a two-dimensional matrix with fast-time domain sampling period T_f:

$$\mathbf{R}[n, k] = r(\tau = nT_f, t = kT_s). \tag{2.51}$$

UWB radar can extract vital signs through Doppler information, the desired range history is directly obtained by selecting range cell r where the target is located:

$$R_{his}[k] = \mathbf{R}[r, k]. \tag{2.52}$$

2.2.4. VITAL SIGNS MONITORING REQUIREMENTS OF RADAR

Single-tone CW radar is the most common type in radar-based vital signs monitoring system due to its simplicity and low power consumption. But it cannot detect the vital signs of multi-subject at the same time since it cannot provide range information. FMCW and UWB radar are capable of measuring both range and Doppler frequency, therefore they can fulfill the functionality of multi-target detection. However, FMCW radar system suffer from high phase noise level and power consumption [49]. UWB radar system has been proven to have great penetration ability, giving dominant position for applications of search and rescue. But IR-UWB radar is limited by its power density restriction, leading to short distance applications. Performance of different radar systems for vital signs monitoring is summarized in Tab. 2.2 [49].

System	Multi-subject detection	Range estimation	Power consumption
CW	No	No	Medium
FMCW	Yes	Yes	High
IR-UWB	Yes	Yes	Low

Table 2.2: Comparison of Radar-Based Vital Signs Monitoring Systems

The observation time of radar should be set to have the capability of detecting the maximum velocity of the minimum human chest displacement. The maximum veloci-

ties of minimum respiration and heartbeat amplitudes in the sinusoidal model in Section 2.1.2 (2.1) can be calculated as:

$$v_{r,sin} = max\left\{\frac{\partial x_{r1}(t)}{\partial t}\right\} = 1.26 \text{ [mm/s]}, \tag{2.53}$$

$$v_{h,sin} = max\left\{\frac{\partial x_{h1}(t)}{\partial t}\right\} = 1.56 \text{ [mm/s]}. \tag{2.54}$$

And the maximum velocities of minimum respiration and heartbeat amplitudes in improved model described in Section 2.1.2 (2.3) and (2.5) can be calculated as:

$$v_{r,imp} = max\left\{\frac{\partial x_{r2}(t)}{\partial t}\right\} = 1.45 \text{ [mm/s]}, \tag{2.55}$$

$$v_{h,imp} = max\left\{\frac{\partial x_{h2}(t)}{\partial t}\right\} = 5.81 \text{ [mm/s]}. \tag{2.56}$$

The global minimum velocity of sinusoidal cardiopulmonary model is $v_{min,sin} = 1.26$mm/s, the global minimum of improved cardiopulmonary model is $v_{min,imp} = 1.45$mm/s.

For the sake of measuring this maximum velocity of the minimum chest displacement with central frequency f_c, it meet the requirement as follows:

$$\frac{c}{2f_c \cdot CPI} \leqslant 0.1 \cdot v_{min}, \tag{2.57}$$

so the coherent processing interval (CPI) of FMCW and UWB radars should be:

$$CPI \geqslant \frac{5c}{f_c v_{min}}. \tag{2.58}$$

According to the Nyquist sampling theorem, radar echo should be sampled over twice as fast as the highest frequency component. The maximum velocity of the sinusoidal and improved cardiopulmonary model is $v_{max} = 26.34$mm/s. So the sampling frequency in vital signs monitoring system should meet the requirement of:

$$f_s > 2f_{max} = 2\frac{2v_{max}f_c}{c}. \tag{2.59}$$

As discussed in Section 2.2.3, the range resolution of IR-UWB radar is defined as:

$$\Delta R = \frac{c}{2B},$$

where c is the velocity of light and B is the bandwidth of radar. Typical range resolution of UWB radar in vital signs monitoring is about 3mm.

The chest displacement we want to detect is in millimeter-scale and if vital signs are extracted from range displacement in UWB radar system, the requirement must be satisfied as:

$$\Delta R < A_{h,min}. \tag{2.60}$$

The range resolution of UWB radar is only related to bandwidth, so the choice of bandwidth is limited as:

$$B > \frac{c}{2A_{h,min}}. \tag{2.61}$$

Higher resolution implies larger bandwidth, a FMCW radar does not have very wide bandwidth, which limits its range resolution. In FMCW system, vital signs are extracted by obtaining Doppler information. Therefore, the range resolution of the FMCW radar is constrained by the required separation of multiple people in the scene.

One parameter related but not identical to range resolution is the accuracy of range measurement, depending essentially on bandwidth and noise, and it is described by:

$$\delta R = \frac{c}{2B\sqrt{2SNR}} = \frac{\Delta R}{\sqrt{2SNR}}. \tag{2.62}$$

So bandwidth and signal-to-noise level are two significant parameters for the accuracy in range determination. Range resolution contributes to accuracy in range domain but is not the only factor.

In like manner of range resolution, radar velocity resolution can be written as:

$$\Delta v = \frac{c}{2nf_cT},$$

where c is speed of light, f_c is radar carrier frequency, T denotes duration of a chirp (for CW radar) or a pulse (for IR-UWB radar). The smallest resolvable velocity for FMCW and UWB radars should not be larger than the maximum velocity of heartbeat signal with minimum amplitudes, which is expressed as:

$$\Delta v < v_{h,min}. \tag{2.63}$$

So the velocity resolution of a radar used for vital signs monitoring should be about 1mm/s.

2.3. RADAR RECEIVED DATA MODEL

In the previous section, the extraction of range history in different radar systems was introduced. However, in the actual working environment of radar, noise and automobile vibration are unavoidable and they will interfere with the target signal. Vibration can be seen as extra range displacement and thus additive to range history induced by chest movement. The phase noise can be assumed Gaussian in moderate to high SNR case, hence the noise can also be added to the range history. White and colored Gaussian noise are added to received data of vital signs s in order to simulate the environment noise n and car vibration v, so the radar received data will become:

$$y = R_{his} + n + v, \tag{2.64}$$

where R_{his} is the range history induced by vital signs, n is white Gaussian noise, and the car vibration v is modelled by a second-order autoregressive model:

$$v_t = \alpha_1 v_{t-1} + \alpha_2 v_{t-2} + \varepsilon_t, \tag{2.65}$$

where α_1, α_2 are parameters of the model, $\varepsilon_t$is white noise. The process is stable when the roots are within the unit circle, which means the coefficients α_1, α_2 satisfy:

$$-1 \le \alpha_2 \le 1 - |\alpha_1|. \tag{2.66}$$

The power spectral density of AR(2) model can be expressed as:

$$S(f) = \frac{1}{1+\alpha_1^2+\alpha_2^2-2\alpha_1(1-\alpha_2)cos(2\pi f)-2\alpha_2 cos(4\pi f)}. \tag{2.67}$$

The power spectrum of one example of auto vibration simulated by AR(2) model is depicted in Fig. 2.9, in which $\alpha_1 = 1.97, \alpha_2 = -0.99$, and the spectral peak appears at 1.2Hz.

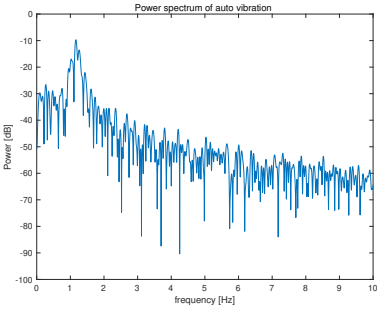

Figure 2.9: Power spectrum of auto vibration

Generally speaking, the sources of vibration in a vehicle is very complicated, including mechanical vibration (e.g. engine, driveline, tire contact patch, and the road surface, brakes) and electrical vibration (e.g. vibration coming from electrical actuators, alternator or traction motor in electrical cars) [50]. Most of these vibrations are not uniformly distributed over frequency, instead there always are spectral peaks show up in the frequency domain [51]. Since the frequencies of vital signs are much lower compared to most of the strong automotive vibration (seen in 2.10, the spectral peak appears around 300Hz), only low frequency vibration whose spectral peak around 1Hz will be taken into consideration in this thesis.

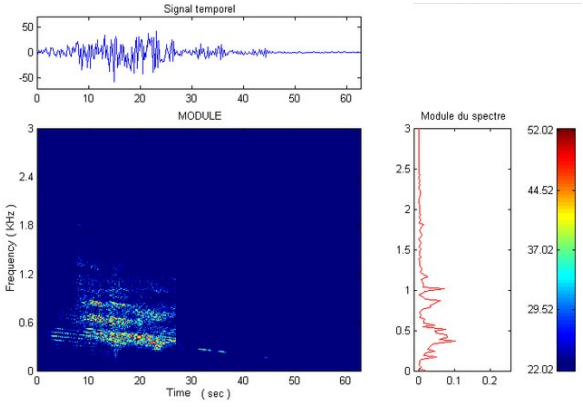

Figure 2.10: Spectrogram of the braking vibrations [51]

2.4. CONCLUSION

The main content in this chapter consists of a description of the cardiopulmonary activity, followed by its mathematical model and the extension of the model to dynamic condition. Most studies simplify the respiration and heartbeat as sinusoidal models. The improved cardiopulmonary signal models were investigated in this chapter to provide better fitness of vital actual signs waveform. Furthermore, a first-order auto-regression model was proposed to simulate the fluctuation of both respiration and heartbeat signals in reality.

Afterwards, three types of radar systems used in vital signs monitoring were described. These are continuous wave (CW) radar, frequency modulated continuous wave radar (FMCW) and ultra- wideband (UWB) radar. The major advantages of single-tone CW radar are simple structure, low power consumption. However, it lacks capability of range measurement, and thus target detection and localization. Reasonable approaches to resolve this issue could be FMCW radar and UWB radar. The main disadvantages of FMCW radar are high power consumption, while impulse-radio UWB radar requires larger volume than CW although usually residing with high spatial resolution [30].

Subsequently, radar received data model was constructed, embracing range history, the possible presence of noise and auto vibration. We modeled environment noise by white Gaussian noise and auto vibration as a colored Gaussian noise simulated by a second-order auto-regressive model, which spectral peak is near 1Hz.

3

SIGNAL DECOMPOSITION AND ANALYSIS METHODS

Radar echo signal contains information on respiration and heartbeat signals, as well as background noise, clutter and interference. Prior to analyzing the radar data directly, a few signal decomposition methods are considered to extract vital signs from radar data. The most well-known tool is the empirical mode decomposition (EMD). To improve the stability of EMD against noise, two modifications of EMD are investigated, namely, ensemble empirical mode decomposition (EEMD) and complete ensemble empirical mode decomposition with adaptive noise (CEEMDAN). However, EMD and its modifications algorithms are sensitive to noise. So variational mode decomposition (VMD) is investigated to address the issue of EMD algorithms. The analysis of the extracted signals is demonstrated with the Hilbert transform, which shows the time-frequency-energy distribution of each mode.

The main themes covered in this chapter are the description of empirical, variational mode decomposition algorithms, and numerical analysis of these methods.

3.1. EMPIRICAL MODE DECOMPOSITION

Empirical mode decomposition is an adaptive and highly efficient method that decomposes a compound signal into a finite number of intrinsic mode functions (IMF), to which well-behaved Hilbert transform can be applied to construct time-frequency spectrum of each component [52]. In order to make the instantaneous frequencies of a signal meaningful, its envelopes should be symmetric with respect to zero and it should have the same number of zero crossings and extreme points [53]. On this basis, the two physical constraints of IMF were proposed in [52]:

1. Each intrinsic mode function should either have the same number of extrema and zero crossings, or differ by one at most;

2. At any point, the mean value of the upper envelope of maxima (see in Fig. 3.1(a))

and the lower envelope of minima (see in Fig. 3.1(a)) is zero, that is, local symmetry on zero axis.

Apparently, the first constraint is to make the instantaneous frequency of any point in IMF meaningful [54]. The second constrain is the idea of replacing the global requirement with a local one, preventing instantaneous frequencies from unwanted fluctuations incurred by asymmetric waveform [52]. In each cycle of the decomposed signal represented by IMF, it contains only one oscillation mode, which can be either frequency and amplitude modulated, or even non-stationary.

The first constrain is crucial to make the instantaneous frequency meaningful, while if the second constrain is carried to the extreme, the amplitude fluctuations of IMF will be wiped out. There is a systematic way that can intuitively decompose a signal to obtain IMFs in the time domain, denominated as a sifting process of EMD. So a stopping criterion for the sifting process is proposed in order to guarantee both amplitude and frequency modulations of IMFs are physically meaningful. The criterion is usually realized by restriction of the standard deviation of two consecutive sifting processes.

The essence of EMD is to empirically determine the intrinsic oscillation modes of the original signal based on their characteristic time scales, and accordingly decompose the signal into several IMFs [52]. EMD is thus performed with the following steps [52]:

1. Find all local maximum value of input signal $s(t)$, connect all local maxima by a cubic spline to get the upper envelope $s_{max}^{(1,1)}(t)$ (see Fig. 3.1(a)). Repeat the procedure to find local minima and produce the lower envelope $s_{min}^{(1,1)}(t)$ (see Fig. 3.1(b)).

2. Calculate the mean of upper and lower envelopes, get the mean envelope m_1 depicted in Fig. 3.1(c):
$$m_1 = \frac{s_{max}^{(1,1)}(t) + s_{min}^{(1,1)}(t)}{2}. \tag{3.1}$$

3. The difference between the original signal and mean envelope is the first component $m_{1,1}$, The residue $h_{1,1}$ shown in Fig. 3.1(d):
$$h_{1,1} = s(t) - m_{1,1}. \tag{3.2}$$

4. Replace the original signal $s(t)$ with $h_{1,1}$ and repeat Step 1-3, until standard deviation from the two consecutive sifting is less than predefined value ϵ:
$$SD = \frac{\sum(h_{1,k-1} - h_{1,k})^2}{\sum h_{1,k-1}^2} < \epsilon, \tag{3.3}$$
with ϵ is typically set between 0.2 and 0.3. The first IMF component is decomposed and designated as:
$$c_1 = h_{1,k} = m_{1,k} - h_{1,k-1}. \tag{3.4}$$

5. Repeat the steps above until the final residual has no more oscillation and cannot be decomposed, meaning the number of extrema in the last residual should not be greater than one. The residual $r_n(t)$ indicates the mean trend of the signal. After

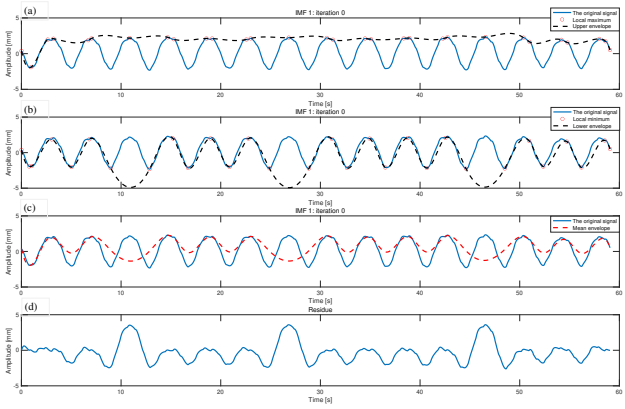

Figure 3.1: EMD sifting process: (a) upper envelope; (b) lower envelope; (c) mean envelope; (d) residue.

EMD, the input signal $s(t)$ is expressed as the summation of a finite number of IMFs $c_i(t), i = 1,\ldots,n$, and the residual $r_n(t)$:

$$s(t) = \sum_{i=1}^{n} c_i(t) + r_n(t). \tag{3.5}$$

EMD is an adaptive signal decomposition algorithm thus it can decompose the respiration and heartbeat signal from human chest displacement information carried by radar echo data [55]. Fig. 3.2 displays a simple empirical mode decomposition result from simulated mixed signals of respiration, heartbeat and environment noise. It can be seen from the result that the waveforms in different time scales are extracted and highlighted. The first IMF contains the highest frequency component of the original signal, after step-wise decomposition, the frequency of IMF decreases in turn while the last IMF contains the lowest one. The last component is the original signal trend instead of a oscillation mode. Also, it should be noticed that mode mixing happened at IMF2-3 and IMF4-5. Part of the intrinsic mode in IMF3 leaks into IMF2 and IMF5 contains some component of IMF4. So, the determination of respiration and heartbeat signals should be achieved by analyzing the frequency information of different IMFs. The exposition of frequency analysis method, called Hilbert-Huang transform, will be in Section 3.2.

3.2. HILBERT-HUANG TRANSFORM

Hilbert Huang transform (HHT) is a signal analysis method proposed by Norden E. Huang etc in 1998 [52]. It is a time-frequency analysis method that can effectively analyze linear and nonlinear, stationary and non-stationary signals. The essences of HHT are empirical mode decomposition (EMD) and Hilbert transform (HT), the former is a signal decomposition method, the latter is a spectral analysis method.

It can be found from the development of signal analysis methods that various methods are posed to satisfy the interest in different features of different signal types. For a

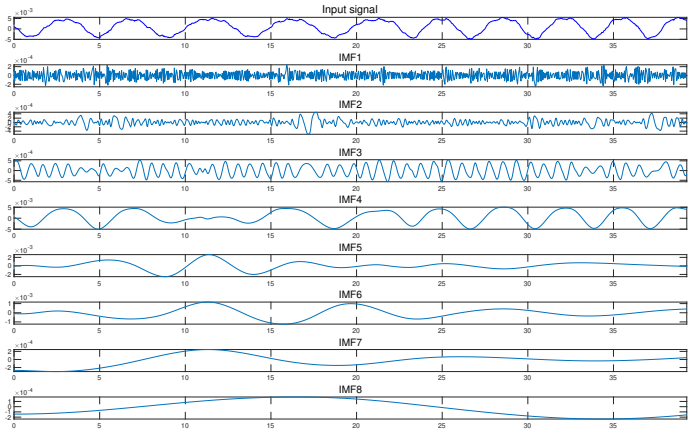

Figure 3.2: The resulting EMD components from noisy vital signs

stationary linear or periodic signal, the spectrum of the signal can be obtained by means of Fourier transform. For a non-stationary or nonlinear signal, the local spectral features of the signal are of interest. Different time-frequency analysis methods are used to obtain the time-frequency representation of the signal, such as short-time Fourier transform (STFT) [16], Wavelet transform (WT) [56] and Wigner-Ville distribution (WVD) [57].

However, the time-frequency analysis methods mentioned above are based on the Fourier transform, lacking adaptivity to the signal. In addition, these time-frequency analysis methods cannot accurately describe rapid changes of frequency over time due to the limitation of Heisenberg's uncertainty principle. So ideally, in order to accurately describe frequency changes over time, an adaptive, intuitive, instantaneous frequency analysis method is needed, which is the Hilbert Huang transform. In this framework, EMD is used to adaptively decompose the signal into a finite number of intrinsic mode functions (IMF) and a residual signal representing the trend of the signal. Then Hilbert transform is used to conduct time-frequency analysis to the acquired IMFs.

In empirical mode decomposition, input signal $s(t)$ is decomposed into the summation of n intrinsic mode functions $c_i(t)$ and a residual signal $r_n(t)$. Hilbert transform is applied to each IMF:

$$Y_i(t) = \frac{1}{\pi} PV \int_{-\infty}^{\infty} \frac{C_i(\tau)}{t-\tau} d\tau, \tag{3.6}$$

where PV is the Cauchy principal value. The resulting analytical signal is:

$$Z_i(t) = C_i(t) + jY_i(t). \tag{3.7}$$

In the form of polar coordinates:

$$Z_i(t) = a_i(t)e^{j\theta_i(t)}, \tag{3.8}$$

and

$$a_i(t) = \left[C_i^2(t) + Y_i^2(t)\right]^{\frac{1}{2}}, \qquad \theta_i(t) = \arctan\left[\frac{Y_i(t)}{C_i(t)}\right]. \tag{3.9}$$

The polar form of the analytical signal reflects the physical meaning of the Hilbert transform, which is the best local approximation of the signal through a sinusoidal frequency and amplitude modulation. According to the meaning of instantaneous frequency, the instantaneous frequency of each IMF can be obtained:

$$\omega_i(t) = \frac{d}{dt}\theta_i(t). \tag{3.10}$$

With time t and instantaneous frequency $\omega_i(t)$ as the independent variables, the signal amplitude can be expressed as a function of t and $\omega_i(t)$. This amplitude-time-frequency distribution is called Hilbert spectrum.

Examples of Hilbert spectrum are displayed in Fig. 3.3, demonstrating the time-frequency-energy distribution of IMF1-8 as the result of EMD in Fig. 3.2. The frequency distribution of IMF3 is concentrated at a narrow region around 1.5Hz and IMF4 is around 0.25Hz. Based on this representation, it is reasonable to tell IMF3 mainly contains heartbeat components while the respiratory signal component is mostly represented in IMF4. It can be seen from the Hilbert spectrum that the instantaneous frequency changes rapidly at certain moments, indicating occurrences of mode mixing. The color bar in the Hilbert spectrum shows the instantaneous energy intensity of IMFs, and yellow-colored curve implies the strongest energy, indicating the mode that represents original respiration signal.

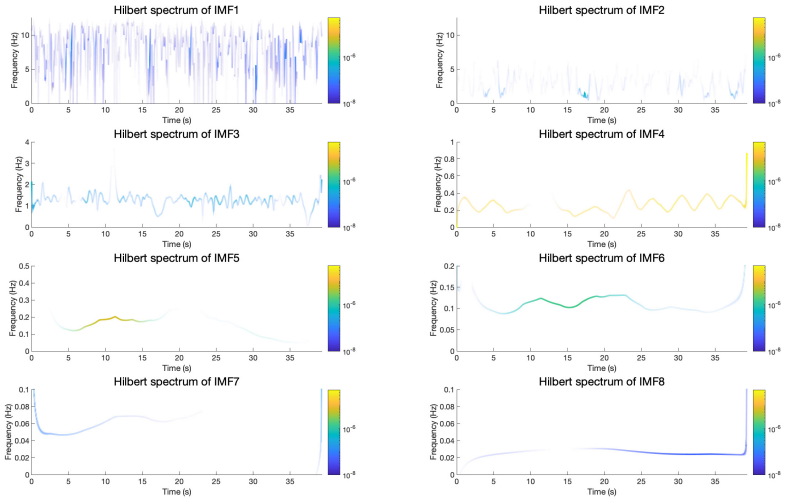

Figure 3.3: Hilbert spectrum of IMFs obtained by EMD

3.3. ENSEMBLE EMPIRICAL MODE DECOMPOSITION

EMD is an adaptive, widely-used and highly efficient signal decomposition method, however, it suffers from the deficiency of mode mixing. Usually, mode mixing occurs when the input signal is obtained by a high-frequency signal, especially an intermittent high-frequency signal added to a low-frequency signal (see in Fig. 3.4(a)). When mode mixing happens, IMF contains tremendously different scales of oscillations, or similar time scales reside in different IMFs. Ensemble empirical mode decomposition (EEMD) was proposed by Wu and Huang in 2009 to overcome the shortage of EMD [58].

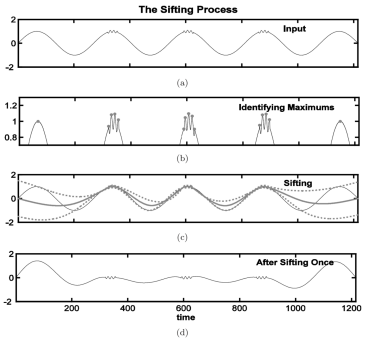

Figure 3.4: Mode mixing problem

The principle of EEMD relies on adding white noise to the original signalwhich will uniformly fill in the entire time-frequency space of signal with components of different scales [59]. The added noise populates the signal, thus making the signal not intermittent and alleviating the mode mixing problem.

Although extra noise is added to the original signal, the sets of zero-mean white Gaussian noise cancel each other out in the spatial-temporal overall mean. Eventually, it is the original signal that is the only consistent part as a sufficient large number of trials are tested. So, the average of trails can be considered as the final result of EEMD. The concepts of EEMD are given as [58]:

1. Build N realizations of white Gaussian noise and add them to input signal one by one, obtaining a collection of noisy signals:

$$s^i(t) = s(t) + w^i(t), \tag{3.11}$$

   where $s(t)$ denotes the signal to be decomposed and $w_i(t)$ is the ith independent realization of zero-mean white Gaussian noise, $i = 1,2,\ldots,N$.

2. Conduct empirical mode decomposition to every noisy signal $s^i(t), i = 1,2,\ldots N$, and obtain a set of $\mathrm{IMF}_k^i, k = 1,2,\ldots K$.

3. Calculate ensemble mean of the decomposed IMFs:

$$\widetilde{\mathrm{IMF}}_k = \frac{1}{N}\sum_{i=1}^{N} \mathrm{IMF}_k^i. \tag{3.12}$$

Fig. 3.5 is an example of EEMD result from noisy respiration and heartbeat signals. We can see from this figure that there are more modes obtained by EEMD than EMD because of adding extra white noise. The mode mixing issue in EMD is alleviated in EEMD. From the Hilbert spectrum of IMFs from EEMD in Fig. 3.6, it can be found that IMF3 represents the heartbeat signal since most of its instantaneous frequencies change between 1-1.5Hz, and Hilbert spectrum of IMF4 resides around 0.25Hz, representing respiration signal.

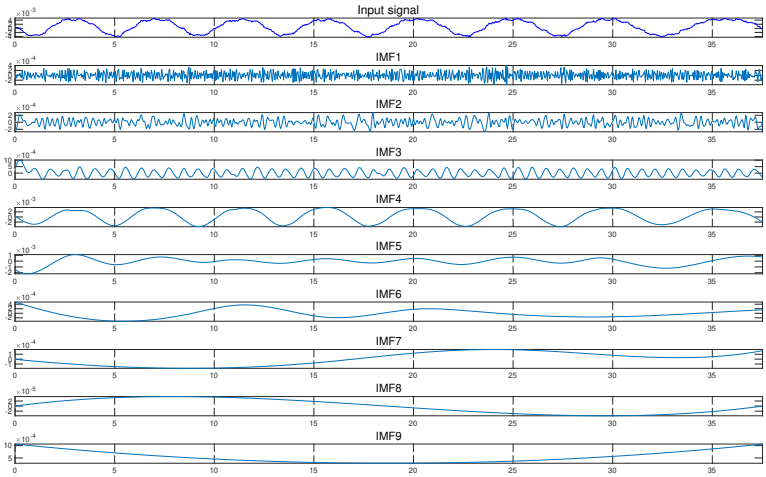

Figure 3.5: The resulting EEMD components from noisy vital signs

3.4. COMPLETE ENSEMBLE EMPIRICAL MODE DECOMPOSITION WITH ADAPTIVE NOISE

EEMD resolves the problem of mode mixing in EMD, however, it introduces new issues. The reconstructed signal still contains the residual noise component. A new method named complete ensemble empirical mode decomposition with adaptive noise (CEEMDAN) was proposed, providing better separation of IMFs [37]. CEEMDAN was developed as an improvement over the EEMD algorithm, with a reduced number of sifting iterations and lower computational cost.

CEEMDAN algorithm [37] is described by following steps with $s(t)$ as the input signal:

1. Decompose I realizations of $s(t)+\sigma_0 w^i(t), i=1,\ldots,I$ by EMD, the first mode of CEEMDAN $\widetilde{\text{IMF}}_1$ will be computed as:

$$\widetilde{\text{IMF}}_1 = \frac{1}{I}\sum_{i=1}^{I} \text{IMF}_1^i, \tag{3.13}$$

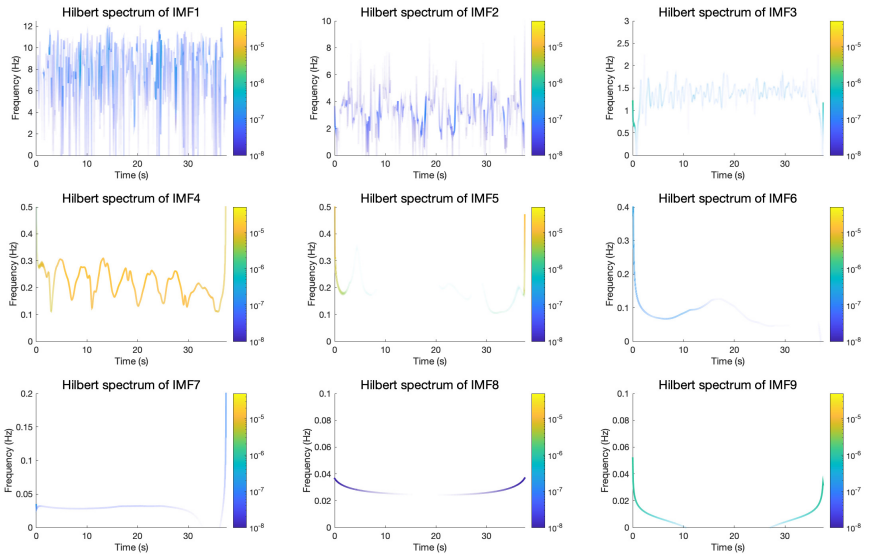

Figure 3.6: Hilbert spectrum of IMFs obtained by EEMD

where $w^i \sim \mathcal{N}(0,1)$, σ_0 is the standard deviation of noise, I denotes the number of realizations.

2. Calculate the kth residue for $k = 1,\ldots,K$:

$$r_k(t) = r_{k-1}(t) - \widetilde{\mathrm{IMF}}_k(t), \qquad r_0(t) = s(t). \tag{3.14}$$

3. Decompose realizations $r_k(t) + \sigma_k E_k(w^i(t)), i = 1,\ldots,I,$, the $(k+1)$th mode is defined as:

$$\widetilde{\mathrm{IMF}}_{k+1} = \frac{1}{I}\sum_{i=1}^{I} E_1(r_k(t) + \sigma_k E_k(w^i(t))). \tag{3.15}$$

4. Go back to Step 2 for next iteration k until the obtained residue is no longer feasible to be decomposed.

One example of CEEMDAN can be seen in Fig. 3.7, the input signal is identical to the ones in EMD and EEMD. CEEMDAN alleviates the mode mixing problem in EMD. And with the same number realizations of noise added, its execution time is 6.21 seconds while the execution time of EEMD is 9.78 seconds, showing a lower computational cost.

The Hilbert spectrum of IMFs decomposed by CEEMDAN are shown in Fig. 3.8. From the time-frequency distribution, IMF4 is considered as the heartbeat signal and IMF6 is the respiration signal.

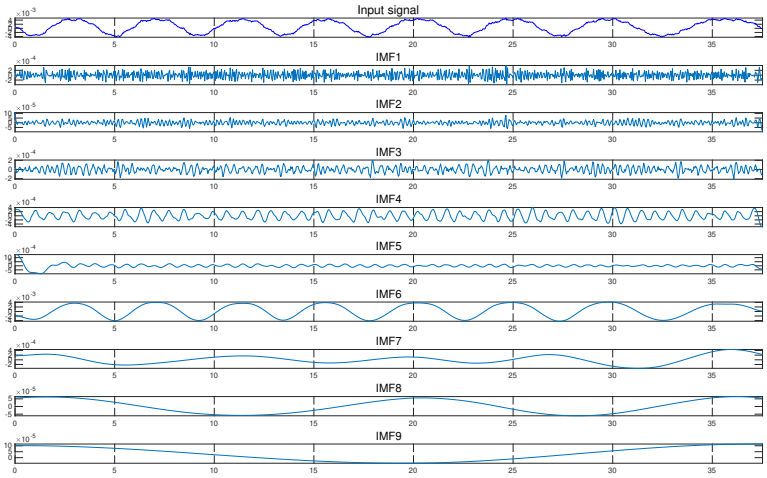

Figure 3.7: The resulting CEEMDAN components from noisy vital signs

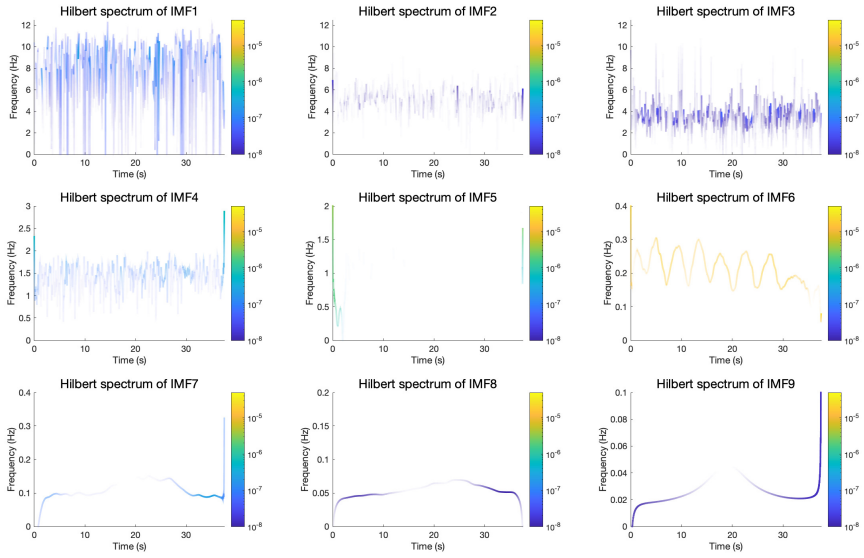

Figure 3.8: Hilbert spectrum of IMFs obtained by CEEMDAN

3.5. VARIATIONAL MODE DECOMPOSITION

Variational mode decomposition (VMD) is a kind of algorithm in which the modes are extracted concurrently [38]. The objective of variational mode decomposition algorithm

is to obtain the optimal solution through iteration, so as to determine the center frequency and bandwidth of each mode component [38]. Each mode u_k is mostly concentrate around central frequency ω_k, and the sum of every component bandwidths is the smallest [60]. Different from the definition of the intrinsic mode function of EMD algorithm, the intrinsic mode function of the VMD algorithm is an amplitude-frequency modulation signal:

$$u_k(t) = A_k(t)\cos(\phi_k(t)) \tag{3.16}$$

where $u_k(t)$ is the intrinsic mode function in VMD, $A_k(t)$ denotes the amplitude of envelope and it is non-negative, the phase $\phi_k(t)$ is non-decreasing, and it should be noted that both amplitude $A_k(t)$ and instantaneous frequency $\omega_k(t) = d\phi_k(t)/dt$ vary much slower than the phase $\phi_k(t)$, that is, the mode u_k can be regarded as a pure harmonic signal on a sufficiently long interval $[t-\delta, t+\delta]$, $\delta \approx 2\pi/\phi_k^{'}(t)$ [61].

The aim of VMD algorithm is to search for k IMFs with limited bandwidths and different center frequencies, also the sum of the bandwidths should be the smallest [62]. There are two major parts involved in VMD, the construction and solution of the variational problem, each of them will be explained in detail.

The steps of variational problem construction is described as follows [38]:

1. The analytic signal of each intrinsic mode function $u_k(t)$ is calculated by Hilbert transform, obtaining a single-sided frequency spectrum:

$$u_{k,A}(t) = \left(\delta(t) + \frac{j}{\pi t}\right) * u_k(t), \tag{3.17}$$

   where is δ denotes Dirac function and $*$ stands for the convolution operation.

2. Multiply the analytic signal and harmonic signal with central frequency ω_k:

$$\left[\left(\delta(t) + \frac{j}{\pi t}\right) * u_k(t)\right] e^{-j\omega_k t}. \tag{3.18}$$

   By doing which, the spectrum kth mode is shifted to baseband.

3. Find the squared L^2-norm of the gradient in (3.18), and estimate from this bandwidth of each IMF can be estimated from this. The resulting constrained variational problem is expressed as:

$$\min_{\{u_k\},\{\omega_k\}} \left\{ \sum_{k=1}^{K} \left\| \partial_t \left[\left(\delta(t) + \frac{j}{\pi t}\right) * u_k(t)\right] e^{-j\omega_k t} \right\|^2 \right\}, \tag{3.19}$$

   where $\{u_k\} := \{u_1, \ldots, u_K\}$ and $\{\omega_k\} := \{\omega_1, \ldots, \omega_K\}$ denote collections of K IMFs and their center frequencies, respectively.

The variational problem can be settled in different ways. Here, the steps of the solution from [38] are demonstrated as:

1. Firstly, quadratic penalty term and Lagrangian function are introduced, converting the unconstrained minimization problem in (3.19) to a constrained one:

$$\mathcal{L}(\{u_k\},\{\omega_k\},\lambda) = \alpha \sum_{k=1}^{K} \left\| \partial_t \left[\left(\delta(t) + \frac{j}{\pi t} \right) * u_k(t) \right] e^{-j\omega_k t} \right\|^2 + \left\| s(t) - \sum_{k=1}^{K} u_k(t) \right\|^2 + \left\langle \lambda(t), s(t) - \sum_{k=1}^{K} u_k(t) \right\rangle, \tag{3.20}$$

where α is the penalty coefficient, $\lambda(t)$ is the Lagrange multiplier, $s(t)$ is the input signal.

2. The issue remains to be addressed for now is a convex optimization problem, which can be tackled by alternating direction method for multipliers (ADMM), detain of the algorithm can be seen in Algorithm 1 [38]:

Algorithm 1 ADMM optimization steps for VMD

Initialize $\{u_1\}$, $\{\omega_1\}$, λ_1, $n \leftarrow 0$
repeat
  $n \leftarrow n+1$
  for $k = 1 : K$ **do**
    Update u_k:
    $u_k^{n+1} \leftarrow \arg\min_{u_k} \mathcal{L}\left(\{u_{i<k}^{n+1}\},\{u_{i\geq k}^{n}\},\{\omega_i^n\},\lambda^n\right)$
  end for
  for $k = 1 : K$ **do**
    Update ω_k:
    $\omega_k^{n+1} \leftarrow \arg\min_{\omega_k} \mathcal{L}\left(\{u_i^{n+1}\},\{\omega_{i<k}^{n+1}\},\{\omega_{i\geq k}^{n+1}\},\lambda^n\right)$
  end for
  Dual ascent:
    $\lambda^{n+1} \leftarrow \lambda^n + \tau\left(s - \sum_k u_k^{n+1}\right)$
until convergence: $\sum_k \left\| u_k^{n+1} - u_k^n \right\|_2^2 / \left\| u_k^n \right\|_2^2 < \epsilon$

3. However, there are sub-optimization problems remain in ADMM algorithm. By applying ADMM to update the modes, u_k^{n+1} can be written as:

$$u_k^{n+1} = \arg\min_{u_k} \left\{ \alpha \left\| \partial_t \left[\left(\delta(t) + \frac{j}{\pi t} \right) * u_k(t) \right] e^{-j\omega_k t} \right\|_2^2 + \left\| s(t) - \sum_i u_i(t) + \frac{\lambda(t)}{2} \right\|_2^2 \right\}. \tag{3.21}$$

4. The problem in (3.21) can be transformed to spectral domain using the Parseval

Fourier isometry under L^2-norm, shown as follows:

$$\hat{u}_k^{n+1} = \arg\min_{\hat{u}_k} \Big\{ \alpha \| j\omega[1+\mathrm{sgn}(\omega+\omega_k)\cdot\hat{u}_k(\omega+\omega_k)]\|_2^2 + \Big\| \hat{s}(\omega) - \sum_i \hat{u}_i(\omega) + \frac{\hat{\lambda}(\omega)}{2} \Big\|_2^2 \Big\}, \tag{3.22}$$

where $\mathrm{sgn}(\cdot)$ represents the sign function defined as:

$$\mathrm{sgn}(x) = \begin{cases} -1 & \text{if } x<0, \\ 0 & \text{if } x=0, \\ 1 & \text{if } x>0. \end{cases}$$

5. Substitute ω in the first term of (3.22) by $\omega-\omega_k$, we can get:

$$\hat{u}_k^{n+1} = \arg\min_{\hat{u}_k} \Big\{ \alpha \| j(\omega-\omega_k)[1+\mathrm{sgn}(\omega)\cdot\hat{u}_k(\omega)]\|_2^2 + \Big\| \hat{s}(\omega) - \sum_i \hat{u}_k(\omega) + \frac{\hat{\lambda}(\omega)}{2} \Big\|^2 \Big\}. \tag{3.23}$$

6. Rewrite the term in (3.23) as half-space integrals using the Hermitian symmetry of the real signals in the reconstruction fidelity term:

$$\hat{u}_k^{n+1} = \arg\min_{\hat{u}_k} \Big\{ \int_0^\infty 4\alpha(\omega-\omega_k)^2 |\hat{u}_k(\omega)|^2 + 2\Big| \hat{s}(\omega) - \sum_i \hat{u}_i(\omega) + \frac{\hat{\lambda}(\omega)}{2} \Big|^2 d\omega \Big\}. \tag{3.24}$$

7. The above quadratic optimization problem is solved by letting the first variation vanish for the positive frequencies, which means:

$$\hat{u}_k^{n+1}(\omega) = \frac{\hat{s}(\omega) - \sum_i \hat{u}_i(\omega) + \frac{\hat{\lambda}(\omega)}{2}}{1+2\alpha(\omega-\omega_k)^2}. \tag{3.25}$$

8. The same method is exploited to update the center frequency of the intrinsic mode functions ω_k, the iterative formula is:

$$\omega_k^{n+1} = \frac{\int_0^\infty \omega |\hat{u}_k(\omega)|^2 d\omega}{\int_0^\infty |\hat{u}_k(\omega)|^2 d\omega}. \tag{3.26}$$

9. Since we have the solutions to sub-optimizations in ADMM algorithm as shown in Algorithm 1, the complete optimization algorithm of VMD is described in Algorithm 2 [38].

Algorithm 2 Complete optimization steps for VMD

Initialize $\{u_1\}$, $\{\omega_1\}$, λ_1, $n \leftarrow 0$
repeat
  $n \leftarrow n+1$
  for $k = 1 : K$ **do**
    Update u_k for all $\omega \geq 0$:
      $u_k^{n+1} \leftarrow \left(\hat{s}(\omega) - \sum_{i<k} \hat{u}_i^{n+1}(\omega) - \sum_{i>k} \hat{u}_i^{n}(\omega) + \frac{\hat{\lambda}^n(\omega)}{2}\right) \Big/ \left(1 + 2\alpha(\omega - \omega_k^n)^2\right)$
    Update ω_k:
      $\omega_k^{n+1} \leftarrow \left(\int_0^\infty \omega |\hat{u}_k^{n_1}(\omega)|^2 d\omega\right) / \left(\int_0^\infty |\hat{u}_k^{n_1}(\omega)|^2 d\omega\right)$
  end for
  Dual ascent for all $\omega \geq 0$:
    $\hat{\lambda}^{n+1}(\omega) \leftarrow \hat{\lambda}^n(\omega) + \tau\left(\hat{s}(\omega) - \sum_k \hat{u}_k^{n+1}(\omega)\right)$
until convergence: $\sum_k \left\| u_k^{n+1} - u_k^n \right\|_2^2 / \left\| u_k^n \right\|_2^2 < \epsilon$

It requires some manually setting of the parameters before applying VMD algorithm to obtain IMFs:

(a) Penalty coefficient α: it can affect the bandwidth of the intrinsic mode function. The larger the value, the faster the attenuation on both sides of the central frequencies will be.

(b) Time step of the dual ascent τ: used to solve the convex optimization problem, the value is typically chosen under 1 and can be set to zero when there is strong noise.

(c) The number of modes to be recovered K.

(d) Tolerance of convergence criterion ϵ: typically set around 1×10^6.

The result of VMD is depicted in Fig. 3.9. Unlike EMD algorithms, the lower order IMFs in VMD represent rapidly varying signal components. So the respiration signal, which has the lowest frequency in the original signal, is the first decomposed mode. The heartbeat signal is represented by IMF2. The verification can be seen in Fig. 3.10, which describes the instantaneous frequencies of IMFs. We can see the frequency distributions of IMF1 and IMF2 correspond to the frequency ranges of respiration and heartbeat, respectively.

3.6. NUMERICAL SIMULATIONS

Four signal decomposition methods have been discussed. Methods could be adversely affected by certain circumstances. Therefore, the performances of signal decomposition methods in vital signs monitoring under disparate conditions need to be assessed. It is hard to extract the heartbeat signal with the presence of noise and auto vibration since it is much weaker than the respiratory signal and has a relatively close frequency component with auto vibration. In this case, only the result of respiration signal extraction will be evaluated. The extracted respiration signal is determined by the amplitude and frequency of the decomposed IMF. The IMF corresponding to the respiration should have

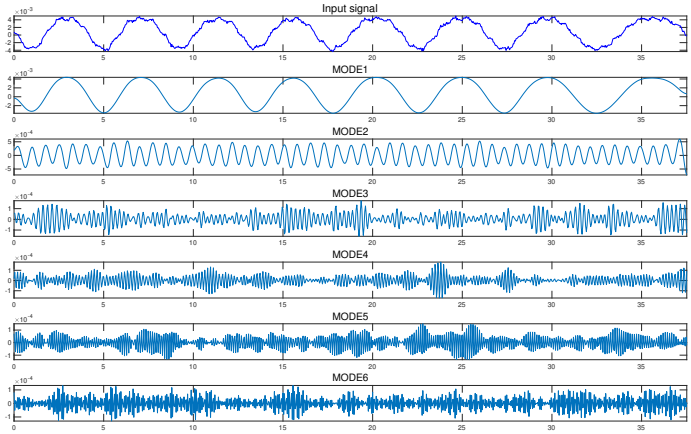

Figure 3.9: The resulting VMD components from noisy vital signs

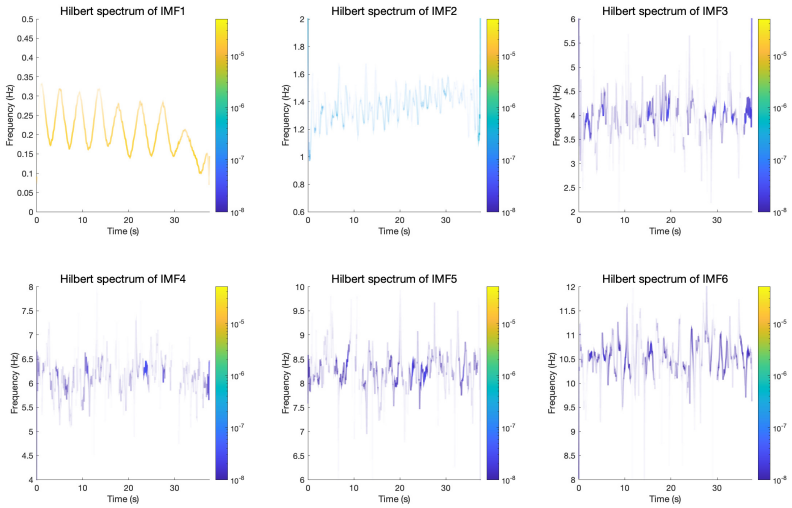

Figure 3.10: Hilbert spectrum of IMFs obtained by VMD

the largest amplitude and the frequency distribution should fall into the typical respiratory frequency range. Owing to the dynamic performance of cardiopulmonary signals, noise and vibration waveforms, Monte Carlo simulation is a reliable method used to assess different signal decomposition results under diverse signal-to-noise ratio conditions and vibration amplitudes through a large number of repeated experiments [63].

Here, two evaluation metrics are applied to assess the performance of empirical and

variational mode decomposition algorithms. The first is the signal-to-noise ratio of estimated respiration signal. We treat the difference between the original signal and the estimated signal as noise, the SNR of estimated respiration signal is thus calculated as:

$$SNR = 10\log_{10}\left(\frac{P_s}{P_n}\right), \tag{3.27}$$

where P_s is original respiration signal power and P_n is noise power.

The second metric is the root mean square error of frequency:

$$RMSE_f = \sqrt{\frac{1}{N}\sum_{i=1}^{N}(\hat{\mathbf{f}}_\mathbf{r} - \mathbf{f}_\mathbf{r})^2}, \tag{3.28}$$

where N is the number of samples, $\mathbf{f}_\mathbf{r} = [f_{r,1}, \ldots, f_{r,N}]$ is a N dimensional vector representing instantaneous frequencies of original respiration signal; $\hat{\mathbf{f}}_\mathbf{r} = [\hat{f}_{r,1}, \ldots, \hat{f}_{r,N}]$ denote N instantaneous frequencies of estimated respiration signal.

Fig. 3.11 and 3.12 are the performance assessments under different input SNR level when only white Gaussian noise is added to the vital signs. The input SNR shows the difference in energy level between the original signal and the added white noise. In contrast to our common intuition, the SNR of reconstructed respiration signal (seen in Fig.3.11) does not monotonically grow with the increase of input SNR. We notice that EEMD performs better than CEEMDAN under the condition of low input SNR, but CEEMDAN is more promising in higher input SNR cases. In general, VMD is the most robust method to noise while EMD is the least stable method against noise. When it comes to the estimation of SNR of reconstructed respiration signal, the best accuracy is achieved by VMD when the input SNR is 27dB, with which the highest SNR of reconstructed respiration is 25dB. The most accurate result of other methods is about 20dB, when the input SNR is around 30dB.

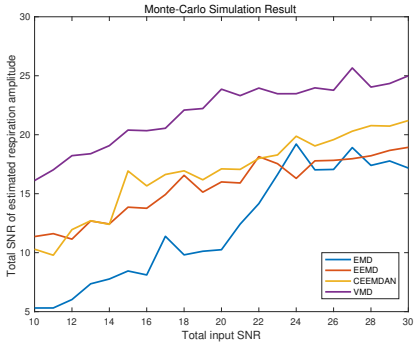

Figure 3.11: SNR of reconstructed respiration signal

RMSE of estimated frequency is studied in Fig. 3.12, the curves of different methods show downward trends. In most SNR cases, EEMD supplies the best estimation of respiratory instantaneous frequencies in noisy signals. Whereas for EEMD in high SNR

case, due to the presence of additional white noise added in the algorithm, the decomposed respiration signal will have residual noise components. The noise components might have a higher level than the environment noise, leading to a large RMSE value. It also should be noted that RMSE of estimated frequency in VMD hardly changes with increasing signal-to-noise ratio, revealing the robustness of VMD to noise. When the signal-to-noise ratio is within the range of 10-20dB, the error of EMD and CEEMDAN frequency estimation generally decreases with the improvement of input SNR. Although CEEMDAN have worse performance than EEMD at most SNR levels, the RMSE of CEEMDAN goes beyond EEMD algorithm when input SNR is near 30dB. The peak of accuracy of estimated respiration frequency happens when the input SNR is higher than 15dB for all these methods. The minimum RMSE of EMD is about 0.075 and it is 0.06-0.065 for the other three methods.

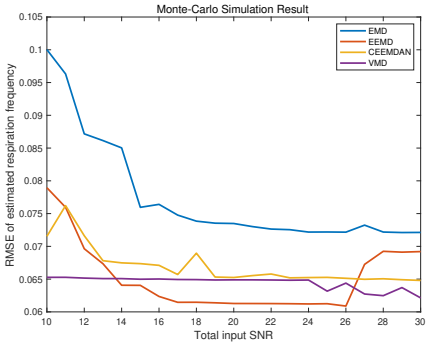

Figure 3.12: RMSE of estimated respiration frequency

Next, we investigate the impact of auto vibration level on four signal decomposition algorithms. The waveform of auto vibration is depicted in Fig. 3.13, in which clutter-to-noise ratio and signal-to-noise ratio are both 20dB.

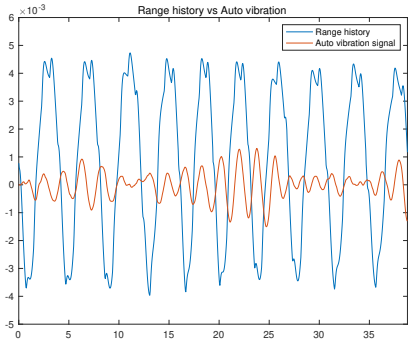

Figure 3.13: The waveform of auto vibration vs range history

When eliminating the interference of environmental noise, we concentrate our attention on studying the impact of auto vibration level on different signal decomposition algorithms. Simulation results are shown in Fig. 3.14 and 3.15.

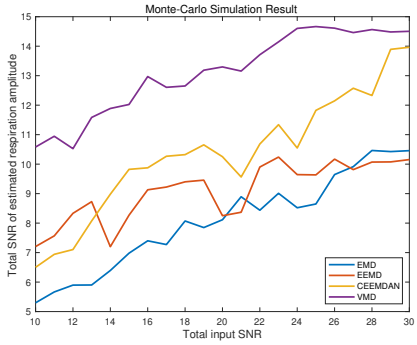

Figure 3.14: SNR of reconstructed respiration signal

Similar to previous conclusion when only environment noise is presented, the SNR of reconstructed respiration signal does not increase monotonously when the input signal-to-noise ratio raises, as can be observed in Fig. 3.14. In this comparison, VMD performs best, followed by CEEMDAN, EEMD and EMD, and the performance ranking does not change with the input SNR.

In addition, as can tell from Fig. 3.15, VMD and CEEMDAN always have lower error than EMD and EEMD when estimating the instantaneous frequencies of respiration signal. A conclusion can be drawn that VMD is usually the best decomposition algorithm option when vibration is presented. The most accurate estimation is attained by all the methods with the largest input SNR, the SNR of the reconstructed signal using CEEMDAN and VMD is 14dB and it is 9.5dB for EMD and EEMD methods, the RMSE of estimated frequency for CEEMDAN and VMD is about 0.75 and it is 0.1 when performing EMD and EEMD.

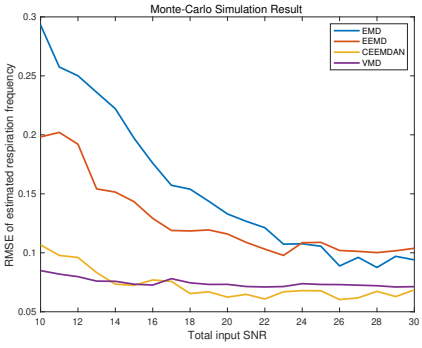

Figure 3.15: RMSE of estimated respiration frequency

3.7. CONCLUSION

In this chapter, we describe the design and implementation of three empirical and one variational mode decomposition algorithm. All methods are applicable to vital signs monitoring and estimation of signal parameters. Hilbert transform is applied to IMFs after signal decomposition, to acquire time-frequency spectrum and instantaneous frequencies of each mode thus obtained.

Analysis of the proposed techniques with numerical simulations have demonstrated that EEMD is more applicable in a noisy environment aiming to estimate instantaneous frequency of the reconstructed signal, its high estimation accuracy is achieved as a RMSE of 0.06 when the input SNR is 25dB. VMD is more eligible when referring to the estimation of instantaneous amplitude, by applying VMD method, the SNR of reconstructed respiration signal is up to 25dB. CEEMDAN and VMD are both suitable approaches in presence of auto vibration, the most accurate estimation is obtained with the vibration of 30dB SNR.

4

ONLINE SIGNAL DECOMPOSITION METHODS

In the previous chapter, empirical and variational signal decomposition methods have been discussed and compared. These signal decomposition methods have not dealt with the condition of data stream, when new samples are continuously added to the data set, and processed jointly. The existing literature on online empirical mode decomposition (Online-EMD) [64] [65] employs a sliding window and stitching procedure, achieving dynamic decomposition of data stream. In this chapter, we show the feasibility of executing the same technique in variational mode decomposition to handle data with increasing length, nominated as Online-VMD algorithm.

The first section of this chapter illustrates the approach to achieve the online decomposition of data stream. It will then go on to the evaluation and comparison of online-EMD and VMD. EEMD and CEEMDAN both seek to obtain IMFs by averaging the modes decomposed by a number of realizations of extra noise added to the original signal. These two methods are well-behaved solutions of mode-mixing problem but it takes much longer time than EMD due to the averaging procedure. So, EEMD and CEEMDAN are not considered for online decomposition here.

4.1. ONLINE SIGNAL DECOMPOSITION PRINCIPLE

Online-EMD aims at extracting IMFs from data of unfixed length. In this algorithm, a sliding window that encompasses a certain number of extrema is applied to obtain local IMFs, then a window function and stitching procedures are performed, accumulating local IMFs to the global ones [64]. The concept of the sliding window and stitching procedure in Online-EMD is shown in Fig. 4.1.

The online empirical signal decomposition algorithm is shown as follows:

1. Initialization: set number of iteration $i = 1$, total weights $\Phi^0(t) = 0$, the starting position of the signal $p_1 = 0$ and let initial IMF $\bar{M}$ equals zero.

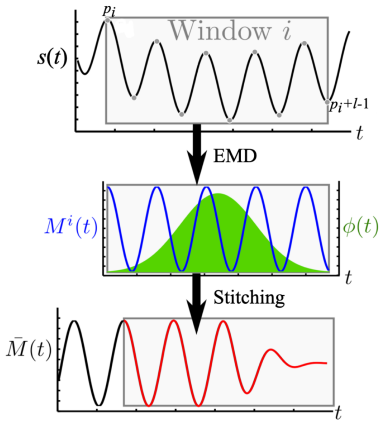

Figure 4.1: Overview of Online-EMD sliding window and stitching procedure

2. Determine the starting window, which encompasses l serial local extrema $\{p_1,\ldots,p_l\}$ of the original signal $s(t)$.

3. Implement empirical mode decomposition algorithm to separate the first IMF $M^i(t)$ of current window, the signal component that varies fastest.

4. Now there are $l^{'}$ positions of extrema in M^i and they are denoted as $\{p_1^{'},\ldots,p_l^{'}\}$. Weight function $\tilde{\phi}(t)$ on $[-\tau,\tau]$ (and 0 outside) is utilized in stitching procedure as:

$$\tilde{\phi}(t)=\frac{1}{\sqrt{2\pi}}\exp\left(-\frac{t^2}{2}\right)-\frac{1}{\sqrt{2\pi}}\exp\left(-\frac{\tau^2}{2}\right), \tag{4.1}$$

with which we attempt to restrain the discontinuity caused by boundary error.

Set $s_k=-\tau+2(k-1)\tau/(l^{'}-1)$ for $k\in\{1,\ldots,l^{'}\}$. A new defined weight function called warped weights $\phi_k(t)$ is expressed as:

$$\phi_k(t)=\tilde{\phi}\left(s_k+(s_{k+1}-s_k)\frac{t-e_k^{'}}{e_{k+1}^{'}-e_k^{'}}\right), \tag{4.2}$$

where $k\in\{1,\ldots,l^{'}-1\}$ in warped weight and $t\in[e_k^{'},e_{k+1}^{'}]$. Note that zero is still not contained in the domain of function. As warped wight function is obtained, weighted IMF $\hat{M}^i$ is shown as follows:

$$\hat{M}^i(t)=\left(\phi_1(t)\hat{M}_1^i(t),\ldots,\phi_{l^{'}-1}(t)\hat{M}_{l^{'}-1}^i(t)\right), \tag{4.3}$$

where $M_k^i(t)$ denotes the local IMF between two adjacent extrema, $e_k^{'}\leqslant t<e_{k+1}^{'}$. Moreover, the sum of weights is saved as:

$$\Phi^i(t)=\Phi^{i-1}(t)+\sum_{k=1}^{l^{'}-1}\phi_k(t). \tag{4.4}$$

5. Stitch $\hat{M}^i$ on the previously decomposed weighted IMFs:

$$\bar{M} = \bar{M} + \hat{M}^i, \tag{4.5}$$

then normalize local IMF who will not encompassed in the sliding window of next iteration:

$$\bar{M} = \bar{M}/\Phi^i(t). \tag{4.6}$$

6. Subtract the newly identified IMF portion $\bar{M}(t)$ from the input data of current iteration $s^i(t)$:

$$r^i(t) = s^i(t) - \bar{M}(t), \quad t \in [e_i, e_{i+1}]. \tag{4.7}$$

The residual r_i is used as the input signal so as to extract subsequent IMF.

7. Increase i to $i+1$ and go back to Step 2, until the number of remaining extrema in original signal is less than window size l.

The principles of Online-VMD are similar to Online-EMD, which are also sliding windows and stitching procedures. But in VMD, the sliding window encompasses a certain number of sampling points, instead of a specific number of extrema. Also, VMD can concurrently decompose the data contained in a sliding window into K local modes, and then use the weight function to accumulate the local modes into the global one. The differences of Online-EMD and Online-VMD are summarized in Tab. 4.1.

Difference	Online-EMD	Online-VMD
Sliding window content	Extrema	Sampling points
Mode decomposition way	Iterative	Concurrent

Table 4.1: Differences between Online-EMD and Online-VMD

4.2. SIMULATION EXAMPLES OF ONLINE DECOMPOSITION

Online empirical mode decomposition considers the signal to be composed of intrinsic mode functions, while online variational modal decomposition considers the signal consisting of sub-signals dominated by different frequencies. The simulation results of vital signs monitoring in noisy case using Online-EMD and Online-VMD are shown in Fig. 4.2 and 4.3, respectively. In this simulation, frequency of the input respiration signal is 0.25Hz while heartbeat signal is 1.3Hz.

Now the Online-EMD/VMD simulation results of respiration and heartbeat signal extraction in noisy environment are obtained, Hilbert-Huang transform is essential to analysis and determine which IMFs are desired vital sign signals. Hilbert spectrum of IMFs obtained by Online-EMD is depicted in Fig. 4.4, obtained by Online-VMD can be seen in Fig. 4.5.

By observing the Hilbert spectrum in Fig. 4.4, we can see that the time-frequency distribution of IMF3 is roughly consistent with the original heartbeat signal. It can be seen that the instantaneous frequency of IMF4 is mainly distributed in the range of 0.2-0.3Hz, corresponds to the original respiration signal. Based on this, it can be determined

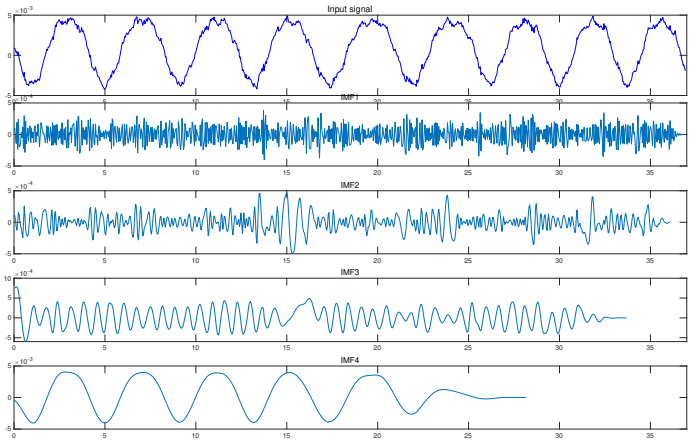

Figure 4.2: The resulting Online-EMD components from noisy vital signs

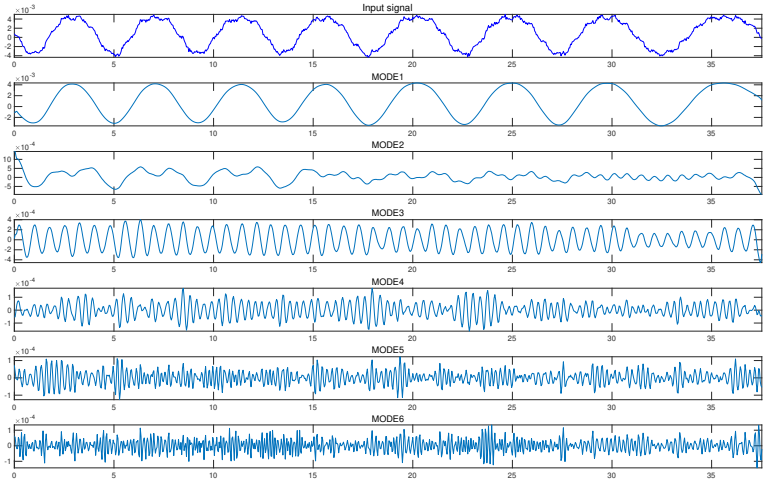

Figure 4.3: The resulting Online-VMD components from noisy vital signs

that IMF3 and IMF4 are the extracted heartbeat and respiration signal, respectively. The extracted heartbeat signal is mixed with noise and vibration components.

Unlike Online-EMD, which first decomposes the high-frequency components, the instantaneous frequencies of the first mode extracted by Online-VMD (see Fig. 4.5) is between 0.2-0.3Hz, so it is considered as the respiration signal. The curve in Hilbert spectrum of IMF3 fluctuates around 1.3Hz, representing the extracted heartbeat signal.

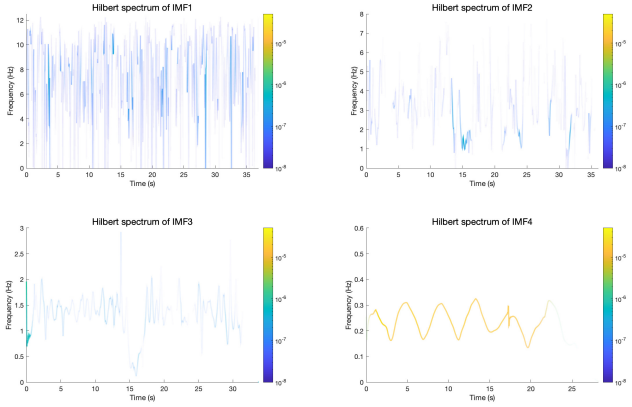

Figure 4.4: Hilbert spectrum of IMFs obtained by Online-EMD

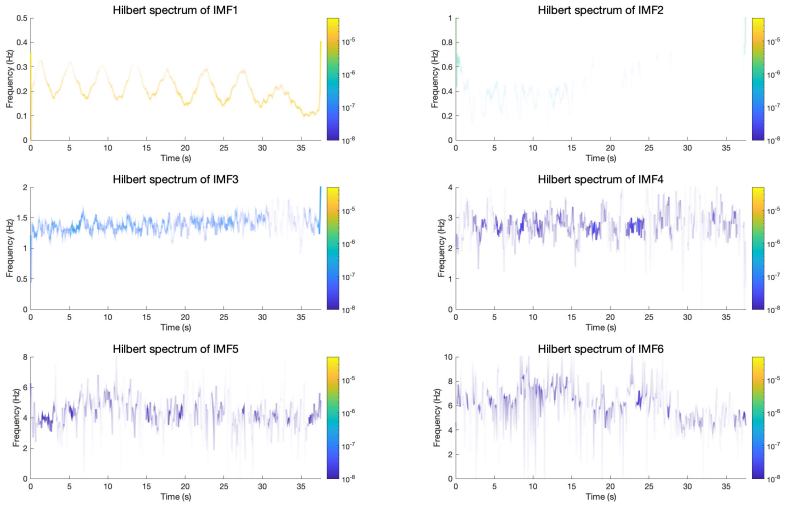

Figure 4.5: Hilbert spectrum of IMFs obtained by Online-VMD

With the presence of both environmental noise and auto vibration, Fig. 4.6 and 4.8 respectively display the result of vital signs decomposition using Online-EMD and Online-VMD. The Hilbert spectrum of Online-EMD/VMD decomposition results are shown in Fig. 4.7 and 4.9.

It can be seen from Fig. 4.7 that mode mixing problem occurs in IMF3 and IMF4 under the interference of noise and vibration. However, we can still determine that the original heartbeat signal can be represented by IMF3 and the respiration signal resides

in IMF4 from the Hilbert spectrum.

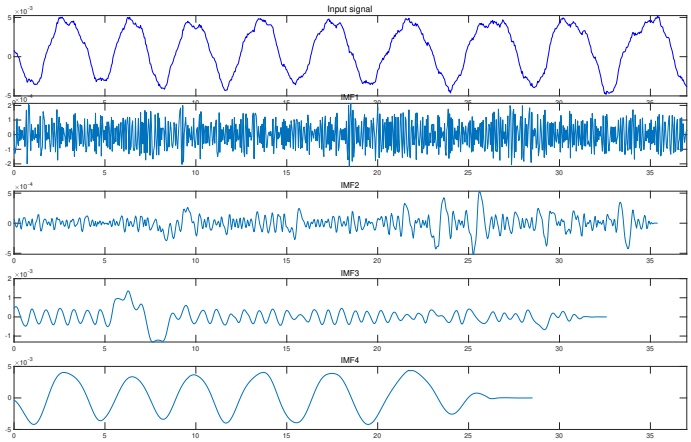

Figure 4.6: The resulting Online-EMD components from vital signs with noise and vibration

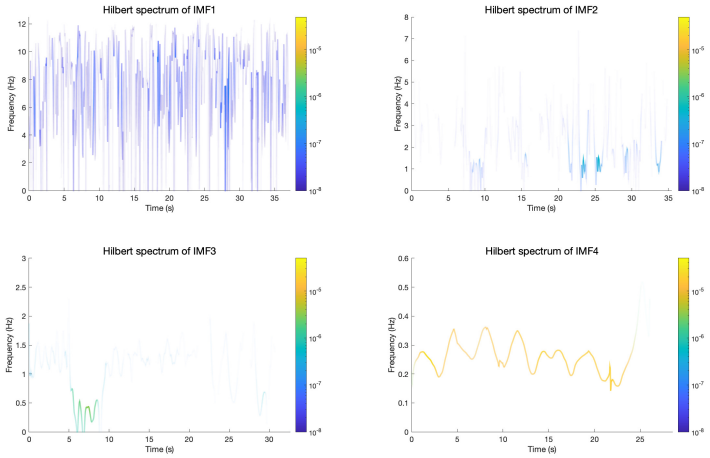

Figure 4.7: Hilbert spectrum of IMFs obtained by Online-EMD

Fig. 4.8 illustrates Online-VMD has a good extraction effect on vital signs in an environment with noise and vibration since no mode mixing happens. The same conclusion is confirmed in Fig. 4.9, as the instantaneous frequencies of IMF1 are around 0.25Hz, and instantaneous frequencies of IMF3 are around 1.3Hz. Therefore, IMF1 and IMF3 can be determined as the extracted respiration signal and heartbeat signal, respectively.

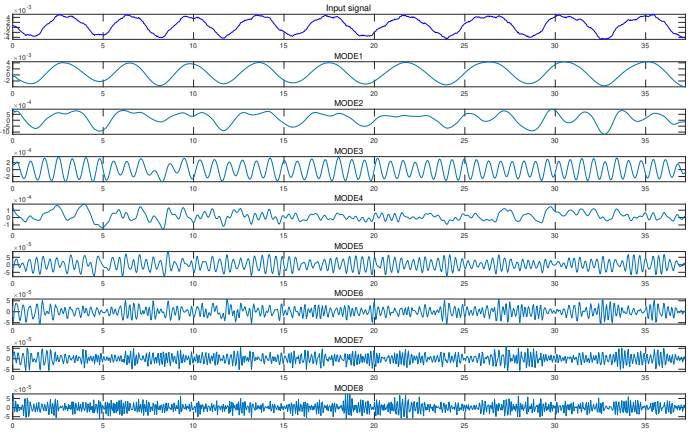

Figure 4.8: The resulting Online-VMD components from vital signs with noise and vibration

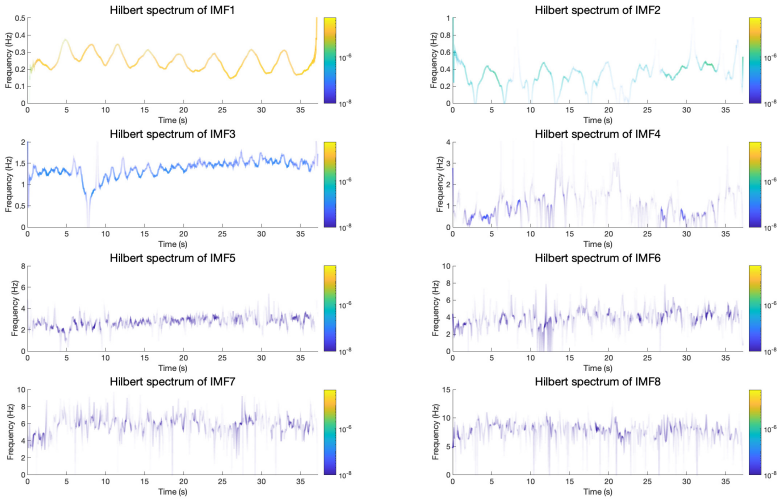

Figure 4.9: Hilbert spectrum of IMFs obtained by Online-VMD

Based on what has been acquired from the above simulation results, some discussion is given as follows:

1. Similar to conventional EMD, Online-EMD is also affected by mode mixing problem. IMF3 and IMF4 shown in Fig. 4.6 both contains respiratory component. However, EEMD and CEEMDAN algorithms cannot be introduced to resolve mode

mixing problem due to the conflict between the real-time requirement of the online decomposition algorithm and their long execution time.

2. Owing to the limitation of the sliding window in Online-EMD, the length of the decomposed mode decreases as the order increases. But Online-VMD overcomes this shortcoming, the modes obtained in Online-VMD have the same length as the input signal. The target respiration signal of Online-EMD is the higher order IMF since the respiration signal has a relatively low frequency component, therefore, the extracted respiration signal length in Online-EMD is always shorter than in Online-VMD.

3. When noise and auto vibration are present, the heartbeat signal is easily disturbed by them, and mode mixing is prone to occur in Online-EMD. But VMD does not suffer from these, and it can achieve a good performance of vital signs extraction. Under this circumstance, it is reasonable to tell that Online-VMD is more robust to noise and vibration than Online-EMD.

4.3. NUMERICAL SIMULATIONS

Monte Carlo simulation is also used in this chapter to assess the two kinds of online signal decomposition algorithms with the presence of environmental noise and auto vibration through 200 repeated experiments. Here, attention is focused on the effect of processed signal length on the performance of two algorithms. The same two evaluation metrics as used in Section 3.6, SNR of the reconstructed signal, as defined in (3.27), as well as the root-mean-square error of frequency are applied to evaluate the performance of Online-EMD/VMD.

Fig. 4.10 provides information on how SNR of reconstructed respiration signals in Online-EMD and Online-VMD vary with time. It can be observed that the SNR of decomposed respiration signals in the two algorithms change slowly over time. However, the SNR of the Online-VMD algorithm is much higher than that of Online-EMD, indicating better performance. After a processing time of 30 seconds, the most accurate estimations are achieved by Online-EMD with 6dB SNR of the reconstructed respiration signal and by Online-VMD with a output SNR of 12dB.

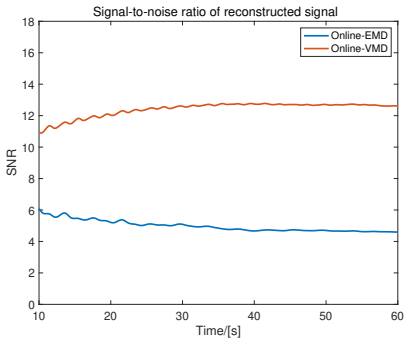

Figure 4.10: SNR of reconstructed signal

As we can see from Fig. 4.11, both curves of estimated frequency error oscillate, but the oscillating amplitude of the Online-VMD curve is greater. Fig. 4.12 describes an example of the relation between extracted and simulated respiration signals. It can be observed that the period of estimated frequency oscillation coincides with the period of the extracted respiration signal. In addition, the simulated respiration frequency is constant in a period, while the waveform of estimated instantaneous frequencies in one extracted respiratory cycle is sinusoidal-like. On this account, RMSE of the estimated frequencies first increases and then decreases in one period, resulting in the resulting in a frequency error that oscillates over time. Furthermore, the envelopes of local maxima in two curves decrease with time, indicating a trend of declining error in estimated frequency over time. It can be seen that the accumulated error of Online-VMD is smaller than Online-EMD when the signal decomposition is completed. The minimal RMSE of Online-EMD is 0.15 and is 0.05 for Online-VMD.

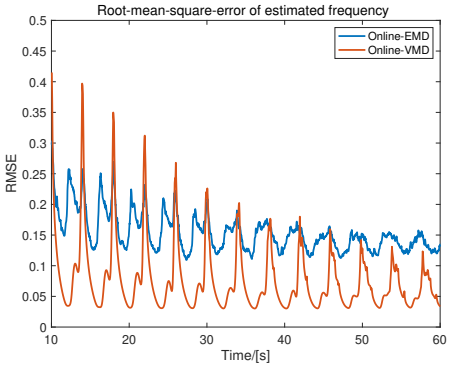

Figure 4.11: RMSE of estimated frequency

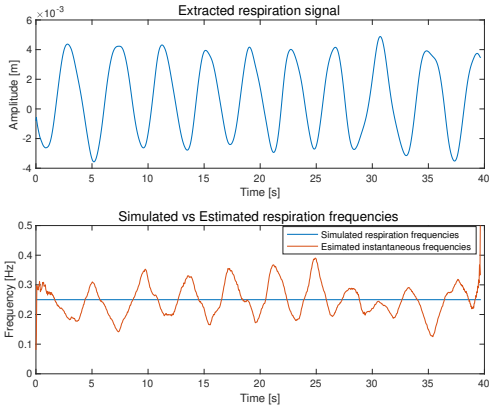

Figure 4.12: Simulated vs Estimated respiration frequencies

4.4. CONCLUSION

This chapter summarized the principle of the online signal decomposition algorithms, and verified the decomposition of the mixed respiration and heartbeat signals through the simulation model. It can be concluded that online methods can achieve the extraction of respiration and heartbeat signals in an environment with noise and auto vibration. Subsequently, the performance of the two online signal decomposition methods was evaluated using repeated simulation experiments by the Monte-Carlo method. From this, we found that the error of the Online-VMD method is smaller and it is more robust to noise and vibration than Online-EMD. The optimal accuracy of estimation over time can be achieved after 30 seconds of processing, the SNR of reconstructed signal is 6dB for Online-EMD and 12dB for Online-VMD, while the RMSE of estimated frequency is 0.15 for Online-EMD and 0.05 for Online-VMD.

5

EXPERIMENTAL VALIDATION

In this chapter, the experimental verification of real data measurements is conducted using two radar systems. Results of signal decomposition methods are demonstrated and compared to illustrate the feasibility of methods in real-world vital signs monitoring.

5.1. MEASUREMENT USING CW RADAR

The first measurement was undertaken by a network analyzer operating at 77GHz as a CW radar, which sampling frequency is 25Hz. The subject under testing was sitting about 1 meter away from the radar as shown in Fig. 5.1. The total measurement time is 60 seconds. In the last few seconds of the measurement, the subject was asked to hold his/her breath so that the radar echo at that time only contains the chest displacement caused by the heartbeat.

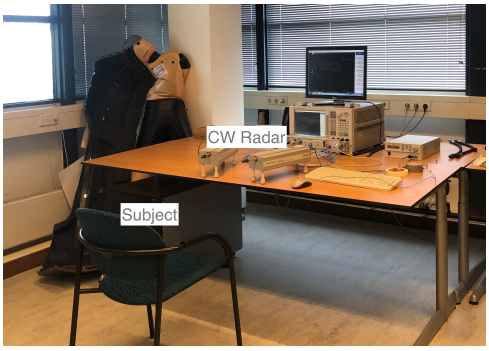

Figure 5.1: CW radar measurement scenario

The measured range history from CW radar is in the top subplot of Fig. 5.2. The range history can be divided into two segments, the first segment contains both respiration and heartbeat information, and the second contains only heartbeat information

(see in Fig. 5.2 bottom). We first use the various signal decomposition algorithms to decompose the mixed echo of respiration and heartbeat and then the echo caused only by the heartbeat. The purpose of this partition is to use the result of heartbeat parameter estimation obtained from two different segments to verify the algorithms. After that, iterative adaptive approach (IAA) is applied as a reference algorithm, estimating respiration and heartbeat frequency to compare with the frequencies obtained by the signal decomposition algorithms.

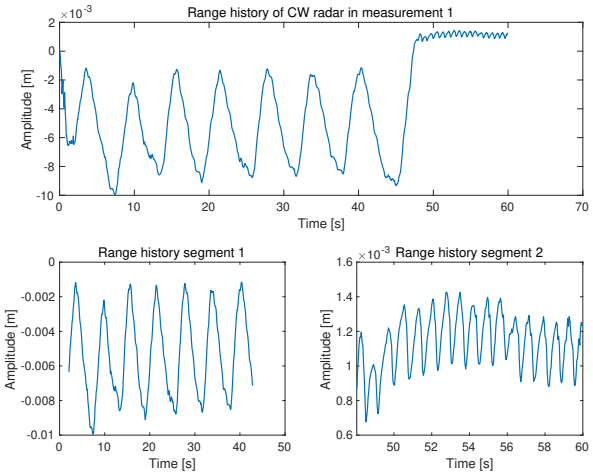

Figure 5.2: The measurement range history from CW radar

5.1.1. SIGNAL DECOMPOSITION METHODS

The results of four kinds of signal decomposition algorithms to two segments of range history are displayed in Fig. 5.3-5.14. The respiration and heartbeat signals can be represented from the decomposition result of the first segment, so we should determine from which two IMFs the respiration and heartbeat signals are located. The second segment only contains the heartbeat information, so we only need to determine the IMF where the heartbeat signal is located. The judgment should be based on the power spectrum and Hilbert spectrum of each IMF. For the IMFs corresponding to the respiration and heartbeat signals, the main lobe in their power spectrum and the instantaneous frequencies in the Hilbert spectrum should be within the typical frequency range of respiration and heartbeat, and the amplitude of IMFs also need to satisfy the requirements for the amplitude of chest displacement induced by respiration heartbeat.

For the first segment of range history decomposition using EMD in Fig. 5.3, the respiration signal component mostly resides in IMF4 and the heartbeat signal component is in IMF2, but part of the respiration signal also residing in IMF3, indicating mode mixing problem; for the second segment decomposition seen in Fig. 5.4, IMF2 represents the original heartbeat signal. Power and Hilbert spectrum of respiration and heartbeat using EMD can be seen in Fig. 5.5. In this figure, it can be seen that the central respiration

and heartbeat frequencies estimated from power spectrum are 0.1639Hz and 1.4375Hz, while the heartbeat frequency obtained from segment 2 is 1.3571Hz. Also, the instantaneous frequencies of vital signs can be acquired in the Hilbert spectrum.

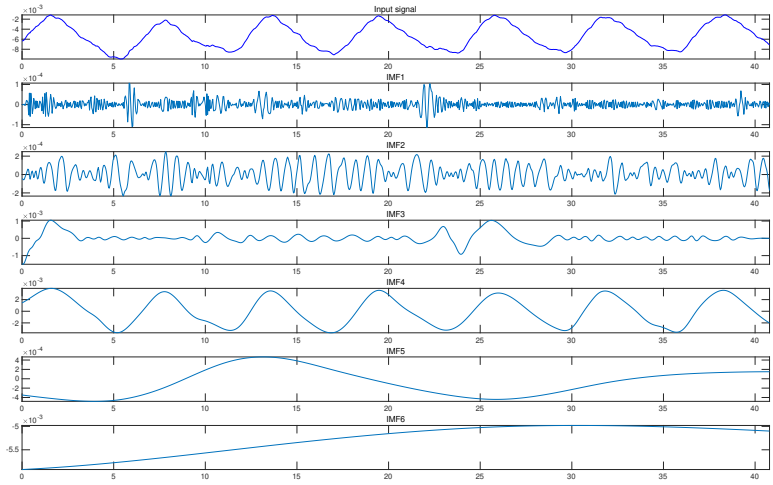

Figure 5.3: Segment 1 decomposition using EMD

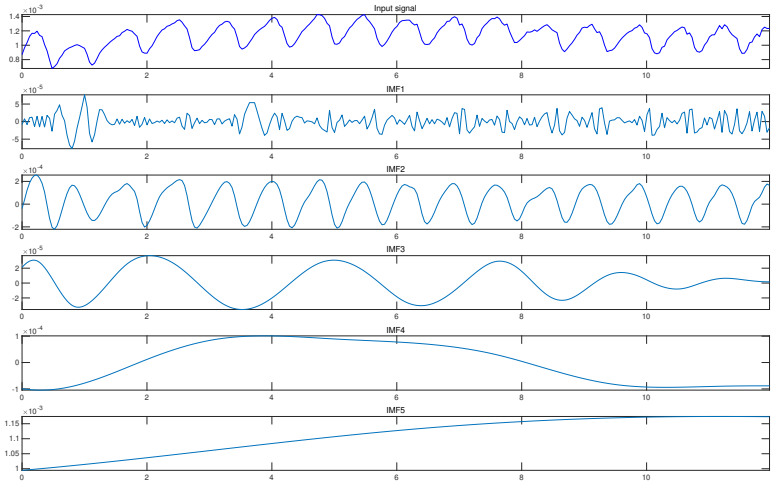

Figure 5.4: Segment 2 decomposition using EMD

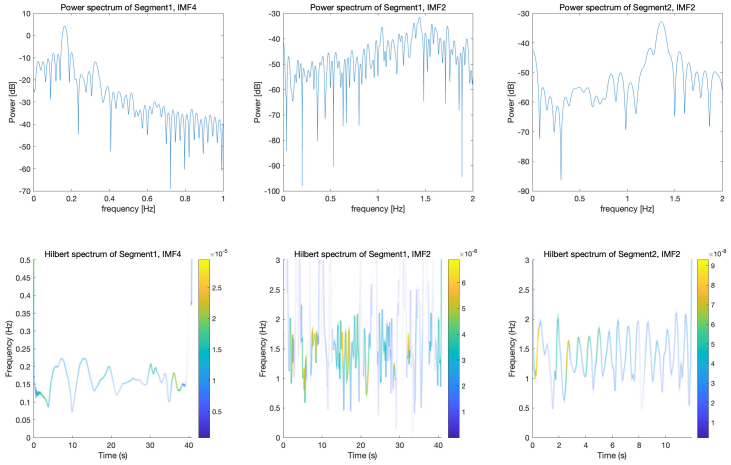

Figure 5.5: Power and Hilbert spectrum of respiration and heartbeat using EMD

To address the mode mixing problem, EEMD is applied and its decomposition result is displayed in Fig. 5.6 and 5.7. In EEMD, more IMFs are decomposed than EMD because of the extra added noise, IMF5 and IMF3 represent respiration and heartbeat signal in segment 1, respectively. And IMF2 in segment 2 decomposition result is the heartbeat signal. Corresponding power and Hilbert spectrum can be seen in Fig. 5.8. The central frequencies of respiration, heartbeat in segment 1 and 2 are 0.1633Hz, 1.4301Hz and 1.3591Hz, respectively.

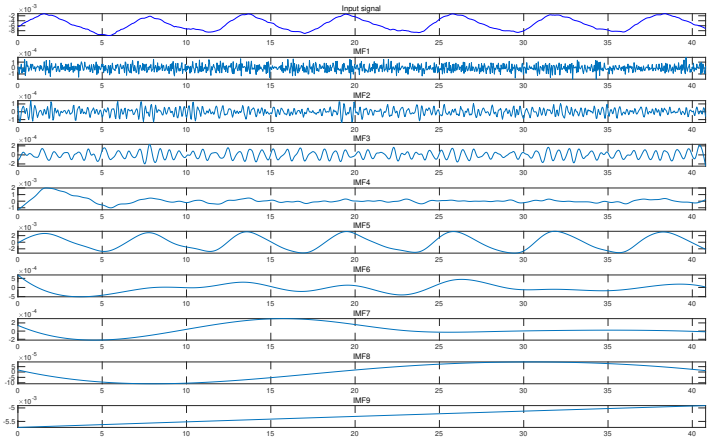

Figure 5.6: Segment 1 decomposition using EEMD

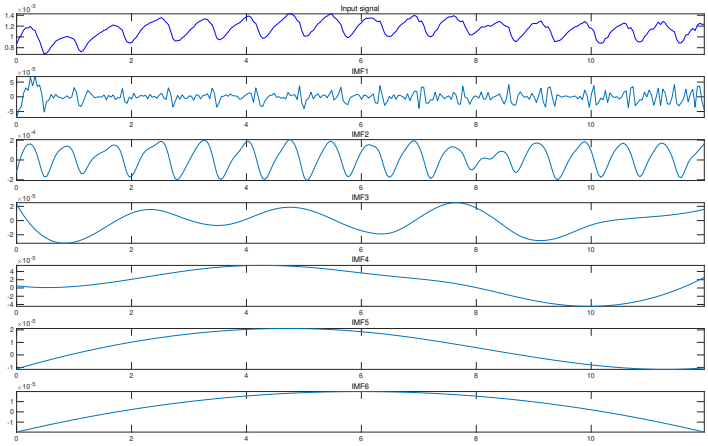

Figure 5.7: Segment 2 decomposition using EEMD

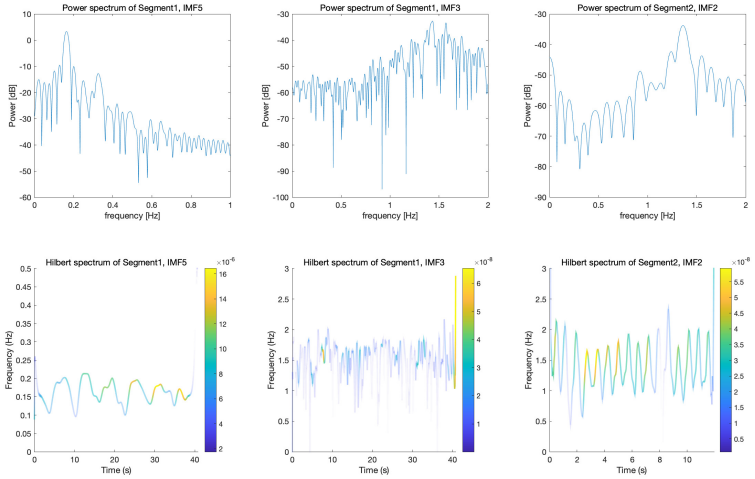

Figure 5.8: Power and Hilbert spectrum of respiration and heartbeat using EEMD

Compared with EEMD, CEEMDAN has reduced number of sifting iterations and lower computational cost, which vital signs decomposition result is in Fig. 5.9 and 5.10. IMF5 and IMF4 denote respiration and heartbeat signals in segment 1, and IMF2 denotes heartbeat signal in segment 2. In Fig. 5.11, the respiration frequency estimated by CEEMDAN is 0.1643Hz while heartbeat frequencies are 1.4332Hz and 1.3574Hz, which shows good agreement, small changes are within normal human behavior.

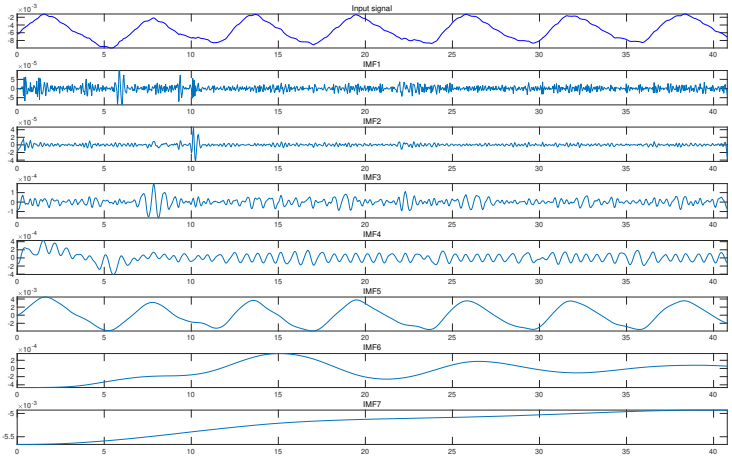

Figure 5.9: Segment 1 decomposition using CEEMDAN

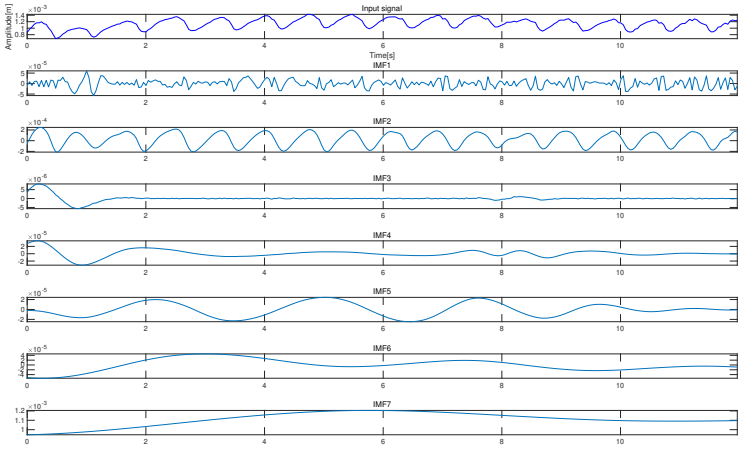

Figure 5.10: Segment 2 decomposition using CEEMDAN

Unlike EMD, VMD first decomposes a sub-signal with the lowest center frequency. Therefore, as a component that is more slowly varying than the heartbeat signal, the respiration signal resides in IMF2 of Fig. 5.12. Heartbeat signal in range history segment 1 is in IMF2 as shown in Fig. 5.12, the second part of the heartbeat signal is represented in IMF2 of Fig. 5.13. The central frequencies of vital signs in VMD are 0.1655Hz, 1.4343Hz and 1.3591Hz. Moreover, the instantaneous frequencies of vital signs obtained by VMD

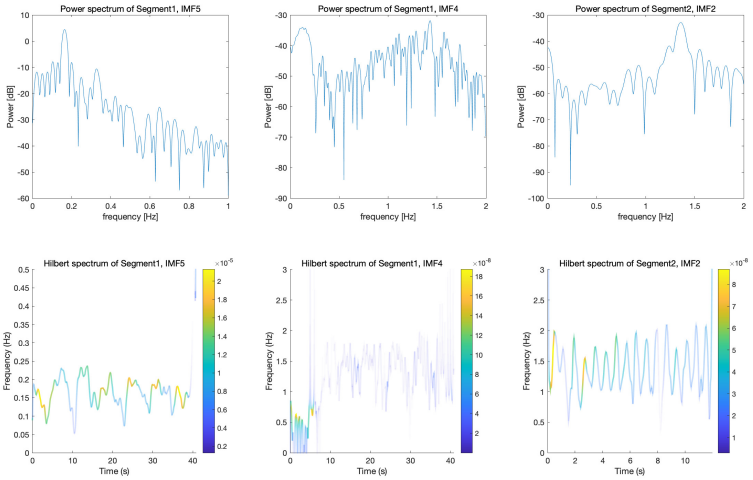

Figure 5.11: Power and Hilbert spectrum of respiration and heartbeat using CEEMDAN

are presented in Fig. 5.14, from which we can see less curve fluctuation in the Hilbert spectrum than other methods, indicating a better signal decomposition and parameter estimation performance.

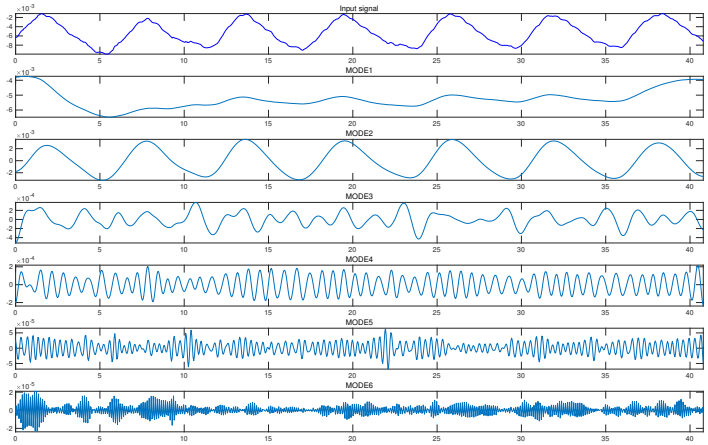

Figure 5.12: Segment 1 decomposition using VMD

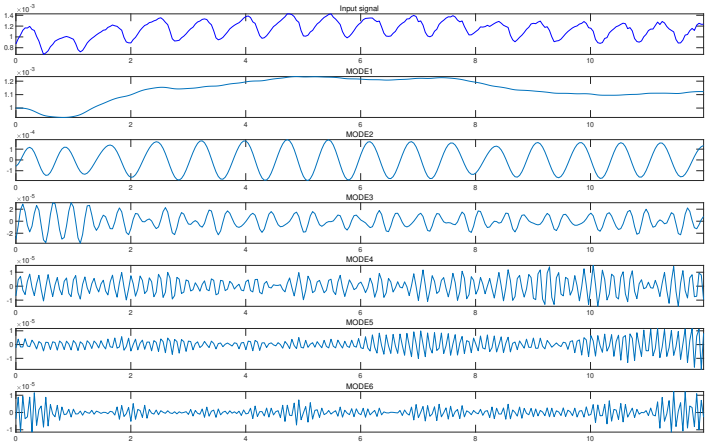

Figure 5.13: Segment 2 decomposition using VMD

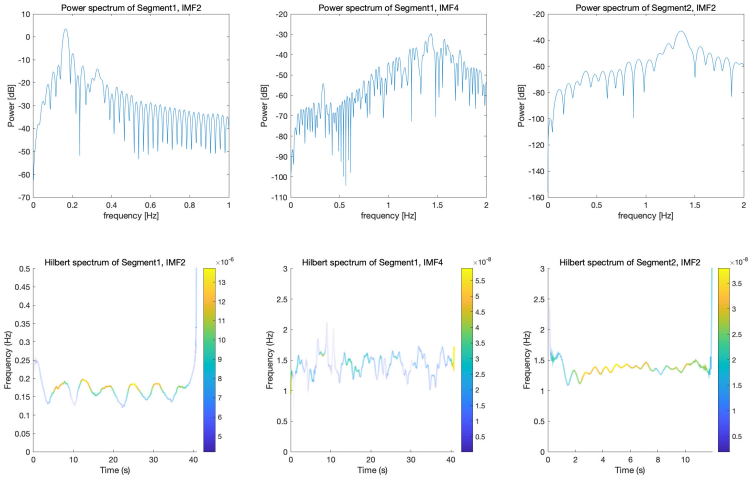

Figure 5.14: Power and Hilbert spectrum of respiration and heartbeat using VMD

5.1.2. ONLINE SIGNAL DECOMPOSITION METHODS

After using classic signal decomposition methods, online EMD and VMD decomposition are performed to estimate the parameters of vital signs dynamically. Contrary to the previous analysis, the whole range history of CW radar is decomposed by online method, instead of being divided into two segments.

Online-EMD is a recursively signal decomposition method, the current IMF is extracted after the previous IMF is completely obtained, which leads to the length of the higher-order IMFs will be gradually shortened. The Online-EMD result of CW radar range history can be seen in Fig. 5.15. The respiration signal component resides in both IMF3 and IMF4, so the online decomposition result is effected by mode mixing, leading to a worse estimation of vital signs frequencies and amplitudes. IMF2 can represent the heartbeat signal within the entire measurement duration. However, IMF2 in the measurement time of segment 1 denotes the heartbeat signal decomposed from mixed respiration and heartbeat signals; IMF2 of segment 2 represents the extracted heartbeat when there is only the presence of a heartbeat signal. The power and Hilbert spectrum of vital signs are displayed in Fig. 5.16. It can be seen from the figure that the estimation performance of the second IMF2 segment is better than that in the first segment. The estimated central frequencies of respiration, heartbeat in segment 1 and 2 are 0.1618Hz, 1.3791Hz and 1.3414Hz, respectively.

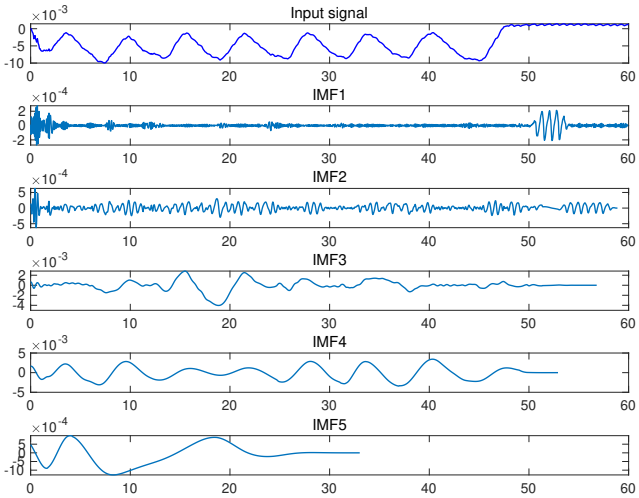

Figure 5.15: Range history decomposition using Online-EMD

Different from Online-EMD, Online-VMD can concurrently decompose all IMFs from the signal in a sliding window. In this case, each IMF in Online-VMD has the same length. In the Online-VMD result as shown in Fig. 5.17, respiration signal extraction is in the first segment of IMF2, the first part of heartbeat signal resides in the first segment of IMF10, while the second part of heartbeat is in the second segment of IMF4. The corresponding

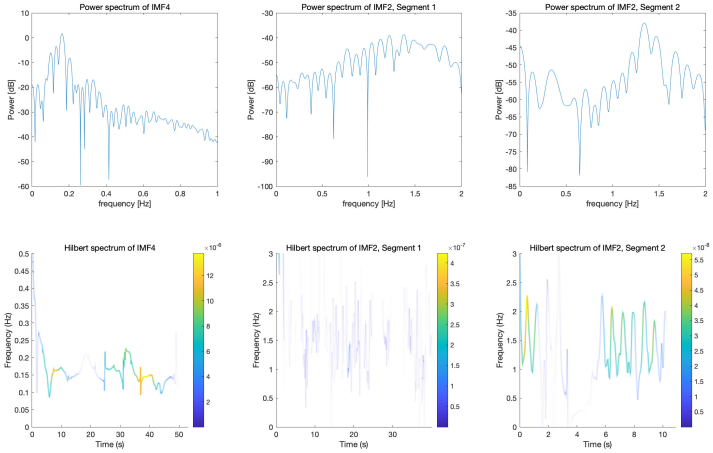

Figure 5.16: Power and Hilbert spectrum of respiration and heartbeat using Online-EMD

power and Hilbert spectrum of respiration and heartbeat signals can be seen in Fig. 5.18. It can be obtained that the central respiration and heartbeat frequencies estimated from power spectrum are 0.1594Hz and 1.4363Hz, whereas the heartbeat frequency obtained from segment 2 is 1.3771Hz. There is no mode mixing issue exists in Online-VMD, and higher-order IMFs in Online-VMD has the same length as the input signal, which means they can contain all the oscillation information of the input signal. Therefore, Online-VMD can be considered as a more promising online signal decomposition method.

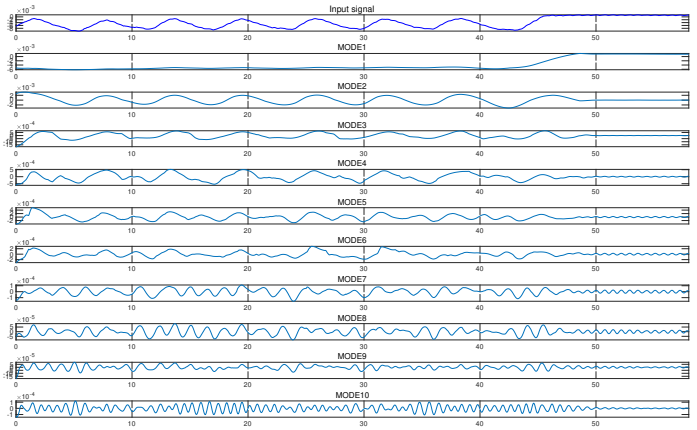

Figure 5.17: Range history decomposition using Online-VMD

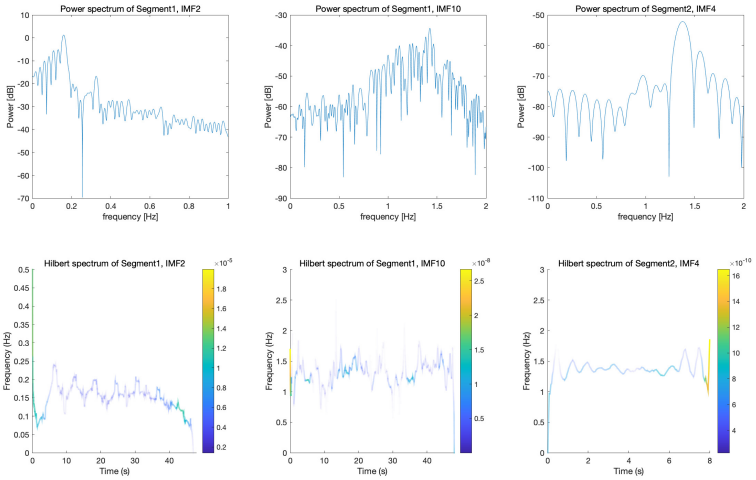

Figure 5.18: Power and Hilbert spectrum of respiration and heartbeat using Online-VMD

5.1.3. COMPARISON

A state of the art frequency estimation method, iterative adaptive approach (IAA), is performed in this thesis to compare with the frequency estimation results of signal decomposition algorithms. In this algorithm, the IAA spectrum is essential to estimate respiration and heartbeat frequency.

Let $\boldsymbol{\mu} = [\mu_1\, \mu_2 \ldots \mu_M]^T$ denotes M measurements of human chest displacement, $\mathbf{a}_M(\omega) = [1\, e^{j\omega} \ldots e^{j(M-1)\omega}]^T$ is the steering vector, the signal matrix can be expressed as:

$$\boldsymbol{\mu} = \mathbf{A}_M \mathbf{x}_K + \mathbf{e}_M, \tag{5.1}$$

where $\mathbf{A}_M = [\mathbf{a}_M(\omega_0)\ \mathbf{a}_M(\omega_1)\ \ldots\ \mathbf{a}_M(\omega_{K-1})]$ with $\omega_k = 2\pi k/K,\ k = 0,1,\ldots,K-1$, and K is selected as $5M$; $\mathbf{x}_K = [x_0\, x_1 \ldots x_{K-1}]^T$ is the complex amplitude associated with frequency ω_k; $\mathbf{e}_M$ is noise vector. The pseudocode of the IAA algorithm is summarized in Algorithm. 3.

Algorithm 3 The Iterative Adaptive Approach Algorithm

Initialization of $\mathbf{p}_K$ using FFT: $\hat{p}_k = \frac{1}{M^2}\left|\mathbf{a}_M^H(\omega_k)\boldsymbol{\mu}\right|^2, k = 0,1,\ldots,K-1$
repeat
  $\mathbf{R}_M = \mathbf{A}_M \mathrm{diag}(\hat{\mathbf{p}}_k)\mathbf{A}_M^H$
  for $k = 0,1,\ldots,K-1$ **do**
    $\hat{x}_k = \frac{\mathbf{a}_M^H(\omega_k)\mathbf{R}_M^{-1}\boldsymbol{\mu})}{\mathbf{a}_M^H(\omega_k)\mathbf{R}_M^{-1}\mathbf{a}_M(\omega_k)}$
    $\hat{p}_k = |\hat{x}_k|^2$
  end for
until convergence

Since the IAA spectrum is obtained, the respiration frequency can be estimated by the location of spectral peak in IAA spectrum $\{\hat{p}_k\}_{k=0}^{K-1}$. Power spectrum and IAA spectrum of the first range history segment are shown in Fig. 5.19. The estimated respiration frequency in power spectrum is $\hat{f}_{r1}$ =0.1670Hz, while estimated respiration frequency in IAA spectrum is $\hat{f}_{r2}$ =0.1667Hz. Other dominant peaks shown in the IAA spectrum indicate the harmonics of respiration, or the heartbeat frequency. Respiration harmonics should be removed to eliminate the influence on heartbeat frequency estimation.

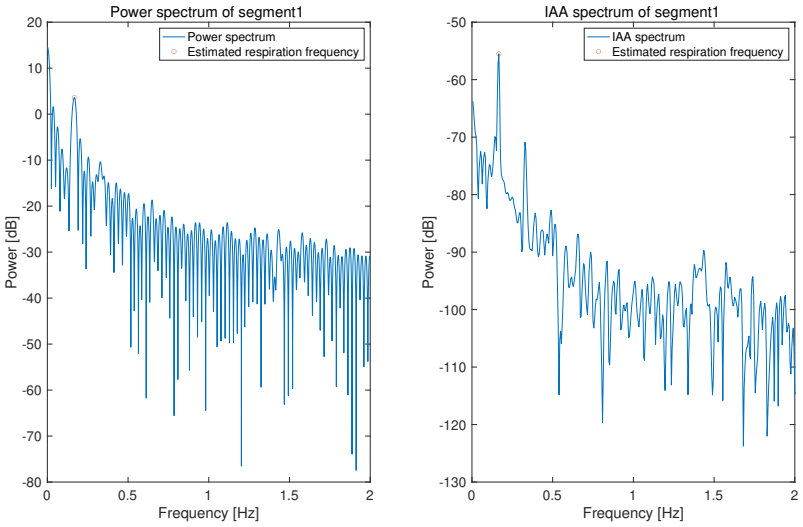

Figure 5.19: Power and IAA spectrum of Segment 1

The harmonics of the respiration signal may interfere with the heartbeat signal. Typical heartbeat frequency is between 0.8 and 2 Hz, so the first 12 respiration harmonics are removed to better expose the heartbeat signal [30]. The complex amplitude of the kth respiration harmonic $\hat{\beta}_k, k = 1,2,\ldots,12$ is obtained in IAA algorithm:

$$\hat{\beta}_k = \frac{\mathbf{a}_M^H(\omega_{r,k})\mathbf{R}_M^{-1}\boldsymbol{\mu}}{\mathbf{a}_M^H(\omega_{r,k})\mathbf{R}_M^{-1}\mathbf{a}_M(\omega_{r,k})}. \tag{5.2}$$

The estimate of the heartbeat signal $\hat{\boldsymbol{\mu}}_h$ after respiration harmonic removal:

$$\hat{\boldsymbol{\mu}}_h = \boldsymbol{\mu} - 2\sum_{k=1}^{12} \mathrm{Re}\left[\hat{\beta}_k \mathbf{a}_M(2\pi k \hat{f}_r)\right]. \tag{5.3}$$

The IAA spectrum after respiration harmonic cancellation is in Fig. 5.20. Then, the heartbeat frequency can be easily determined from the location of the dominant peak of the IAA spectrum of $\hat{\boldsymbol{\mu}}_h$ between 0.8 Hz and 2 Hz, the estimated heartbeat frequency $\hat{f}_{h1}$ = 1.4363Hz. Iterative adaptive approach is also applied to range history segment

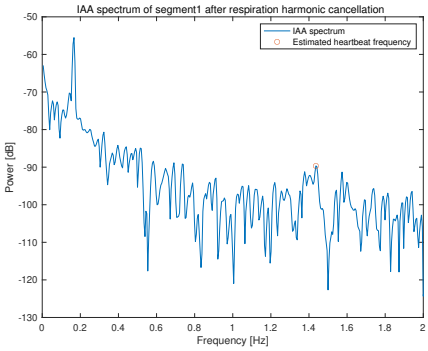

Figure 5.20: IAA spectrum for heartbeat estimation

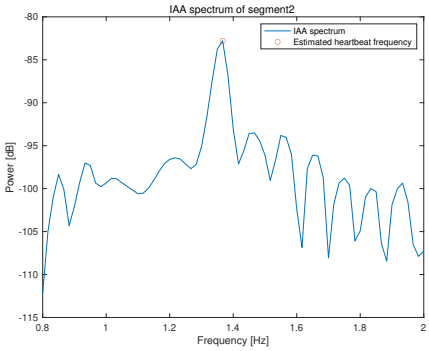

Figure 5.21: IAA spectrum of Segment 2

two to estimate the heartbeat frequency. IAA spectrum of segment 2 is in Fig. 5.21. The estimated heartbeat frequency is $\hat{f}_{h2} = 1.3667$Hz.

The vital signs central frequency estimation results using signal decomposition methods and iterative adaptive approach are displayed in Tab. 5.1. The table below illustrates that the heartbeat frequency estimation results gained from two segments of radar data have a good consistency, and the decomposition results agree well with IAA estimation. Hence, proof of the signal decomposition methods in vital signs monitoring is provided.

Method	Respiration frequency [Hz]	Heartbeat frequency 1 [Hz]	Heartbeat frequency 2 [Hz]
EMD	0.1639	1.4375	1.3571
EEMD	0.1633	1.4301	1.3591
CEEMDAN	0.1643	1.4332	1.3574
VMD	0.1655	1.4343	1.3591
Online-EMD	0.1618	1.3791	1.3414
Online-VMD	0.1624	1.4271	1.3771
IAA	0.1667	1.4363	1.3667

* Heartbeat frequency 1 denotes the estimated heartbeat frequency from segment 1
** Heartbeat frequency 2 denotes the estimated heartbeat frequency from segment 2

Table 5.1: Comparison of estimated respiration and heartbeat frequency using different methods

5.2. MEASUREMENT USING TWO RADARS

In the second measurement, we used a 77GHz CW radar and a 24GHz FMCW radar (with 1GHz bandwidth and 6Hz sampling in slow time) to monitor vital signs simultaneously, as shown in Fig. 5.22. The range resolution of FMCW radar is not small enough to extract vital signs from range displacement, so it is Doppler information that utilized to obtain range history. The minimal detectable movement of the chest in FMCW radar

system is the displacement induced by heartbeat with an amplitude of 0.37mm, while it is 0.11mm for CW radar. The two radars did not face the subject under testing directly in this measurement so the detected vital signs are weaker than those in measurement 1. Only the respiration signal can be extracted in this measurement and we will compare the vital signs monitoring results of the two radars in this section. The range histories of FMCW and CW radar are displayed in Fig. 5.23 and 5.24, respectively. The objective of this measurement is to investigate the performance and accuracy of different signal decomposition methods applied to vital signs monitoring in CW and FMCW radar systems.

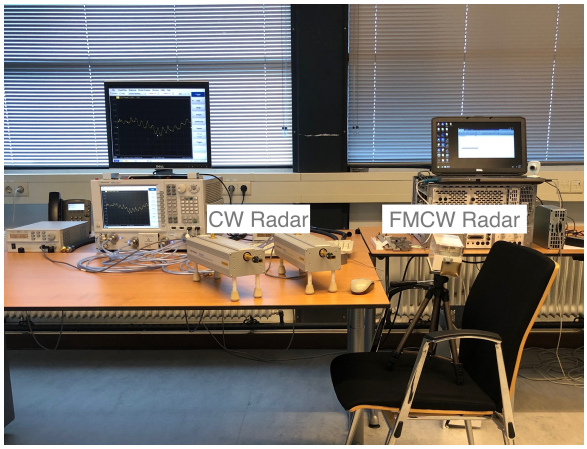

Figure 5.22: Two radars measurement setup

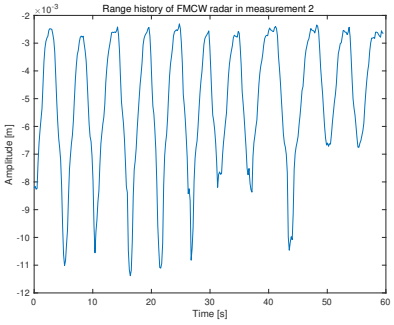

Figure 5.23: Range history of FMCW radar

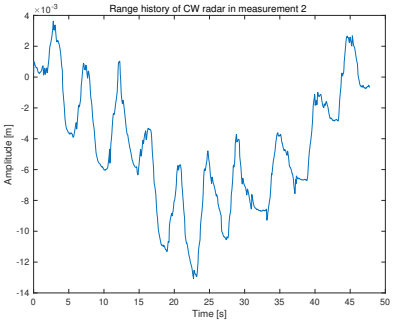

Figure 5.24: Range history of CW radar

5.2.1. SIGNAL DECOMPOSITION METHODS

Four signal decomposition methods are applied to the range history of two radars. When implementing EMD, respiratory mode mixing appears in IMF2-3 in FMCW signal decomposition result as shown in Fig. 5.25, and in IMF3-5 in FMCW signal decomposition

result as shown in Fig. 5.26. IMF2 in FMCW signal decomposition and IMF4 in CW signal decomposition can be considered as respiration signals. However, the mode mixing problem leads to mistakes of instantaneous frequency estimation in Hilbert spectrum (see Fig. 5.27 and 5.28). From the power spectrum, the central frequencies of respiration in FMCW and CW are estimated as 0.1838Hz and 0.2144Hz, respectively.

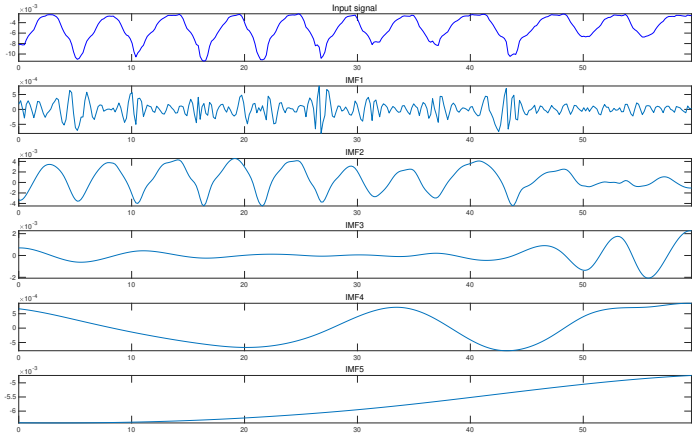

Figure 5.25: Range history decomposition of FMCW radar using EMD

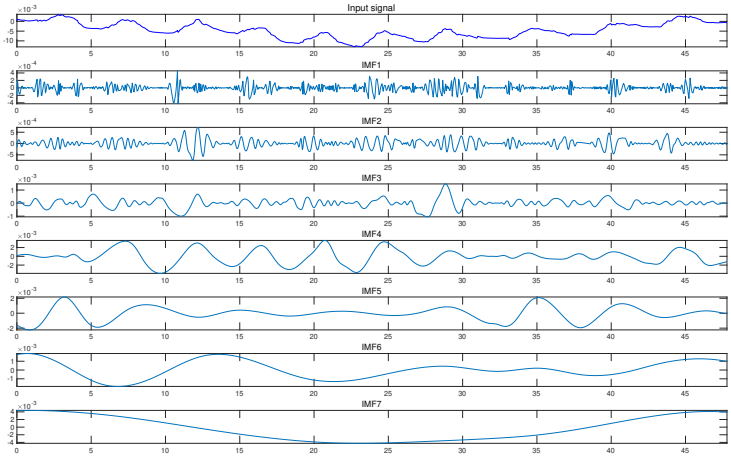

Figure 5.26: Range history decomposition of CW radar using EMD

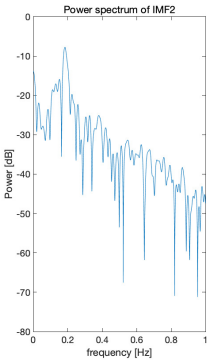

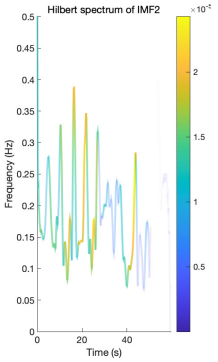

Figure 5.27: Power and Hilbert spectrum of respiration in FMCW radar using EMD

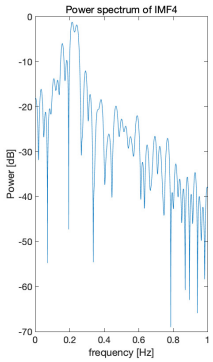

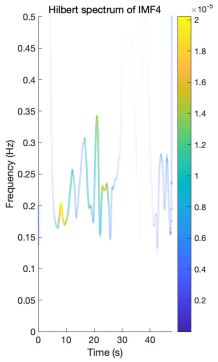

Figure 5.28: Power and Hilbert spectrum of respiration in CW radar using EMD

5

In Fig. 5.29 and 5.30, the mode mixing of respiration signal is mostly tackled in EEMD. The power and Hilbert spectrum of IMF3 of FMCW radar is depicted in Fig. 5.31 and spectrum of IMF5 of CW radar is in Fig. 5.32. We can see the time-frequency distribution of extracted respiration signals in EEMD are more realistic than that in EMD. The central frequencies of respiration of two radars obtained by EEMD are 0.1904Hz (for FMCW radar) and 0.2145Hz (for CW radar).

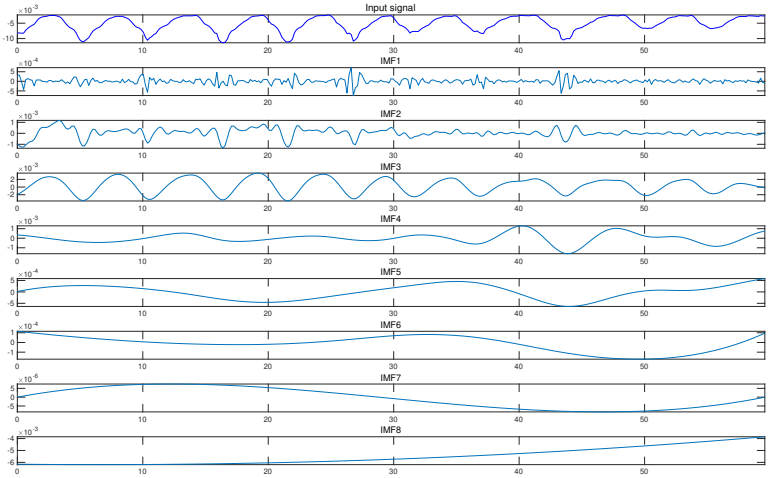

Figure 5.29: Range history decomposition of FMCW radar using EEMD

The third signal decomposition method we use is CEEMDAN, and the results are shown in Fig. 5.33 and 5.34. Power and Hilbert spectrum of IMF3 in Fig. 5.33 is described

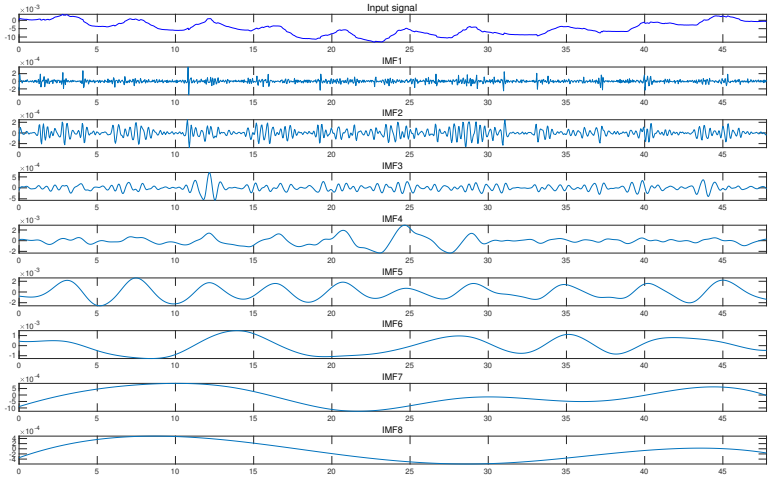

Figure 5.30: Range history decomposition of CW radar using EEMD

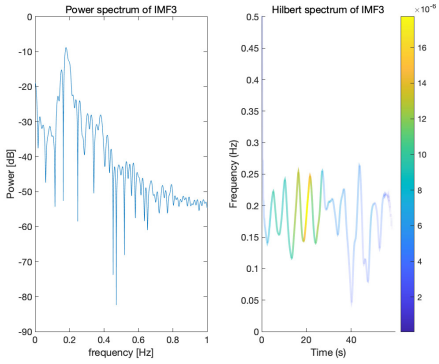

Figure 5.31: Power and Hilbert spectrum of respiration in FMCW radar using EEMD

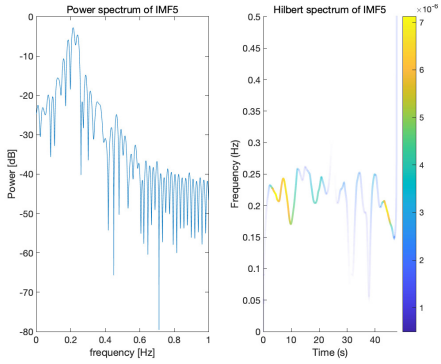

Figure 5.32: Power and Hilbert spectrum of respiration in CW radar using EEMD

in Fig. 5.35, while spectrum of IMF5 in CW radar range history decomposition result can be seen in Fig. 5.36. The instantaneous frequency of extracted respiration from CW radar changes more dramatically than the signal from FMCW radar. And the peak of power spectrum in FMCW radar is located at 0.1785Hz, the frequency peak in CW radar is 0.2154Hz.

VMD shows good performance of signal decomposition in measurement 1. In this measurement, we also applied VMD, and the range history decomposition results of FMCW and CW radar is shown in Fig. 5.37 and 5.38. Respiration signals in the two radars both reside in IMF2. The spectrum of extracted respiration signals are in Fig. 5.39 and

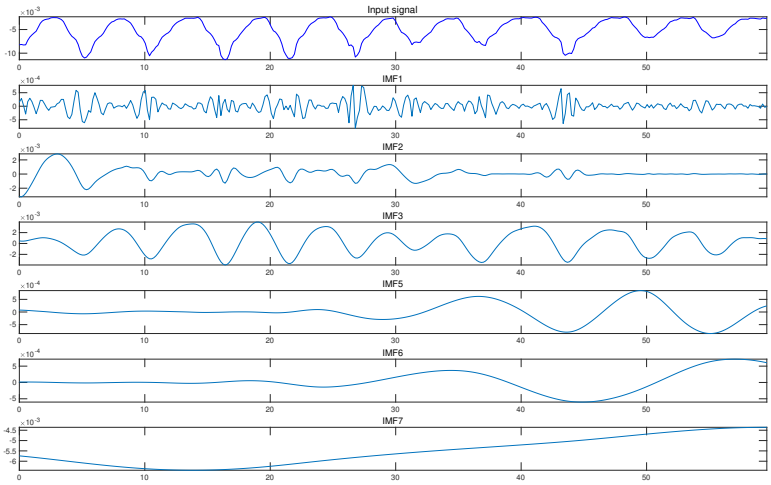

Figure 5.33: Range history decomposition of CW radar using CEEMDAN

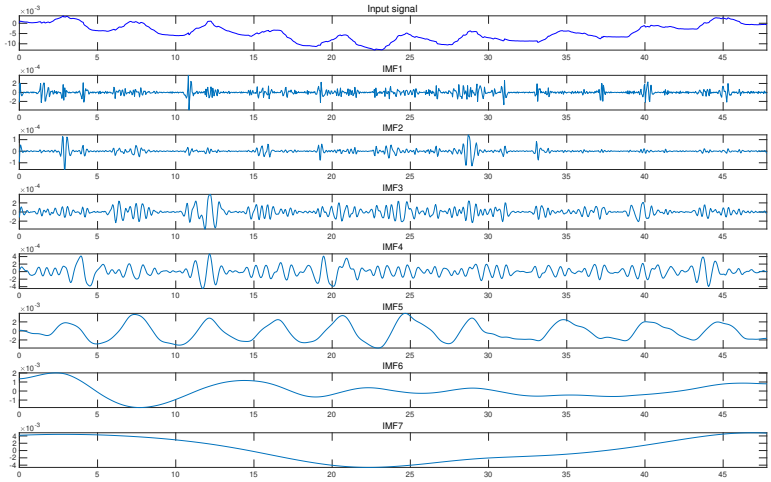

Figure 5.34: Range history decomposition of CW radar using CEEMDAN

5.40. The central frequencies of FMCW and CW radar are 0.1808Hz and 0.2155Hz. In this measurement, VMD still maintains a good signal decomposition effect.

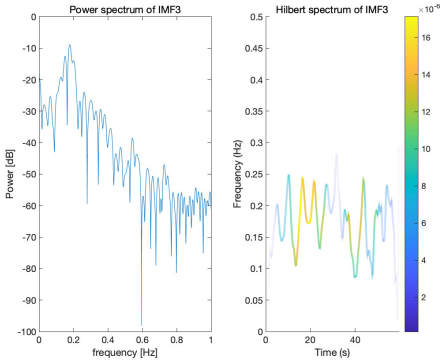

Figure 5.35: Power and Hilbert spectrum of respiration in FMCW radar using CEEMDAN

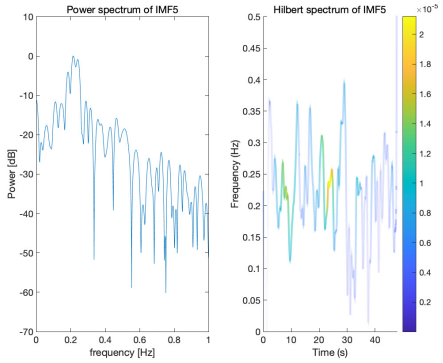

Figure 5.36: Power and Hilbert spectrum of respiration in CW radar using CEEMDAN

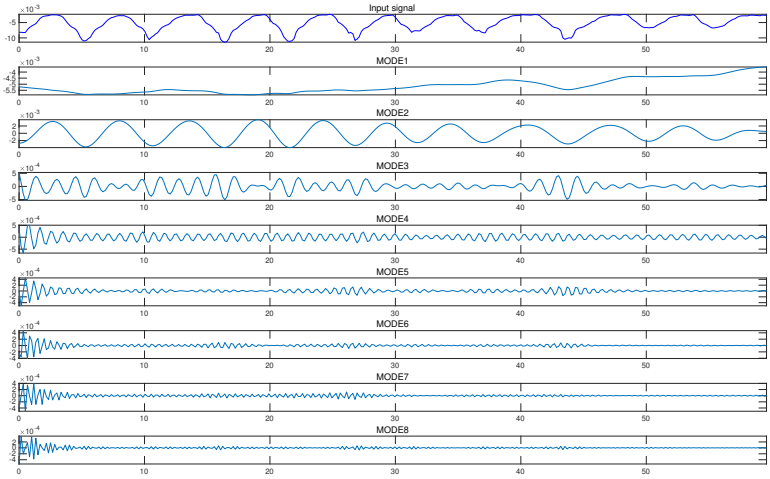

Figure 5.37: Range history decomposition of FMCW radar using VMD

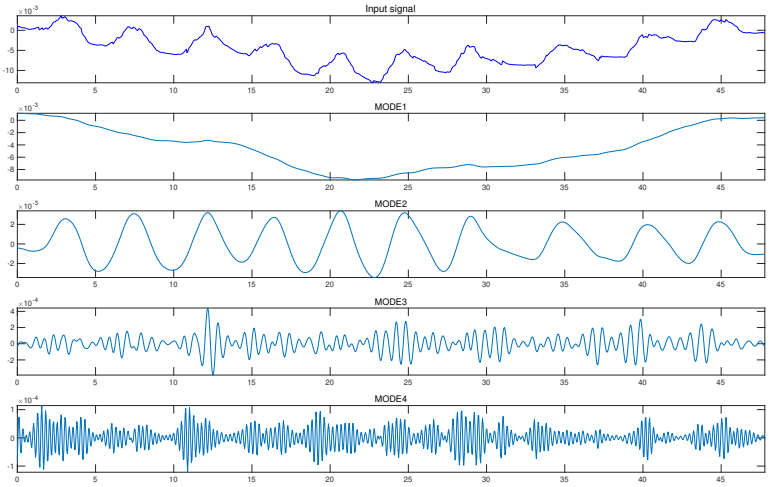

Figure 5.38: Range history decomposition of CW radar using VMD

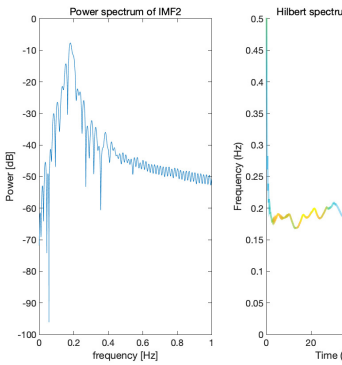

Figure 5.39: Power and Hilbert spectrum of respiration in FMCW radar using VMD

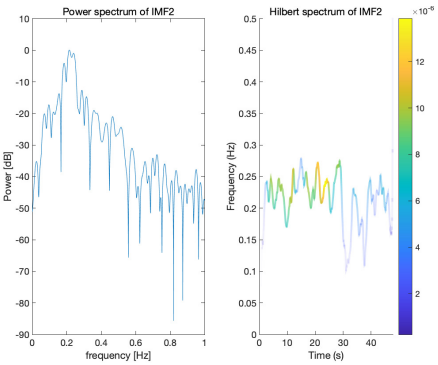

Figure 5.40: Power and Hilbert spectrum of respiration in CW radar using VMD

5.2.2. ONLINE SIGNAL DECOMPOSITION METHODS

After implementing classic signal decomposition methods, Online-EMD and Online-VMD are performed in measurement 2. Online-EMD results are shown in Fig. 5.41, 5.42. It is easy to tell that IMF2 in Fig. 5.41 can represent the input respiration signal, while IMF4, i.e., the residue signal in Fig. 5.42 represents the respiration signal in CW radar. The corresponding power and Hilbert spectrum of respiration signals can be seen in Fig. 5.43, 5.44. The estimated respiration frequency of FMCW radar is 0.1832Hz and frequency of CW radar is 0.2265Hz.

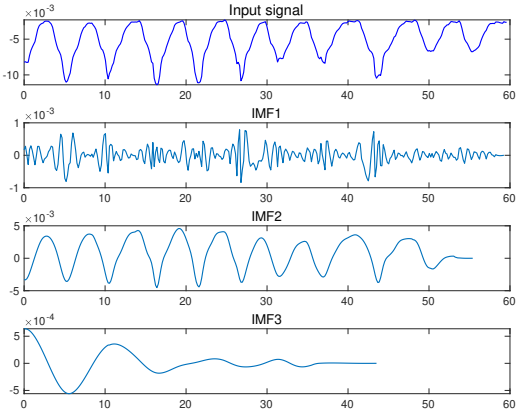

Figure 5.41: Range history decomposition of FMCW radar using Online-EMD

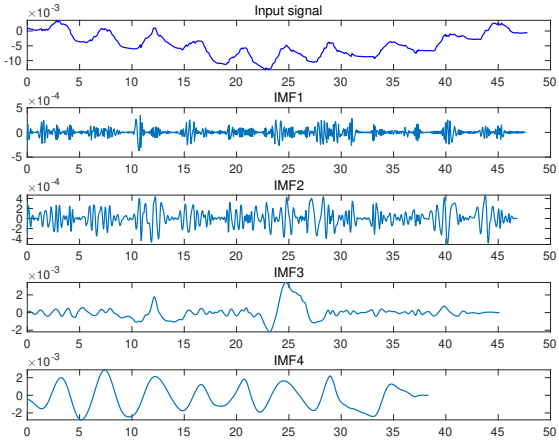

Figure 5.42: Range history decomposition of CW radar using Online-EMD

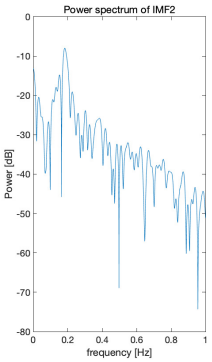

Figure 5.43: Power and Hilbert spectrum of respiration in FMCW radar using Online-EMD

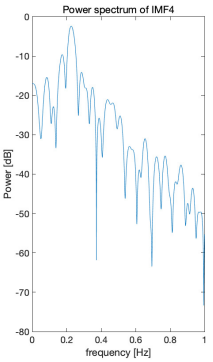

Figure 5.44: Power and Hilbert spectrum of respiration in CW radar using Online-EMD

5

The Online-VMD results of two radar signals dynamic decomposition are shown in Fig. 5.45 and 5.46. Similar to classic VMD, IMF2 in Online-VMD also represents respiration signal. The central and instantaneous frequencies of respiration signals from two radars can be seen in Fig. 5.47 and 5.48. The central frequencies of respiration signals in two radars are estimated as 0.1799Hz and 0.2161Hz.

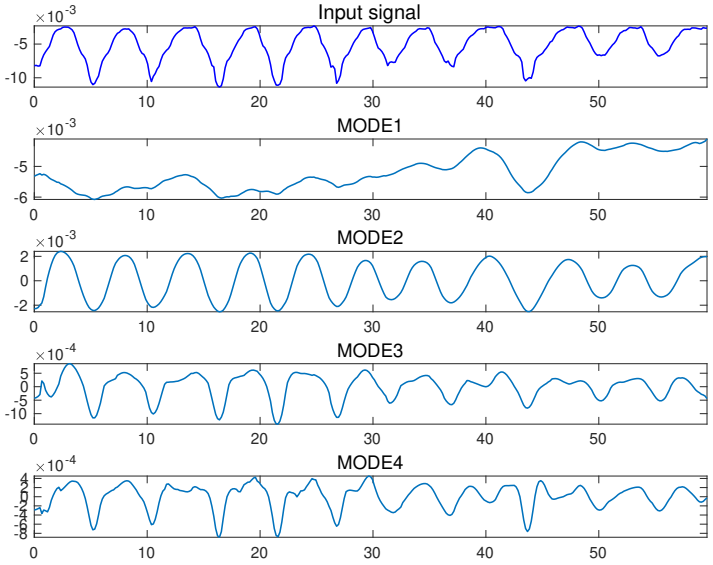

Figure 5.45: Range history decomposition of FMCW radar using Online-VMD

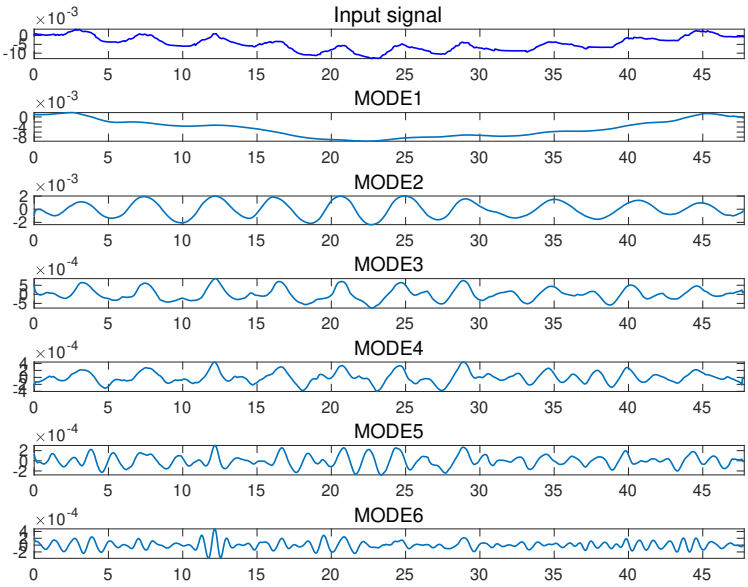

Figure 5.46: Range history decomposition of CW radar using Online-VMD

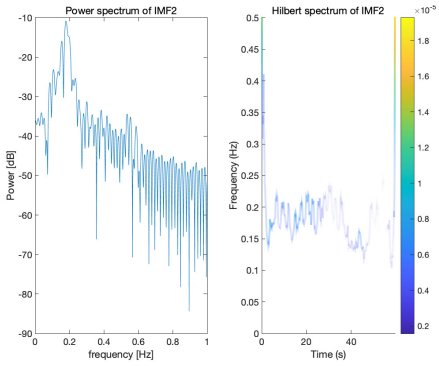

Figure 5.47: Power and Hilbert spectrum of respiration in FMCW radar using Online-VMD

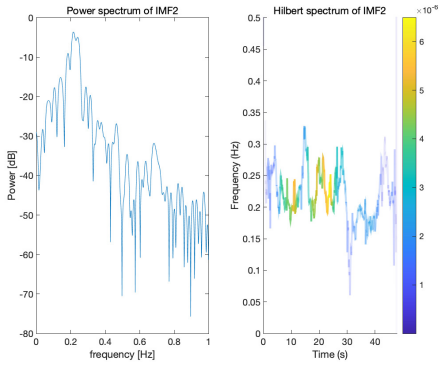

Figure 5.48: Power and Hilbert spectrum of respiration in CW radar using Online-VMD

The processing abilities of online signal decomposition methods are reflected by two parameters: the minimal monitoring time $t_{o,min}$ that can get the vital signs information of the auto driver; and the reaction time of algorithm t_r when the driver's behavior changes to an abnormal state. The outcome of Online-EMD/VMD with different window size in two radar systems are shown in Tab. 5.2.

Method	FMCW radar system			CW radar system		
	Window size	$t_{o,min}[s]$	$t_r[s]$	Window size	$t_{o,min}[s]$	$t_r[s]$
Online-EMD	7 extrema	25.6	2.81	7 extrema	19.9	14.45
Online-VMD	30 points	5.5	0.036	100 points	4.7	1.04

Table 5.2: Minimal monitoring time and reaction time of online decomposition methods

From the table, it can be observed that Online-VMD is faster than Online-EMD in both aspects of minimal monitoring time and reaction time. CW radar system used in this measurement operates at a higher frequency band and has a higher sampling frequency than FMCW radar system, resulting in a better velocity resolution and a larger number of extrema in range history. Therefore, there is a longer reaction time of vital signs monitoring using Online-EMD in CW system. Besides, the smaller window size applied for Online-VMD in FMCW radar provides a lower computational cost of the weighting procedure, which reduces the reaction time than CW radar.

5.2.3. COMPARISON

In this measurement, IAA is also implemented to compare with the central frequency estimation results obtained from signal decomposition methods. IAA spectrum of range history in FMCW radar is depicted in Fig. 5.49, the estimated respiration frequency is 0.1807Hz. And IAA spectrum of CW radar signal is in Fig. 5.50, the estimated respiration frequency is 0.2134Hz.

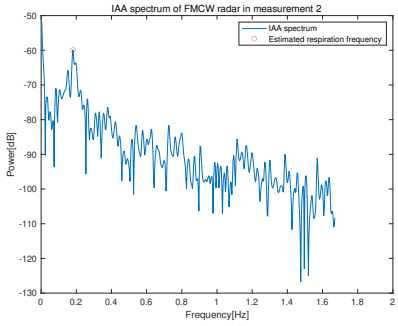

Figure 5.49: IAA spectrum of FMCW radar signal

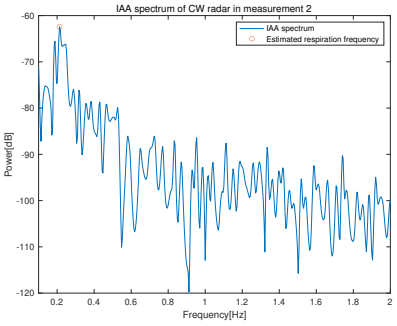

Figure 5.50: IAA spectrum of CW radar signal

No other reliable vital signs monitoring device was used in the experimental measurement as the ground truth data. IAA, as a robust, high resolution and low sidelobe method, can accurately estimate the respiration frequency from radar echo. Hence, IAA is used as the reference method to evaluate the accuracy of other methods. The comparison of respiration frequency estimation results of two radars in measurement 2 using different signal decomposition methods and iterative adaptive approach are displayed in Tab. 5.3.

Method	FMCW radar system		CW radar system		$\frac{f_{r2}}{f_{r1}}$
	Frequency f_{r1} [Hz]	Accuracy	Frequency f_{r2} [Hz]	Accuracy	
EMD	0.1838	98.28%	0.2144	99.53%	1.17
EEMD	0.1803	99.72%	0.2145	99.49%	1.19
CEEMDAN	0.1785	98.78%	0.2154	99.06%	1.20
VMD	0.1808	99.94%	0.2155	99.02%	1.20
Online-EMD	0.1832	98.62%	0.2265	93.91%	1.23
Online-VMD	0.1799	99.56%	0.2161	98.74%	1.20
IAA	0.1807	-	0.2134	-	1.18

Table 5.3: Estimated respiration frequency using different radars and methods

In general, the estimated respiration frequencies from two radar types should have similar results due to the simultaneity of measurement. However, it can be seen from the table above that the frequency of the respiration estimated from the CW radar signal is always about 1.2 times the respiration frequency obtained from the FMCW radar signal, no matter which method is used. For this result, we guessed that there might be an error in the time axis of one of the radars, making the estimated respiration signal frequency from that radar echo to be inconsistent with the actual frequency. To verify the guess, we checked another set of radar data that measured human chest displacement at the same time by FMCW and CW radars. The range histories of two radars in this measurement are shown in Fig. 5.51 and 5.52. From the figures, we can see the data length of FMCW radar is about 72 seconds according to data logs, while recorded CW radar data is only 60 seconds (set by radar settings and checked with timer during the experiment). However, the data of the two radars should have the same length in reality because the measurement started and ended at the same time. Therefore, the difference in the measured data length of the FMCW and CW radars proves the difference in the respiration frequency estimated from the two radars obtained above.

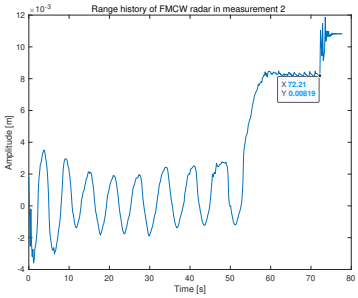

Figure 5.51: Range history of FMCW radar

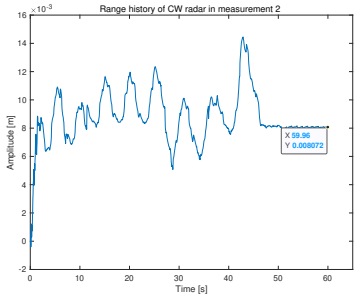

Figure 5.52: Range history of CW radar

From Tab. 5.3, assessment results seem to suggest that apart from Online-EMD in CW radar, other signal decomposition methods have high accuracy in respiration fre-

quency estimation when IAA is applied as the reference method. For offline frequency estimation, VMD provides the highest accuracy as 99.94% in FMCW radar system; EMD obtains the closest center frequency estimation result to IAA when processing the CW radar data, with an accuracy of 99.53%. As for dynamic frequency estimation methods, Online-VMD performs better than Online-EMD in both FMCW and CW radar systems, with accuracy of 99.56% and 98.74%, respectively. More information on instantaneous frequency estimation would help to establish a better accuracy evaluation on this matter. In this measurement, we assume that the person under testing was breathing uniformly because of the short measurement time. Consequently, the accuracy of signal decomposition methods in FMCW and CW radar systems can also be evaluated by the variance of estimated instantaneous frequencies obtain by HHT. The mean value and variance of the estimation in different methods and systems is compared in Tab. 5.4.

Method	FMCW radar system		CW radar system	
	Mean [Hz]	Variance	Mean [Hz]	Variance
EMD	0.1742	0.0213	0.2707	0.0977
EEMD	0.1913	0.00417	0.2084	0.00559
CEEMDAN	0.1744	0.00678	0.2076	0.0142
VMD	0.1922	0.00137	0.2076	0.00719
Online-EMD	0.1874	0.00694	0.2587	0.0392
Online-VMD	0.1830	0.00181	0.2073	0.00939

Table 5.4: Accuracy evaluation of different methods and radar systems

It can be obtained from the table that VMD method has the minimal variance, providing the most stable and accurate estimate in FMCW system. VMD applied in FMCW radar improves the variance of respiration frequency estimation by a factor of 15.6 compared to EMD and by factor of 3-5 compared to EEMD and CEEMDAN. However, the variance of VMD in CW system is 1.3 times higher than EEMD, so EEMD in CW radar system is preferable to VMD. Truth has been confirmed that Online-VMD in both systems shows good performance in dynamic vital signs estimation, which enhance the performance than Online-EMD by a factor of 4. Moreover, the accuracy assessment result of each method in FMCW radar system is superior to CW system, certifying that FMCW radar with lower central frequency is a more appropriate option for vital signs monitoring.

5.3. CONCLUSION

In this chapter, we first describe the experiment of vital signs monitoring using CW radar. The range history of CW was divided into two segments, the first one consists of respiration and heartbeat signal information, and the second segment contains only heartbeat information. It is found that the respiration and heartbeat signals can be extracted from the first segment, and the obtained frequency of the heartbeat signal is similar to the heartbeat frequency estimated in the second segment, which verifies the feasibility of the signal decomposition methods in vital signs monitoring. This experiment con-

firmed that the frequencies of respiration and heartbeat can be reliably determined by signal decomposition methods in a CW radar system which illuminates the human chest directly.

The second experiment was conducted by a FMCW and a CW radar, CW radar has a higher accuracy with a minimal detectable movement of human chest as 0.11mm, lower than the movement of 0.37mm in FMCW radar system. The two radars simultaneously measured the movement of the subject's chest. But only the respiration signal can be extracted from the radar echo since neither of the radars is directly facing the subject. Then we estimate the frequency of the respiration signals obtained from the two radars and found that there is always a 1.2 times frequency difference. From this result, we infer that there is an error in one of the radar time axis. Experiments have proved that the signal decomposition methods are effective in vital signs monitoring, in which VMD presents robustness to noise and good performance in both the decomposition of the entire signal or the dynamic decomposition of the input signal. Minimal monitoring time is 5.5s and reaction time is as low as 0.036s when applying Online-VMD in FMCW radar system. It is confirmed that Online-VMD which has an accuracy of 99.56% and a variance of estimated frequencies of 1.81×10^{-3} is the preferable method and FMCW radar system is more suitable for real-time vital signs monitoring.

6

CONCLUSION AND FUTURE WORK

6.1. CONCLUSION

This thesis was undertaken to explore and evaluate signal decomposition algorithms for radar-based automobile driver vital signs monitoring. The cardiopulmonary physiology activities of the human body are revised and appropriate models for vital signs monitoring with radar were established. Assume that the distance between automobile driver and radar is constant during the monitoring process, vital signs information is presented in the radar range history, which can be accurately extracted from the measured phase of the signal (in CW, FMCW radar systems), or range displacement (in IR-UWB radar system). Then three empirical and one variational signal decomposition methods were employed for separate estimation of respiration and heartbeat frequencies from the extracted range history of the radar echo, demonstrating the feasibility of these methods for vital signs extraction. Moreover, two online signal decomposition approaches are performed to achieve dynamic estimations of vital signs and detect abnormal human behavior.

Main contributions of this thesis are described as follows:

1. Models composed of human chest movement, environmental noise and automatic vibration in different radar systems for vital signs monitoring were established. Human chest movement is usually modeled as a sinusoidal displacement, and we used improved cardiopulmonary models to better fit into the actual chest displacement induced by respiration and heartbeat. After that, a first-order auto-regression model was proposed to simulate the fluctuation of both respiration and heartbeat signals in reality. A novel model of vibration was established as a second-order auto-regressive model with a spectral peak around 1Hz.

2. Signal decomposition algorithms were applied to extract vital signs and extended to dynamic decomposition cases. EMD is the most well-known signal processing in this analysis, but it suffers from the mode mixing problem. To address the issue, two modifications, EEMD and CEEMDAN, were also investigated. Besides,

we employed VMD to improve the stability of EMD and its modifications against noise. Furthermore, online decomposition methods were utilized to dynamically extract vital signs. For the first time, Online-VMD method has been developed and applied to the decomposition of vital signs. Afterward, their performances were assessed and compared by Monte Carlo simulations. It is found that VMD is the most promising method in vital signs monitoring due to its robustness to noise and vibration.

3. Hilbert-Huang transform (HHT) is a time-frequency analysis method used in conjunction with signal decomposition algorithms. In this thesis, HHT was introduced to analyze the extracted IMFs by signal decomposition methods. By applying this, the modes corresponding to respiration and heartbeat signals are determined, and their instantaneous frequencies and amplitudes are obtained.

4. For the first time, signal decomposition methods in vital signs monitoring have been conducted and evaluated by two different radar sensors working in different frequency bands, proving the practicality of vital signs monitoring of the car driver by means of CW and FMCW radar systems. CW radar with a higher central frequency has a smaller minimal detectable movement of human chest of 0.11mm, while the minimum chest displacement can be detected in FMCW radar is 0.37mm. Range histories recovered by the phase shift of radar echo were obtained and employed in both systems for vital signs extraction.

5. From the experimental results, robustness of signal decomposition algorithms to noise and measurement artifacts were demonstrated. Two novel parameters, minimal monitoring time and reaction time, were proposed to describe the outcome of online signal decomposition methods with certain sliding window sizes. Online-VMD has been confirmed to be a more preferable method compared with Online-EMD. When applying Online-VMD in FMCW radar system, minimal monitoring time is 5.5s and reaction time is as low as 0.036s. From the evaluation results, every signal processing method implemented in FMCW has better accuracy than that used in CW radar system, among them, VMD has the highest accuracy of 99.94% when using IAA frequency estimate as the reference method, and it has the lowest variance of 1.37×10^{-3} in FMCW system. The method which has lowest variance in CW system is EEMD of 5.59×10^{-3}, with an accuracy of 99.49%. Online-VMD can enhance the accuracy of Online-EMD by a factor of 4. Therefore, it can be concluded that Online-VMD performed in FMCW radar system with lower central frequency and sampling frequency in slow-time is more suitable for real-time vital signs monitoring.

6.2. RECOMMENDATIONS OF FUTURE WORK

Regarding radar-based non-contact vital sign monitoring system, there are still some challenges that need to be examined in future research, including:

1. In addition to respiration and heartbeat, explore the slight displacement of the human chest caused by other physiological activities such as blood circulation. The

purpose of this research is to establish a model that is closer to the actual physiological activity of the human body, to accurately match the detected information with vital signs.

2. Take the human body movement into account and pose a solution to random body movement elimination. In the thesis, the person being tested is required to remain still in the experiment, however, human posture will change in real application scenarios. In future work, it should be considered to detect human body movements and compensate them using distributed sensors.

3. Investigate the detection of cardiopulmonary abnormalities. This thesis realized the extraction of vital signs of healthy people and the estimation of their instantaneous frequencies and amplitudes. Furthermore, when the tester's respiration or heartbeat signal is abnormal, the cardiopulmonary abnormality should be analyzed from the radar echo signal, and a warning should be issued.

4. Verify the performance of signal decomposition methods in vital signs monitoring by comparing with the ground-truth in various application scenarios, for instance, different human body orientations illuminated by radar.

BIBLIOGRAPHY

[1] Wan-Hua Lin et al. “Comparison of Heart Rate Variability from PPG with That from ECG”. In: *The International Conference on Health Informatics*. Ed. by Yuan-Ting Zhang. Cham: Springer International Publishing, 2014, pp. 213–215. ISBN: 978-3-319-03005-0.

[2] Carlo Massaroni et al. “Contact-Based Methods for Measuring Respiratory Rate”. In: *Sensors* 19 (Feb. 2019), p. 908.

[3] Danilo de rossi et al. “Electroactive fabrics and wearable biomonitoring devices”. In: *Autex Res. J.* 3 (Nov. 2002).

[4] A.S. Fiorillo, Davide C. Critello, and Salvatore Pullano. “Theory, Technology and Applications of Piezoresistive Sensors: a Review”. In: *Sensors and Actuators A: Physical* 281 (July 2018).

[5] A. Nezirovic, A. G. Yarovoy, and L. P. Ligthart. “Signal Processing for Improved Detection of Trapped Victims Using UWB Radar”. In: *IEEE Transactions on Geoscience and Remote Sensing* 48.4 (2010), pp. 2005–2014.

[6] Makie Terazawa et al. “Respiratory Motion Sensor Measuring Capacitance Constructed across Skin in Daily Activities”. In: *Micromachines* 9 (Oct. 2018), p. 543.

[7] Om Prakash Singh, Teo Howe, and Malarvili Balakrishnan. “Real time human respiration carbon dioxide measurement device for cardiorespiratory assessment”. In: *Journal of Breath Research* 12 (Sept. 2017).

[8] Damiano Formenti et al. “Thermal Imaging of Exercise-Associated Skin Temperature Changes in Trained and Untrained Female Subjects”. In: *Annals of biomedical engineering* 41 (Dec. 2012).

[9] W. Wang and A. C. Den Brinker. “Modified RGB Cameras for Infrared Remote-PPG”. In: *IEEE Transactions on Biomedical Engineering* (2020), pp. 1–1.

[10] Kenneth Humphreys, Charles Markham, and Tomas E. Ward. “A CMOS camera-based system for clinical photoplethysmographic applications”. In: *Opto-Ireland 2005: Imaging and Vision*. Ed. by Fionn D. Murtagh. Vol. 5823. International Society for Optics and Photonics. SPIE, 2005, pp. 88 –95.

[11] H. Abuella and S. Ekin. “Non-Contact Vital Signs Monitoring Through Visible Light Sensing”. In: *IEEE Sensors Journal* 20.7 (2020), pp. 3859–3870.

[12] G. Sun. “Non-contact Vital Sign Measurement with Medical Radar and its Clinical Applications”. In: *2019 3rd International Conference on Recent Advances in Signal Processing, Telecommunications Computing (SigTelCom)*. 2019, pp. 90–92.

[13] Eduard Ziganshin, M.A. Numerov, and S.A. Vygolov. “UWB Baby Monitor”. In: Oct. 2010, pp. 159 –161.

[14] Xuyu Wang, Runze Huang, and Shiwen Mao. “Sonarbeat: Sonar Phase for Breathing Beat Monitoring with Smartphones”. In: Sept. 2017, pp. 1–2.

[15] N. Birsan et al. “Time-frequency analysis in Doppler radar for noncontact cardiopulmonary monitoring”. In: *2011 E-Health and Bioengineering Conference (EHB)*. 2011, pp. 1–4.

[16] N. Birsan et al. “Time-frequency analysis in Doppler radar for noncontact cardiopulmonary monitoring”. In: *2011 E-Health and Bioengineering Conference (EHB)*. 2011, pp. 1–4.

[17] A. Tariq and H. G. Shiraz. “Doppler radar vital signs monitoring using wavelet transform”. In: *2010 Loughborough Antennas Propagation Conference*. 2010, pp. 293–296.

[18] W. Hu et al. “Real-time remote vital sign detection using a portable Doppler sensor system”. In: *2014 IEEE Sensors Applications Symposium (SAS)*. 2014, pp. 89–93.

[19] Vinh Phuc Tran and Adel Ali Al-Jumaily. “Non-contact Dual Pulse Doppler System Based Real-time Relative Demodulation and Respiratory Heart Rates Estimations for Chronic Heart Failure Patients”. In: *Procedia Computer Science* 76 (2015). 2015 IEEE International Symposium on Robotics and Intelligent Sensors (IEEE IRIS2015), pp. 47 –52. ISSN: 1877-0509.

[20] Xikun Hu and Tian Jin. “Short-Range Vital Signs Sensing Based on EEMD and CWT Using IR-UWB Radar”. In: *Sciprints* (Aug. 2016).

[21] O. A. Postolache, P. S. Girão, and G. Postolache. “Comparative analysis of two systems for unobtrusive heart signal acquisition and characterization”. In: *2013 35th Annual International Conference of the IEEE Engineering in Medicine and Biology Society (EMBC)*. 2013, pp. 7021–7024.

[22] Zhengwu Xu and Tong Liu. “Vital sign sensing method based on EMD in terahertz band”. In: *Eurasip Journal on Advances in Signal Processing* 2014 (Nov. 2014).

[23] Kun Tian, Jin Li, and Xiaobo Yang. “Separation algorithm of vital sign signal in complex environments based on time-frequency filtering”. In: *EURASIP Journal on Wireless Communications and Networking* 2016 (Dec. 2016).

[24] V. N. Ivanovic, M. Dakovic, and L. Stankovic. “Performance of quadratic time-frequency distributions as instantaneous frequency estimators”. In: *IEEE Transactions on Signal Processing* 51.1 (2003), pp. 77–89.

[25] B. Boashash and T. Ben-Jabeur. “Design of a high-resolution separable-kernel quadratic TFD for improving newborn health outcomes using fetal movement detection”. In: *2012 11th International Conference on Information Science, Signal Processing and their Applications (ISSPA)*. 2012, pp. 354–359.

[26] Jian Li and P. Stoica. “Efficient mixed-spectrum estimation with applications to target feature extraction”. In: *Conference Record of The Twenty-Ninth Asilomar Conference on Signals, Systems and Computers*. Vol. 1. 1995, 428–432 vol.1.

[27] C. Li et al. “Accurate Doppler Radar Noncontact Vital Sign Detection Using the RELAX Algorithm”. In: *IEEE Transactions on Instrumentation and Measurement* 59.3 (2010), pp. 687–695.

[28] Hyunjae Lee et al. “A Novel Vital-Sign Sensing Algorithm for Multiple Subjects Based on 24-GHz FMCW Doppler Radar”. In: *Remote Sensing* 11 (May 2019), p. 1237.

[29] C. A. Dizon, C. F. U. Mendoza, and R. U. Lorenzo. “Direction of arrival (DoA) estimation using root-MUSIC algorithm on the NI PXIe platform”. In: *TENCON 2012 IEEE Region 10 Conference*. 2012, pp. 1–4.

[30] X. Shang, J. Liu, and J. Li. “Multiple Object Localization and Vital Sign Monitoring Using IR-UWB MIMO Radar”. In: *IEEE Transactions on Aerospace and Electronic Systems* (2020), pp. 1–1.

[31] V. Vasu et al. “Using the Lomb periodogram for non-contact estimation of respiration rates”. In: *2010 Annual International Conference of the IEEE Engineering in Medicine and Biology*. 2010, pp. 2407–2410.

[32] H. Noguchi et al. “Signal phase estimation for measurement of respiration waveform using a microwave Doppler sensor”. In: *2013 35th Annual International Conference of the IEEE Engineering in Medicine and Biology Society (EMBC)*. 2013, pp. 6740–6743.

[33] M. S. Rahman, B. Jang, and K. Kim. “A new digital signal processor for Doppler radar cardiopulmonary monitoring system”. In: *2008 International Conference on Electrical and Computer Engineering*. 2008, pp. 76–79.

[34] M. S. Rahman et al. “Extended Kalman Filter for Doppler radar cardiopulmonary monitoring system”. In: *2012 7th International Conference on Electrical and Computer Engineering*. 2012, pp. 264–267.

[35] P. Flandrin, G. Rilling, and P. Goncalves. “Empirical mode decomposition as a filter bank”. In: *IEEE Signal Processing Letters* 11.2 (2004), pp. 112–114.

[36] G. Fang, C. Huang, and C. Yang. “Simultaneous Detection of Multi-Target Vital Signs Using EEMD Algorithm Based on FMCW Radar”. In: *2019 IEEE MTT-S International Microwave Biomedical Conference (IMBioC)*. Vol. 1. 2019, pp. 1–4.

[37] M. E. Torres et al. “A complete ensemble empirical mode decomposition with adaptive noise”. In: *2011 IEEE International Conference on Acoustics, Speech and Signal Processing (ICASSP)*. 2011, pp. 4144–4147.

[38] K. Dragomiretskiy and D. Zosso. “Variational Mode Decomposition”. In: *IEEE Transactions on Signal Processing* 62.3 (2014), pp. 531–544.

[39] Jiaming Yan et al. “Through-Wall Multiple Targets Vital Signs Tracking Based on VMD Algorithm”. In: *Sensors (Basel, Switzerland)* 16 (Aug. 2016).

[40] Y. Xu et al. “Vital Sign Detection Method Based on Multiple Higher Order Cumulant for Ultrawideband Radar”. In: *IEEE Transactions on Geoscience and Remote Sensing* 50.4 (2012), pp. 1254–1265.

[41] Zhibin Yu, Duo Zhao, and Zhiqiang Zhang. “Doppler Radar Vital Signs Detection Method Based on Higher Order Cyclostationary”. In: *Sensors* 18 (Dec. 2017), p. 47.

[42] Nan-Chyuan Tsai and Rong-Mao Lee. “Interaction between cardiovascular system and respiration”. In: *Applied Mathematical Modelling* 35.11 (2011), pp. 5460 –5469. ISSN: 0307-904X.

[43] Amy Droitcour. “Non-contact measurement of heart and respiration rates with single chip microwave Doppler radar”. In: (Jan. 2006).

[44] M. Alizadeh et al. “Remote Monitoring of Human Vital Signs Using mm-Wave FMCW Radar”. In: *IEEE Access* 7 (2019), pp. 54958–54968.

[45] Marco Baldi et al. “Body Movement Compensation in UWB Radars for Respiration Monitoring”. In: Oct. 2012, pp. –.

[46] “Novel signal processing techniques for Doppler radar cardiopulmonary sensing”. In: *Signal Processing* 89.1 (2009), pp. 45 –66. ISSN: 0165-1684.

[47] C. Gu et al. “Instrument-Based Noncontact Doppler Radar Vital Sign Detection System Using Heterodyne Digital Quadrature Demodulation Architecture”. In: *IEEE Transactions on Instrumentation and Measurement* 59.6 (2010), pp. 1580–1588.

[48] Kazuyoshi Itoh. “Analysis of the phase unwrapping algorithm”. In: *Appl. Opt.* 21.14 (ts ,), pp. 2470–2470.

[49] Mamady Kebe et al. “Human Vital Signs Detection Methods and Potential Using Radars: A Review”. In: *Sensors (Basel, Switzerland)* 20 (2020).

[50] Bangkok. *Noise, Vibration, and Harshness (NVH) - APMP*. http://www.apmpweb.org/fms/get_file.php?index=NTU0NA==. 2016.

[51] Jacques Charley, G Bodovillé, and G Degallaix. “Analysis of braking noise and vibration measurements by time—frequency approaches”. In: *Proceedings of the Institution of Mechanical Engineers, Part C: Journal of Mechanical Engineering Science* 215 (Dec. 2001), pp. 1381–1400.

[52] Norden Huang et al. “The empirical mode decomposition and the Hilbert spectrum for nonlinear and non-stationary time series analysis”. In: *Proceedings of the Royal Society of London. Series A: Mathematical, Physical and Engineering Sciences* 454 (Mar. 1998), pp. 903–995.

[53] B. Boashash. “Estimating and interpreting the instantaneous frequency of a signal. I. Fundamentals”. In: *Proceedings of the IEEE* 80.4 (1992), pp. 520–538.

[54] Monson H. Hayes. “Statistical Digital Signal Processing and Modeling”. In: 1996.

[55] Zhengwu Xu and Tong Liu. “Vital sign sensing method based on EMD in terahertz band”. In: *Eurasip Journal on Advances in Signal Processing* 2014 (Nov. 2014).

[56] A. Tariq and H. G. Shiraz. “Doppler radar vital signs monitoring using wavelet transform”. In: *2010 Loughborough Antennas Propagation Conference*. 2010, pp. 293–296.

[57] Kun Tian, Jin Li, and Xiaobo Yang. “Separation algorithm of vital sign signal in complex environments based on time-frequency filtering”. In: *EURASIP Journal on Wireless Communications and Networking* 2016 (Dec. 2016).

[58] Zhaohua Wu and Norden Huang. “Ensemble Empirical Mode Decomposition: a Noise-Assisted Data Analysis Method”. In: *Advances in Adaptive Data Analysis* 1 (Jan. 2009), pp. 1–41.

[59] G. Fang, C. Huang, and C. Yang. “Simultaneous Detection of Multi-Target Vital Signs Using EEMD Algorithm Based on FMCW Radar”. In: *2019 IEEE MTT-S International Microwave Biomedical Conference (IMBioC)*. Vol. 1. 2019, pp. 1–4.

[60] Jiaming Yan et al. “Through-Wall Multiple Targets Vital Signs Tracking Based on VMD Algorithm”. In: *Sensors (Basel, Switzerland)* 16 (Aug. 2016).

[61] Ingrid Daubechies, Jianfeng Lu, and Hau-Tieng Wu. “Synchrosqueezed wavelet transforms: An empirical mode decomposition-like tool”. In: *Applied and Computational Harmonic Analysis* 30 (Mar. 2011), pp. 243–261.

[62] Z. Duan and J. Liang. “Non-Contact Detection of Vital Signs Using a UWB Radar Sensor”. In: *IEEE Access* 7 (2019), pp. 36888–36895.

[63] C. Brüser et al. “Monte-Carlo Simulation and Automated Test Bench for Developing a Multichannel NIR-Based Vital-Signs Monitor”. In: *IEEE Transactions on Biomedical Circuits and Systems* 9.3 (2015), pp. 421–430.

[64] R. Fontugne, P. Borgnat, and P. Flandrin. “Online Empirical Mode Decomposition”. In: *2017 IEEE International Conference on Acoustics, Speech and Signal Processing (ICASSP)*. 2017, pp. 4306–4310.

[65] Xi Ma, Jinqiu Hu, and Laibin Zhang. “EMD-based online Filtering of Process Data”. In: *Control Engineering Practice* 62 (2017), pp. 79 –91. ISSN: 0967-0661.